Super-resolution Imaging, Orientation Analysis, and Image Processing with Machine
Learning in Sum Frequency Generation Spectroscopy

by
Syed Alamdar Hussain Shah

A dissertation submitted to the Department of Chemistry,
College of Natural Sciences and Mathematics
in partial fulfillment of the requirements for the degree of

Doctorate of Philosophy

in Chemistry

Chair of Committee: Steven Baldelli

Committee Member: Shoujun Xu

Committee Member: Ding-Shyue (Jerry) Yang

Committee Member: Arnold M Guloy

Committee Member: Randal Hill

University of Houston
August 2020

DEDICATION/EPIGRAPH

To family.

ACKNOWLEDGMENTS

ABSTRACT

This work encapsulates different aspects of Sum Frequency Generation (SFG) spectroscopy, microscopy, and image processing. It is focused on three areas, namely, super-resolution SFG imaging, molecular orientation analysis for rubrene surface, and improvements in chemical assignment of pixels in SFG imaging. For super-resolution SFG microscopy, a specialized ground state depletion scheme was implemented by modifying the SFG raster scan imaging technique. This strategy deployed a donut shaped depletion beam that suppresses the SFG signal from the peripheral regions of the area illuminated by focused beams used in the raster scan. This improved the spatial resolution by threefold. However, spatial resolution beyond diffraction limit was not attained due to lack of specialized focusing optics. The molecular orientation of the rubrene single-crystal surface was determined using SFG spectroscopy with spectra acquired under different azimuthal orientations and polarization combinations. The SFG analysis indicated a 45° tilt from the surface normal for the phenyl rings of the molecules on the rubrene surface. Finally, a Neural Networks (NNs) based machine learning approach was developed to improve chemical assignment for the pixels in SFG imaging. In this technique, NNs were trained through supervised learning in which they were shown spectra with known chemical labels. Afterwards, they were deployed to predict chemical labels for new pixel spectra. The tests returned above 90 % accuracy under high spectral noise conditions; hence, removing pixel binning requirements traditionally encountered in spectral fitting approach for chemical analysis.

Table of Contents

LIST OF TABLES

LIST OF FIGURES

Chapter 1

Introduction

1.1 Surface Chemistry

The forces exerted by the neighboring molecules affect the physical and chemical properties of a molecule. Inside an isotropic medium, a molecule experiences identical forces from all directions. However, the interface between two isotropic media is by nature anisotropic. This results in application of non-centrosymmetric forces on the surface molecules. Consequently, interfaces frequently show exceptional properties, which are different from those of the bulk media. Furthermore, in many chemical systems, the chemical activity is dominated by the chemistry at the interface [1]. Therefore, surfaces and interfaces have been a topic of extensive scientific research, leading to the development of specialized field of surface chemistry [2, 3].

A thorough understating of surface chemistry is becoming increasingly important as modern scientific and engineering advances have necessitated increased chemical control of the systems used in these applications, especially in areas such as nano-particles [4, 5], corrosion [6], wetting [7, 8], and catalysis [3]. In biology, surfaces such as cell membranes play a vital role in not only separating the inter- and intra-cellular environments but also mediating the sophisticated exchange between them [9]. In nano-technology, a reduction in particle size leads to an increase in the ratio of surface area to volume, which increases the overall contribution of the surfaces, especially impacting the particle-particle and particle-media interactions [10]. A simple modification of the nano-particle surface can result in pronounced changes in their colloidal behaviors such as

suspension and aggregation dynamics. In corrosion and catalysis, surfaces play a key role in initiating or inhibiting the underlying chemical reactions [11]. In some of these systems, the presence of even a single-molecule-thick layer on the metal surface, may lead to enhanced resistance to corrosion or poisoning of a catalyst [12, 13], thus, rendering the system chemically effective or completely ineffective. Surface modifications can also improve or reduce water repellency, giving control over hydrophobicity and hydrophilicity with far-reaching technical and engineering applications [14].

A proper understanding of chemical and physical properties of a surface requires investigation of their molecular origins. However, these studies can often be challenging since the interface contains only a fraction of molecules compared to the bulk. The bulk contribution can easily overwhelm the chemical signatures of the surface species. This requires techniques, which are both surface specific and chemically sensitive.

In addition to unique chemistry, surfaces also display 2D-spatial heterogeneity in the surface plane. Surface heterogeneity plays a crucial role in both chemical and physical functionality of surfaces. For example, various grains in polycrystalline electrodes may show different chemistry [15-17]; wetting of a surface may change by micro texturing [18]; and specific sites on a cell membrane mediate material exchange [19]. Ensemble-probing technique that collects an average response from a surface would not be able to resolve its chemical heterogeneity. This is illustrated in Figure 1, where the two sample surfaces have the same average chemical composition but different spatial distribution. If the whole regions are probed, both may give resembling response to any technique that is insensitive to 2D-spatial heterogeneity over the surface.
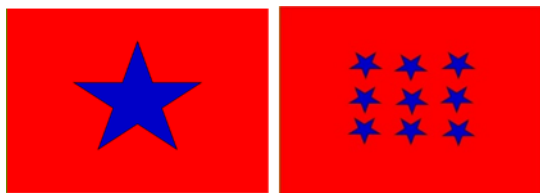
Figure 1: Two sample surfaces where red and blue regions indicate different chemical natures. The two surfaces have same total red and blue areas but different spatial distributions. For a surface chemistry technique without spatial specificity, both samples will appear identical.

Multiple techniques have been developed to study interfacial chemistry. A whole range of scanning probe techniques utilizes different physical and chemical interactions between the sample and a fine tip in close proximity, e.g., Scanning Tunneling Microscope (STM) [20, 21], Atomic Force Microscope (AFM) [22], and Functionalized-AFM [23, 24]. These methods yield superb spatial resolution but may pose challenges in chemical identification or cause modification of surface species. Furthermore, the dependence on a tip creates its own challenges in probing buried interfaces such as a solid-solid interface. On the other hand, far-field spectroscopic techniques such as IR and Raman have been adapted to limit the thickness of material probed by the incident light, hence making them pseudo-specific to the interface [25, 26]. Particularly, Raman spectroscopy has been modified using the electric field enhancement on rough surfaces to generate surface enhanced Raman Spectroscopy (SERS). In addition to rough surfaces, SERS is also applicable to nano-structures, which are specially fabricated to gain an electric-field enhancement. As a result, SERS has acquired reasonable spatial specificity and excellent spatial resolution [27-29]. However, the dependence on an enhancement of the electric field from substrates limits the versatility of this technique. Another significant class of surface techniques utilizes ions, electrons or neutrons [30-33], as these high energy particles have short interaction lengths compared to photons. However, these techniques often require vacuum conditions and are limited to solid-

vacuum or liquid-vacuum interfaces. Recent developments are pushing these methods towards ambient conditions [34-38].

Sum frequency generation (SFG) spectroscopic methods are particularly useful probes for surface chemistry. They are both surface-specific and chemically sensitive, and they can be used in-situ under ambient conditions [39]. Unlike scanning-probe methods (e.g., AFM and STM), SFG does not require any tip to be close to the surface under study. Therefore, the probing and detection may be conducted from a distance (or in a far field). In contrast to electron diffractions and ion emissions, it does not require vacuum. In comparison with other spectroscopic techniques such as Attenuated Total Reflectance Fourier Transform Infrared (ATR FTIR) and Total Internal Reflectance Raman (TIR Raman), SFG signals are only produced from the few-atom-thick interface where the chemical or physical properties change [39-41]. However, SFG signals are typically quite weak. This inherent weakness creates unique challenge, including the dependence on an intense pulsed-laser as the optical source and a sensitive detector for detection. Despite these challenges, the spectroscopic chemical specificity and surface sensitivity, typically without the need of background subtraction, make SFG an indispensable tool for a wide variety of systems. Its abilities for the surface chemistry have been summarized in several publications [39-43]. SFG has been particularly useful for characterizing self-assembled monolayer systems, surfactants, ionic liquid interfaces, solid-air interfaces, and many other systems.

In self assembled monolayers (SAMs), SFG spectroscopic imaging has been instrumental in characterizing the orientations, packing, conformational orders, chemical identification, surface heterogeneity, and multiple other properties on different metallic and non-metallic substrates [44-46]. Furthermore, SFG spectroscopy has enabled the study of interfacial ordering for ionic liquids

at air-liquid, dielectric-liquid, metal-liquid, and multiple other interfaces [47-58]. In these systems, the electrical, chemical, thermodynamic, and steric effects introduce ordering in the ionic liquid interfaces. In these SFG active ordered layers, the orientation, packing, and location of ions convey vital information about the complex forces at the interface.

1.2 Theory

SFG is a second-order nonlinear process in which two laser beams interact with the material to produce a third one with an energy that is sum of the original two. Typically, the two input beams consist of a mid-IR and a visible beam. The conservation of energy leads to the following relation

$$\omega_{SF} = \omega_{Vis} + \omega_{IR} \qquad\qquad Eq.\,(1)$$

where ω_{Vis} and ω_{IR} are the frequencies of the input beams, and ω_{SF} is the frequency of the output beam. Furthermore, the component of momentum parallel to the surface is also conserved; consequently,

$$\vec{k}_{||,SF} = \vec{k}_{||,Vis} + \vec{k}_{||,IR}$$

$$n_{SF}\omega_{SF}sin(\theta_{SFG}) = n_1\omega_1 sin(\theta_1) + n_2\omega_2\,sin(\theta_2) \qquad\qquad Eq.\,(2)$$

where $\vec{k}_{||}$,s are the parallel components of the wave vectors, n's represent refractive indices and θ's represent the angle of incidence or emission for the three beams involved in the SFG process [41-43, 59]. The mathematical relations of Eq. 1 and Eq. 2 are pictorially represented in Figure 2.

From a macroscopic point of view, the two incident beams initiate the SFG process on the surface. The oscillating electric fields of these lasers induce an oscillating polarization in the sample material.
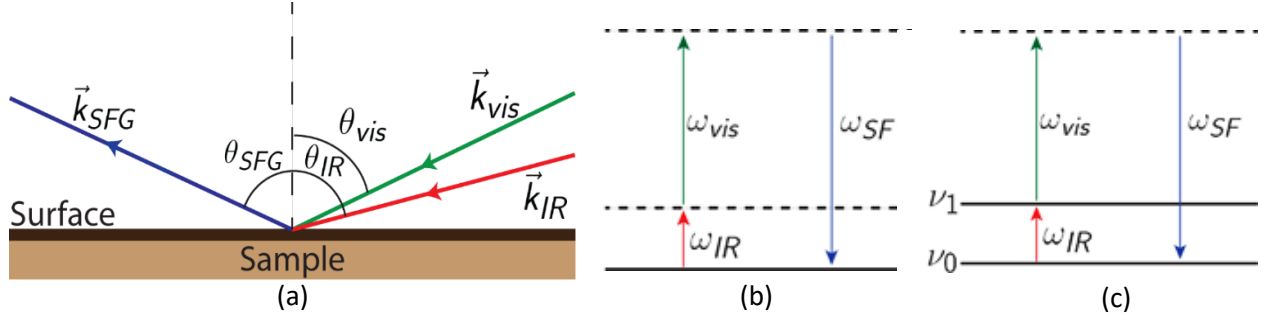
Figure 2: Pictorial description of the SFG process. (a) Momentum conservation in a typical experimental geometry for surface SFG, (b) Nonresonant SFG process, and (c) Resonant SFG process in terms of energy level diagrams. In (b) and (c) the dashed lines represent non-stationary energy levels, and solid lines represent stationary energy levels. v_1 is the excited and v_0 is the vibrational ground state.

This polarization can be resolved into different response components [41, 59-61].

$$P = P^{(1)} + P^{(2)} + P^{(3)} + \cdots$$

In this expansion the second order component can be expressed as

$$P^{(2)} = \chi^{(2)} : E_1 E_2 \qquad\qquad Eq.\,(3)$$

where $\chi^{(2)}$ is a nonlinear susceptibility tensor and $E_{1,2}$ indicate the electric field vectors of the two input lasers. In centrosymmetric media, an inversion operation leads to

$$-P^{(2)} = \chi^{(2)} : (-E_1)(-E_2)$$

$$-P^{(2)} = \chi^{(2)} : E_1 E_2 = P^{(2)}$$

which is only possible if $\chi^{(2)} = 0$; therefore, the SFG process becomes surface specific in centrosymmetric media.

The oscillating polarization acts as a source for generating the sum frequency (SF) electromagnetic wave with the following intensity

$$I_{SF} \propto |P^{(2)}|^2 = \left| \chi^{(2)} : E_1 E_2 \right|^2 \qquad Eq.\,(4)$$

In an energy level description, the two input lasers take the material from the ground state to some non-stationary states. The material then goes back to the ground state by emitting a SF photon as shown in Figure 2(b). If one of the intermediate states is a stationary state, such as a vibrational excited state, the process becomes resonance-enhanced (Figure 2 (c)).

$$\chi^{(2)} = \chi^{(2)}_{NR} + \chi^{(2)}_{res} \qquad Eq.\,(5)$$

Therefore, the SF intensity becomes resonance-enhanced when one of the input lasers is frequency-matched with the vibrational transition. The frequency-matched beam creates a coherence from the vibrational ground state to the excited state. The visible beam then takes it to the virtual/non-stationary state. From non-stationary state, the molecule quickly falls back to vibrational ground state by emitting the SF photon.

1.2.1 SFG Spectroscopy

In vibrational spectroscopy applications, one of the two input beams is scanned through the mid-infrared (mid-IR) frequencies where vibrational transitions of the molecules reside. The other beam is traditionally kept in the visible frequencies so that the sum frequency beam is generated in the visible frequency range where multiple sensitive detectors are available. The molecular information for the surface is contained in the resonant component of the SFG process. Therefore, the problem boils down to measuring $\chi^{(2)}$ for the surface. Different components of $\chi^{(2)}$ can be accessed by selecting different polarizations of the input laser beams and output SF signal [42, 43].

7

The macroscopic nonlinear susceptibility $\chi_{ijk}^{(2)}$ is related to microscopic hyperpolarizability of the surface molecules by [43, 62]:

$$\chi_{ijk}^{(2)} = N_s \sum_{i'j'k'} \langle R_{ii'} R_{jj'} R_{kk'} \rangle \beta_{i'j'k'} . \qquad Eq.\,(6)$$

where N_s is the number density of molecules on the interface; $R's$ are the rotational transformation matrices between the lab coordinates and the molecular coordinates; $\langle \rangle$ indicates orientational average over all surface molecules; and β is the molecular hyperpolarizability. β can be further decomposed into a nonresonant and a resonant part [43]:

$$\beta = \beta_{NR} + \sum_q \frac{n_q \beta_q}{\omega_{IR} - \omega_q + i\,\Gamma_q} . \qquad Eq.\,(7)$$

In the resonant part, β_q, ω_q, and Γ_q are the SFG amplitude, frequency, and damping rate of the qth vibrational mode, respectively. n_q is the fraction of molecules in vibrational ground state. The matrix elements of β_q can be expressed in terms of the Raman polarizability (α) and IR transition dipole moment (μ) as follows:

$$\beta_{i'j'k',q} = -\frac{1}{2\,\epsilon_0 \omega_q} \frac{\partial \alpha_{i'j'}}{\partial Q_q} \frac{\partial \mu_{k'}}{\partial Q_q} \qquad Eq.\,(8)$$

Here Q_q is the normal coordinate of the qth vibration mode.

1.2.2 Ground State Dependence of SFG

When the IR beam is resonant with the vibrational modes of the molecules, the time-dependent induced polarization can be expressed as [63-66]

$$P(t) = \left(\alpha_{vis}^{(1)} + \frac{\partial \alpha_{vis}^{(1)}}{\partial q} q(t) + \cdots \right) E_{vis}(t) \qquad Eq.\,(9)$$

where $q(t)$ is the normal mode driven by the $E_{IR}(t)$ such that

$$q(t) = \Delta\rho \, \frac{e^*}{m^*} \frac{E_{IR}(t)}{\omega_0^2 - \omega_{IR}^2 - i\,\omega_{IR}T_2^{-1}} \qquad Eq.\,(10)$$

In this expression for the normal mode, $\Delta\rho$ is the difference between fractional populations of the ground state and the excited state, m^* is the reduced mass, e^* is the reduced charge, ω_0 is the resonance frequency, ω_{IR} is the laser frequency, and T_2^{-1} is the damping rate [65-67].

In these equations, the damping rate T_2^{-1} defines the spectroscopic lineshape associated with the molecular vibration. This damping or dephasing results from the loss of coherent oscillation of the induced polarization in the molecular ensemble. Furthermore, the vibrational excited states have a finite lifetime after which the molecule decays back to ground state by spontaneous emission. This provides an additional contribution to the dephasing and damping. Consequently, the dephasing time is typically given by [67]

$$\frac{1}{T_2} = \frac{1}{T_2^*} + \frac{1}{2T_1} \qquad Eq.\,(11)$$

where T_2^* is the pure dephasing time and T_1 is the excited state lifetime.

By combining Eq. 9 and Eq.10, the second order component of the induced polarization becomes:

$$\alpha^{(2)}(\omega_{SF} = \omega_{vis} + \omega_{IR}) = \Delta\rho \, \frac{\partial \alpha_{vis}^{(1)}}{\partial q} \frac{e^*}{m^*} \frac{E_{IR}(t)}{\omega_0^2 - \omega_{IR}^2 - i\,\omega_{IR}T_2^{-1}} \qquad Eq.\,(12)$$

This can be related to the macroscopic susceptibility as follows:

$$\chi_{res}^{(2)} = N < \alpha^{(2)} >$$

where brackets indicate molecular average and N is the number density of molecules on the surface. This leads to following relation between the SF intensity and the ground state population.

$$I_{SF} \propto \left| \chi_{NR}^{(2)} + \chi_{res}^{(2)} \right|^2 I_{vis} I_{IR}$$

$$I_{SF} \propto \left| \chi_{NR}^{(2)} + N\Delta\rho < \frac{\partial \alpha_{vis}^{(1)}}{\partial q} \frac{e^*}{m^*} \frac{E_{IR}(t)}{\omega_0^2 - \omega_{IR}^2 - i\,\omega_{IR} T_2^{-1}} > \right|^2 I_{vis} I_{IR} \qquad Eq.\,(13)$$

This expression implies that the resonance component of the I_{SF} is proportional to

$$\Delta\rho^2 \left| N < \frac{\partial \alpha_{vis}^{(1)}}{\partial q} \frac{e^*}{m^*} \frac{E_{IR}(t)}{\omega_0^2 - \omega_{IR}^2 - i\,\omega_{IR} T_2^{-1}} > \right|^2 I_{vis} I_{IR}$$

which can be simplified to

$$(2n_0 - 1)^2 C(\omega_{IR}) I_{vis} I_{IR} \qquad Eq.\,(14)$$

where n_0 is the fractional ground state population. I_{vis} and I_{IR} are the visible and IR intensities, respectively. The rest of the terms from the previous expression are incorporated by an IR frequency-dependent proportionality constant $C(\omega_{IR})$.

Following the relation in Eq. 14, if the vibrational ground state population can be pumped to the excited state with the help of another resonant mid-IR beam, the resonant SF signal can be depleted. This enables SFG signal depletion in which a mid-IR beam pumping the population out of ground state is followed by a pair of visible and mid-IR beams for generating the SF signal from the remaining population. The mid-IR pumping the population out of the ground state is called pump IR and the one producing the SF signal with the visible is called probe IR. Changing the

delay between pump IR and probe IR-visible pair can track the recovery of ground state population through SF signal. This effect is displayed in Figure 3, where the SF signal is displayed side-by-side with the fractional population of the ground state for a two level system. The pump IR acts on the system for a duration marked by the dashed line. During this time, the ground state population decays. Afterwards, the population is recovered through spontaneous emission. The temporal behavior of the probe SF signal is traced by tuning the delay between pump IR and probe IR-visible pair. In a two level system used for this simulation, the minimum fractional population of the ground state cannot be less than 50 % (due to spontaneous emission); however, the corresponding SF signal drops to 0 at 50 %.
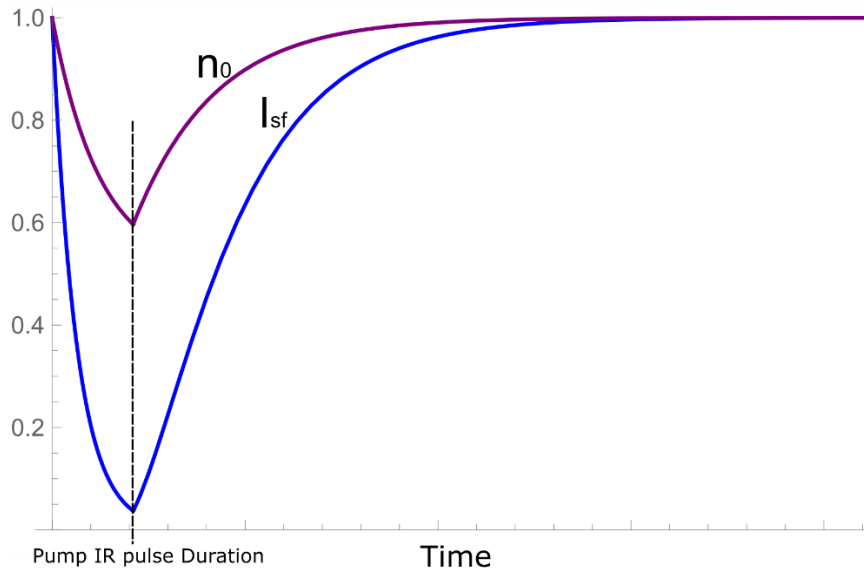
Figure 3: Fractional population along with the SF signal in an SFG signal depletion simulation for a 2-level system.

1.3 SFG Imaging

Multiple SFG microscopy methods have been developed for analyzing the 2D surface heterogeneities. In these methods, the image contrast is generated from multiple mechanisms of

11

chemical importance such as, chemical functional groups, molecular orientation, surface concentration, molecular conformation, and local electric fields. The first attempts at creating SFG microscope by Florsheimer et. al., [68] involved total internal reflection geometry in which the sample was placed/coated on one side of the prism and the input laser beams were incident through the other two sides, generating an outgoing SF light that was collected and recorded by an optical objective and a CCD camera, respectively. Due to the directional nature of SF beam, the traditional SFG microscopy designed for oblique incidence suffered objective defocusing. Afterwards Kuhnke et. al., [69] introduced modified design with improved focus and field of view by following Chastang's scheme in which the surface is first optically relayed onto a diffraction grating and then the diffraction grating is imaged with a microscope objective [70]. These designs inspired the first SFG microscope at University of Houston, that led to the study of self-assembled monolayer systems prepared using micro-contact printing [44].

Since then SFG microscopy has been using in chemical, biological, and physical research [71-73]. Multiple versions have been developed with modifications ranging from inclusion of intensified CCDs [74] to compressive sensing single-pixel imaging [75]. SFG microscopy as also been combined with other spectroscopic microscopies such as second harmonic generation (SHG), coherent anti-stokes Raman scattering (CARS), Raman scattering [73]. In addition to surface specific studies, SFG spectroscopy and microscopy have also been used for investigating bulk systems with multi-layered or non-centrosymmetric media [76-78].

The SFG microscopy, long collection times and comparatively limited spatial resolution are two main challenges. To overcome long collection time, SFG microscopy is combined with Compressive Sensing (CS) technique [75, 79-81]. The CS-SFG microscope utilizes digital mirror

device (DMD) to pattern the visible beam that is then combined with the femtosecond IR beam spatially and temporally on the sample surface. This generates a SF beam. The SF beam is then sent to a detector. Each pattern acts as an imaging basis and only a few percent of total number of patterns are required to capture an accurate representation of the surface morphology; thus, boosting the imaging speed. Furthermore, since each measurement collects signal from entire sample, the sensitivity increases due to improved S/N ratio [79, 80].

1.4 Conclusion

SFG provides a powerful and versatile tool for probing chemical properties of interfacial species through surface specific spectroscopy. It has also been developed into a set of advanced imaging techniques for understanding the spatial heterogeneity of chemical behavior on surfaces. However, unlike some fluorescence microscopies, the resolution for SFG microscopy is still limited to more than a few microns. This hinders the applicability of SFG microscopy to sub-micron length scales that contain multiple systems of scientific and technological interest. Therefore, a major portion of this work is dedicated to the development of a viable path towards super-resolution SFG microscopy. Additionally, the surface specificity and chemical sensitive of SFG have also been utilized in the analysis of rubrene single-crystals. Finally, machine-learning algorithms such as Neural Networks have been developed to aid SFG image analysis.

The following few chapters are devoted to the development of a path towards super-resolution SFG microscopy. Chapter 2 outlines the general laser and optical setups utilized in this work. Chapter 3 and 4 focus on technique, simulation, and development of the super-resolution SFG microscope. Chapter 5 introduces spectroscopic application of SFG technique for analyzing the orientation of surface molecules on a rubrene single-crystal. Finally, chapter 6 explores Neural

Network based machine-learning approach for enhanced-chemical identification of pixels in those SFG images where poor signal-to-noise ratio makes identification through spectral curve fitting impossible.

Chapter 2

Experimental Setup

2.1 Introduction

The SFG process is typically quite weak; therefore, intense input lasers are required to generate a detectable signal. To achieve high optical flux without damaging the sample or the optics, pulsed-laser beams are utilized. In contrast to a continuous wave laser, a pulsed-laser provides short pulses of light. These pulses are typically a few pico-seconds or femto-seconds long. Therefore, the peak intensities in such pulses are astronomically high compare to a continuous wave laser at similar average power. These pulsed-laser beams also require a controllable and diverse set of wavelengths for performing SFG spectroscopy or microscopy. Both these qualities are achieved with the help of a pico-second 1064 nm laser and an optical parametric generator/amplifier (OPG/OPA). These two instruments are the main components for the experimental setups utilized in this work. Therefore, this chapter gives a brief description on the internal workings of these systems. The detailed description for different processes in each system can be found in previous works [82-85]. Furthermore, a brief outline of common detection scheme in these experiments is also provided. The specific details of each detection technique are contained in the relevant chapters for every experiment.

2.2 Main Laser

A 1064 nm EKSPLA PL2251 series laser produces 21 ps pulses at 20 Hz with 28 mJ energy per pulse which act as the main light source in this experiment. The outline of the laser is shown in

Figure 4. The laser consists of three main components; master oscillator, regenerative amplifier, and power amplifier [82]. The fundamental 1064 nm pulsed beam is produced by the master oscillator using a 808 nm diode pumped Nd:YVO$_4$ laser material. This beam then seeds the regenerative amplifier stage where a diode pumped Nd:YAG rod (R2) amplifies the pulse power for a few cycles. After regenerative amplifier the pulse enters the final amplification stage where a flash-lamp pumped Nd:YAG rod (R3) completes the final amplification step [86]. The output of the laser is then used to pump an OPG/OPA.
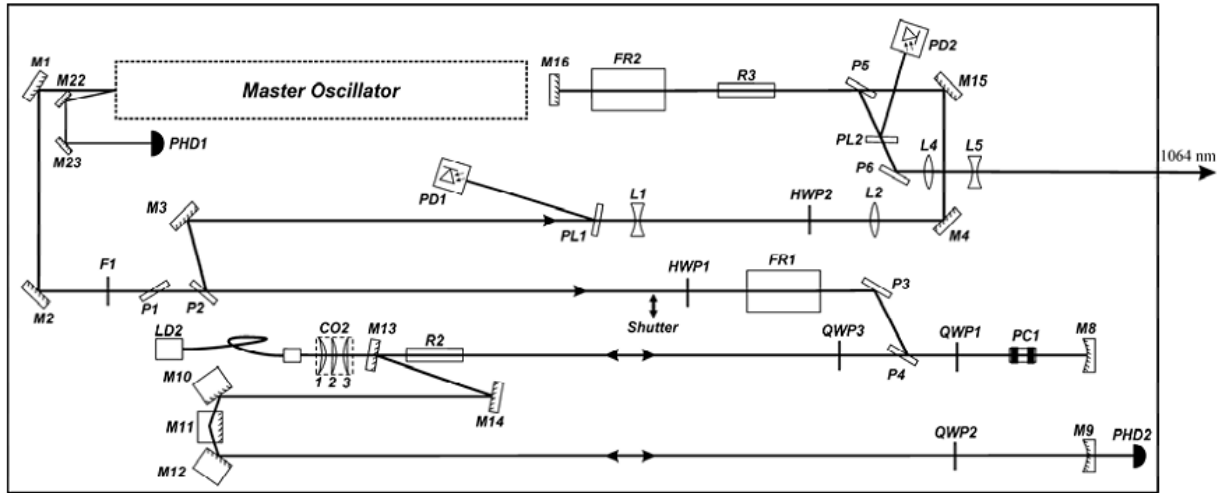
Figure 4: Schematic for ESKPLA laser. Image adapted from user manual for the laser [82].

2.3 OPG/OPA

A Laser-Vision OPG/OPA produces the visible and mid-IR wavelengths required for SFG from the 1064 nm laser. The schematic of OPG/OPA is shown in Figure 5.
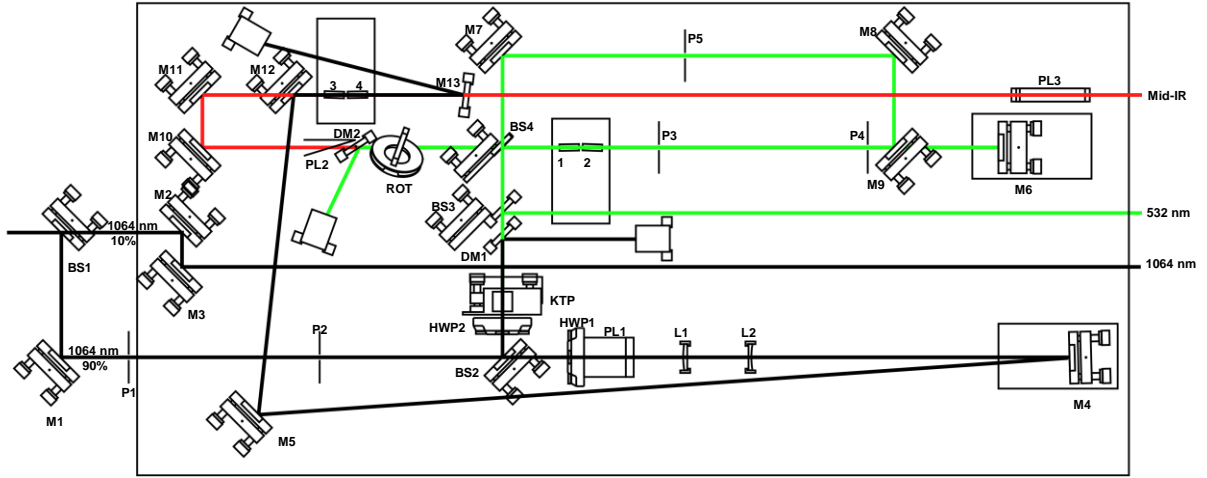
Figure 5: Optical diagram for OPG/OPA system [87].

The 1064 nm output from the ESKPLA laser is split into a 90 : 10 ratio at beam-splitter BS1. The 90 % split is sent to the OPG/OPA. Inside the OPG/OPA the beam is further split at beam-splitter BS2; one portion is sent to the OPA stage and the other portion is frequency-doubled to generate a 532 nm beam. The 532 nm beam is split at beam-splitter BS3 where 50 % is set to the SFG setup and the rest is utilized to pump the KTP crystals 1 and 2 in the first OPG stage. The output of the OPG stage (shown in red) is combined with the remaining portion of the 1064 nm to generate the desired mid-IR wavelength in OPA stage using KTA crystals 3 and 4. By turning the mutual angles of crystal 1 through 4, the OPG/OPA is able to generate mid-IR from 2000 cm^{-1} to 4000 cm^{-1} [83-85].

2.4 SF Detection

The SF signal generated in various experiments is detected by a combination of a monochromator and a photo-multiplier tube (PMT). The monochromator helps separate unwanted light from the SF wavelength. The PMT serves as a sensitive instrument for detecting extremely small SF signals.

Since pulsed-laser beams are utilized for producing SF light, the SF signal is also pulsed. Therefore, the output of PMT consists of current pulses, which are sent to a boxcar averager for gated-integration. In gated-integration, the recording device registers the input signal for only a brief amount of time that is dictated by a controllable time-gate. Consequently, if the gate is timed with the SF signal, the unwanted electronic noise coming from the PMT can be filtered out. Furthermore, the boxcar implements a moving-average that smooths out the PMT signal from multiple laser shots. Finally, the boxcar outputs a voltage proportional to the averaged PMT signal. A data acquisition device (DAQ) reads boxcar's voltage output and sends it to computer where a set of homebuilt LabView programs record it. The details of these programs are described later. This workflow is shown in Figure 6. The details of each individual optical-setup depend on the goal of the experiment. Therefore, for the studies described in subsequent chapters, the optical setups are presents in the chapters.
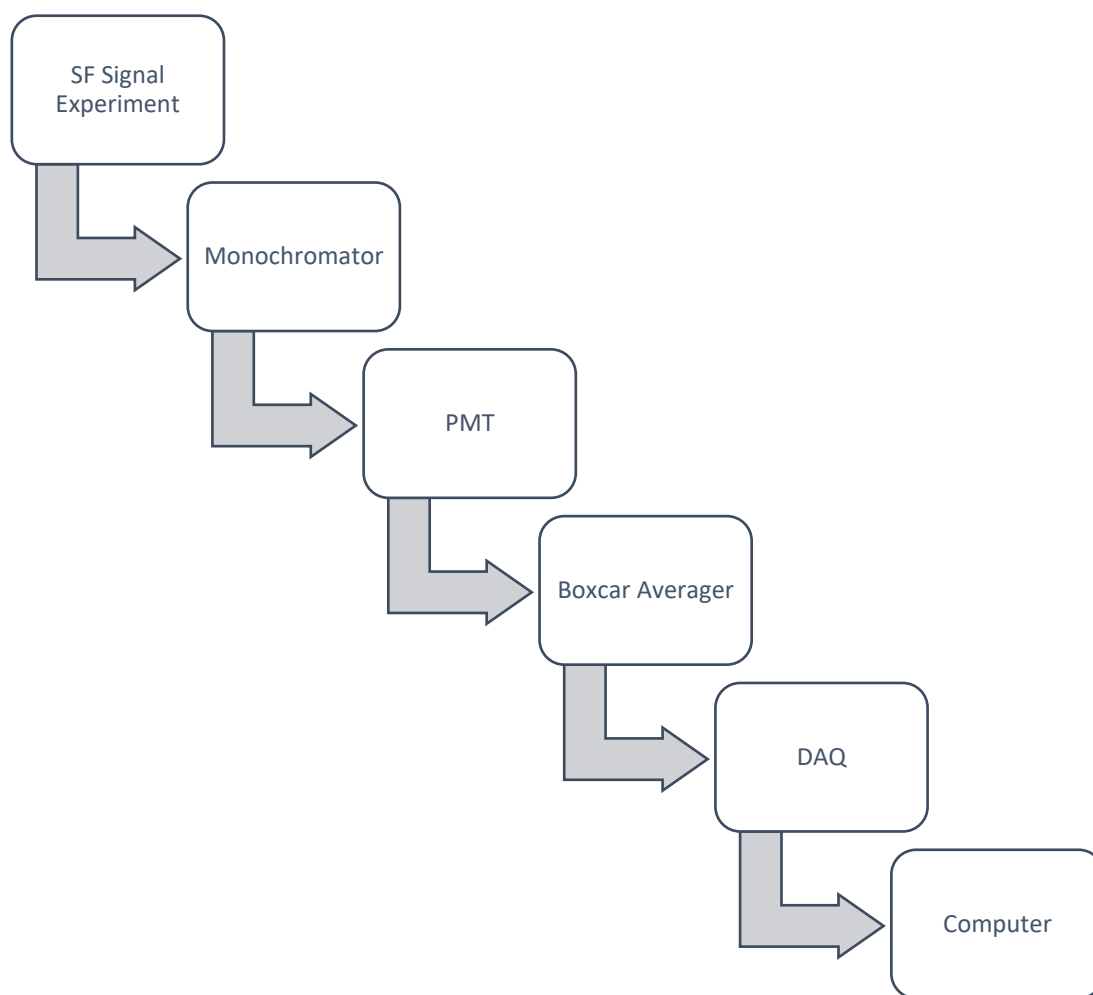
Figure 6: Workflow for SF signal detection from typical optical setup.

Chapter 3

Super-Resolution in SFG Microscopy

3.1 Introduction

To resolve the heterogeneity in the physical and chemical properties of surface, SFG spectroscopic-microscopy provides a powerful tool. However, due to naturally weak signals in the nonlinear second-order SFG process, the microscopy becomes difficult. In the direct chemical imaging using SFG, extremely low signal levels increase the time required to generate a chemically reliable image even with sensitive detection instruments (e.g., intensified CCD, PMT). This resulted in the development of CS-SFG microscopy, which provides faster SFG imaging [75, 79, 80].

 The resolution in the direct-imaging is dictated by the combination of microscope-objective's magnification and the pixel size in the camera [83, 88]. On the other hand, in CS imaging, the resolution is dependent on the objective and DMD mirror size. Both these techniques are diffraction limited with practical resolution far above the diffraction limit. The combination of microscope objective's magnification and pixel size gives a resolution of 2 μm for direct imaging. On the other hand, CS imaging can produce spatial resolution of 2 μm to 8 μm [79, 80]. However, for a complete study of 2D-spatial variation in surface chemistry, the scales above a few microns are mesoscopic for many systems. A better microscopic description of spatial variation in many chemical systems often requires imaging with sub-micron resolution. This necessitates the development of a super-resolution imaging technique for SFG microscopy.

In its simplest form, far-field optical microscopy can be performed by raster scanning tightly focused laser beams on the sample and collecting the signal point-by-point. This approach is limited by the diffraction limit as the size of the focal spot that determines the resolution, cannot be arbitrarily small. Super-resolution in Fluorescence and stimulated Raman microscopies has been achieved by modified versions of the raster-scanning microscopy [89-93]. The basic principle is the use of an additional, donut-shaped laser beam that can suppress the sample's ability to produce signal-of-interest from the peripheries of the original focal spot. This creates a signal-emitting-spot that is sharper than the original focal spot [90, 92].

The original work by Hell et. al., introduced the framework for achieving super-resolution in the spectroscopic-microscopy through the concept of ground state depletion (GSD) [90]. The basic principle consisted of reducing the spot size that could produce the relevant fluorescence signal, below the excitation laser's focal spot-size. To achieve this, the use of an additional beam structure into donut-shape, was proposed. This structured beam modified the populations of the molecular states to achieve the required effect.

Similar approach for modifying SFG production using ground state population manipulation can be utilized to create super-resolution SFG microscopy. In SFG spectroscopy, pump-probe and time resolved experiments have already demonstrated the possibility of SFG manipulation through ground state modification [63, 65-67, 94]. Taking inspiration from the Pump-Probe SFG and GSD microscopy, I have developed and implemented a super-resolution SFG microscopy technique.

3.2 Super-Resolution Technique

In a traditional raster-scanning SFG microscope the mid-IR beam is focused to a tight spot and the image is generated by collecting SF signal point-by-point from the sample surface. The size of the focal spot that determines the resolution is limited by the Abbe diffraction limit given by [95]

$$d = \frac{\lambda}{2NA} \qquad\qquad Eq.\,(15)$$

where d is the spot diameter, λ is the wavelength of light, and NA is the numeric aperture for the imaging system . As a result, for a 3 μm to 5 μm wavelength, the resolution is theoretically limited to 1.5 μm to 2.5 μm. However, practically it is difficult to achieve these resolutions due to limited NA available in typical imaging systems.

Although the diffraction-limited spot size for visible beam is smaller than that of the mid-IR, it is the mid-IR, which is usually focused on the sample surface. The reason behind this choice is lower damage threshold for visible than mid-IR because the visible beam has higher energy per photon and higher absorption cross-section in most samples [66]. This lower damage threshold limits the useable intensity of the visible light; thus, the amount of SF signal drops and one runs into the detection limit well before the diffraction limit is reached.

For a pulsed mid-IR beam spatially and temporally overlapped with the visible beam, the SF signal will be generated from the entire focal spot. The ground state population will be depleted from the peripheral regions of the focal spot if a pump IR is shaped in the form of a donut and focused on the sample surface. However, the central region will still have most molecules in the ground state because here the donut shaped pump beam is dark. If such a spot is then probed by a pair of visible and probe IR beams, before the ground state population recovers, the SF signal will be produced

by effectively a smaller spot. This modification results from the ground state depletion in the peripheral regions. Only the central region with un-depleted ground state population will produce the SF signal. Therefore, the SFG takes place on an effectively sharper spot than the probe IR focal spot; thus, increasing the resolution. This scheme is diagrammatically shown in Figure 7, which represents an oblique incidence geometry for pump IR, probe IR, visible, and SF beams.
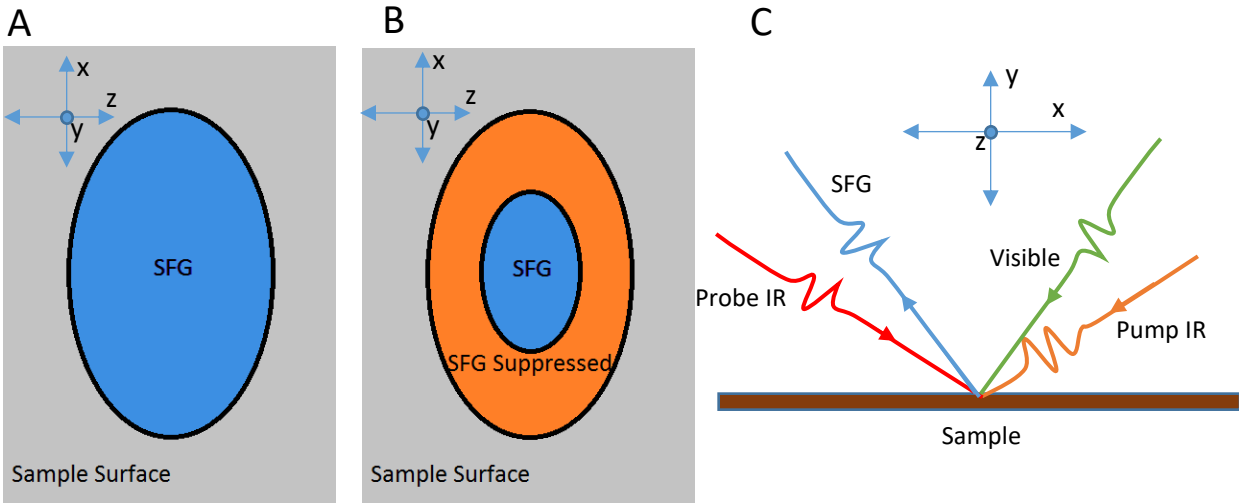
Figure 7: Pictorial representation of super-resolution SFG microscopy scheme. (A) and (B) show the effective increase in resolution by the application of a donut shaped pump IR. (C) displays the experimental geometry. Since it is an oblique incidence geometry, the shape of beams in the surface plane (xz-plane) are elongated along the directions of incidence (x-axis). (A) normally the SFG process takes place on the entire area of probe IR focal Spot. (B) with the help of pump IR the SFG process is suppressed in the peripheral regions of the probe IR focal spot, effectively giving an enhanced resolution.

In Figure 7 C, the beams are shown in the plane of incidence i.e., xy-plane. The figure also illustrates that the pump IR pulse reaches surface before the counter propagating probe IR and copropagating visible pulses. The surface is positioned in the xz-plane. Panel A illustrates that the SFG is produced by the entire focal spot when pump IR is not used. Panel B displays the change

in SFG area when a donut shaped pump IR modifies the ground state population before the probe IR-visible beam pair reaches the sample surface.

The size of the dark region in the donut shaped pump IR is not limited by the Abbe diffraction limit and can be made arbitrarily small. However, the final resolution for this scheme will be limited by the detection limit because decreasing the effective SF producing surface area will result in decreased SF signal. Furthermore, the effective resolution enhancement in this GSD based super-resolution technique depends heavily on the dynamics of the depletion and the repopulation of the vibrational ground state. Therefore, the next sections show different simulation results on the population dynamics, pump-probe SFG, and resolution enhancement. The parameters utilized in these simulations are matched with our experimental capabilities.

3.3 Simulation

3.3.1 SFG with Ground State Depletion

To simulate the GSD based super-resolution scheme introduced in the previous section, the test system needs to have a vibrational state with excited state lifetime greater than the pulse duration of lasers utilized in this work. Furthermore, the system has to be surface specific. Considering these requirements, surface hydrogen on silicon(111) is selected as the test system for these simulations. This same system will also be utilized for experimental demonstration of spatial resolution enhancement in the next chapters. Surface hydrogen exhibits a single Si-H stretch with an excited state lifetime of $1\,\text{ns}$ and frequency of $2073\,\text{cm}^{-1}$ at room temperature [65, 66]. Therefore, for an optical setup with $21\,\text{ps}$ long laser pulses, this system serves as an ideal testing ground for GSD.

From the time-dependent description of the SFG process presented in chapter 1, the SF signal intensity is given by

$$I_{SF} = (2n_0 - 1)^2 C(\omega_{IR}) I_{vis} I_{IR} \qquad\qquad Eq.(16)$$

in this relation, n_0 represents the fractional population of the vibrational ground state. At room temperature, most of the molecules are in the ground state. However, a molecule in vibrational ground state can be promoted to a vibrational excited state by the absorption of a photon from an IR laser resonant with the vibrational mode. The now excited molecule can either spontaneously emit a photon and go back to the ground state or can be stimulated to return to ground state with the help of an other photon from the same resonant IR laser. These two processes form the basis of spontaneous and stimulated emissions. The interplay between the absorption, the stimulated emission, and the spontaneous emission can be captured by Einstein's A and B coefficients [96]. Using this approach, the rate of change of ground state population under the action of a resonant IR laser is given by

$$\frac{\delta n_0}{\delta t} = W^*_{1\to 0} + W_{1\to 0} - W_{0\to 1}$$

In this equation $W^*_{1\to 0}$ is the rate of increase in the ground state population through spontaneous emission, $W_{1\to 0}$ is the rate of increase by stimulated emission, and $W_{0\to 1}$ is the rate of decrease through absorption. In terms of the A and B coefficients these rates can be described as

$$\frac{\delta n_0}{\delta t} = A\, n_1 + I_{IR} n_1 B_{1\to 0} - I_{IR} n_0 B_{0\to 1} \qquad\qquad Eq.(17)$$

$$A = \frac{1}{T_1}$$

$$B_{1 \to 0} = \frac{A}{8\pi hc\nu^3} = B_{0 \to 1}$$

In this set of equations T_1 is the excited state lifetime (which is 1 ns for these simulations), h is the plank's constant, c is the speed of light, n_1 is the excited state population, n_0 is ground state population, I_{IR} is the intensity, and ν is the frequency of laser in wavenumbers. For the Si-H stretch of our model system, the excited state does not show any degeneracy; therefore, the B coefficients for the spontaneous emission and the absorption are equal.

To retrieve the time dependent ground state population, Eq. 16 is used with the boundary condition that all the population is in the ground state at the start. The results for $n_0(t)$ using a 21 ps long pump IR pulse are shown in Figure 8. The IR is considered a square pulse for this calculation. Furthermore, the Si-H sites are considered to be ideal absorbers. These results indicate that the fractional population drops under the action of the pump IR, asymptotically reaching 0.5 by the end of the pulse.
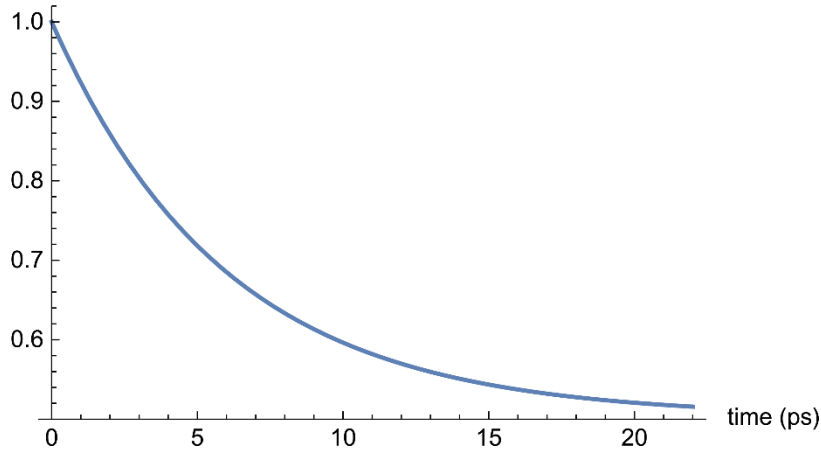
Figure 8: Ground State population for a system with 1 ns lifetime using Pump IR with $500 \frac{J}{m^2}$ fluence.

Another important feature is the intensity dependence of the ground state depletion. In the optical setup for these experiments, as described in chapter 2, the pulse duration is fixed at 21 ps by the main laser. However, the pump IR intensity can be varied. Furthermore, in the experimental setup the intensity varies across the beam cross-section which results in spatial variation of the GSD. Therefore, the dependence of fractional population and SFG on the pump IR intensity is simulated with the condition that pump IR of a given intensity acts for 21 ps. The results are shown in Figure 9 and Figure 10.
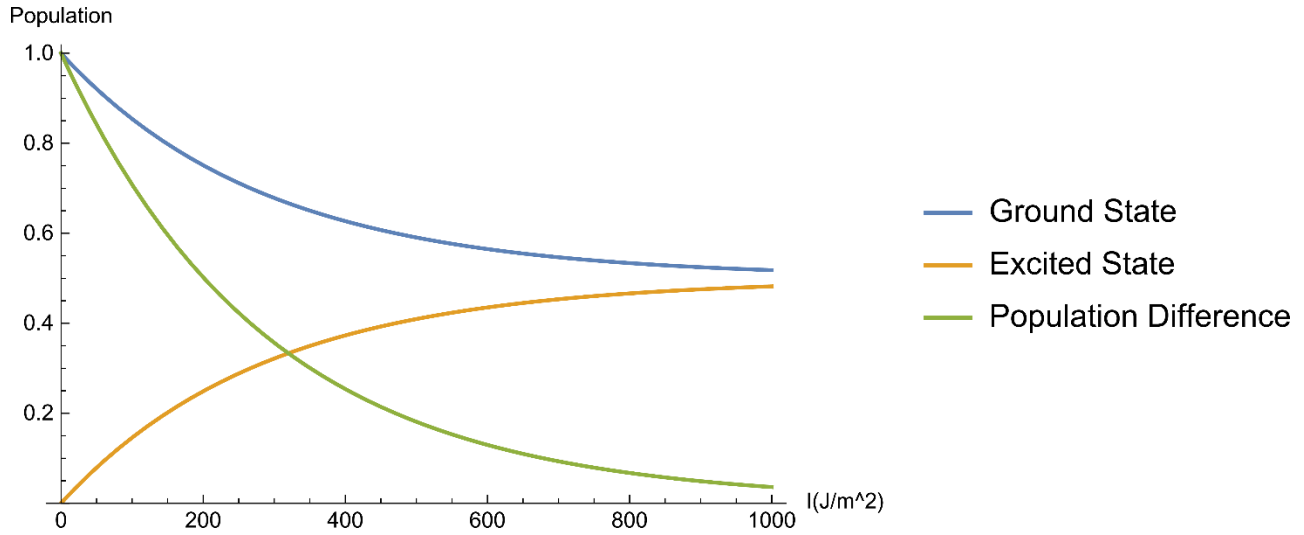
Figure 9: The fractional populations after pump IR acts for 21 ps.

In Figure 9, both fractional populations asymptotically reach 0.5. As a result, the population difference approaches zero. From Eq. 13 the SF signal is proportional to the square of the population difference. Therefore, in Figure 10 the normalized SF signal from the probe IR-visible pair drops to zero.

The delay between the probe IR-visible pulse pair producing the SF signals is not explored in these simulations. For SFG, the delay between the two must be within T_2 (the coherence lifetime of the vibrational excitation). Traditionally in SFG, the IR and the visible are both incident on the sample

simultaneously without any relative delay. However, if the delay is larger than the coherence lifetime, the SF signal will not be produced even with ground state population intact [63, 66].
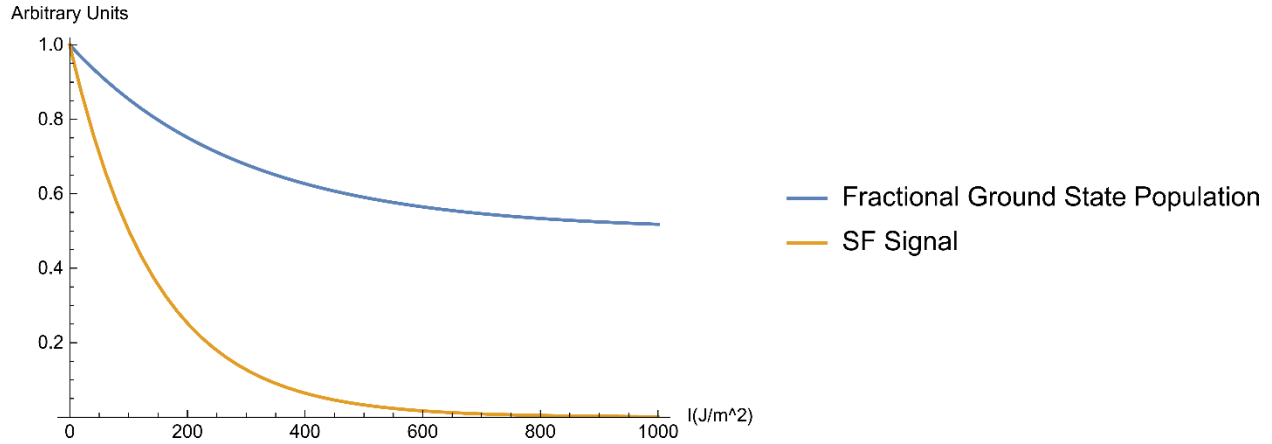
Figure 10: Probe SF signal intensity as a function of pump IR intensity after the pump IR acts for 21 ps.

3.3.2 Spatial Profile Function

The simulations performed so far have focused on the temporal evolution of the ground state population and the associated SF signal. However, the laser beams also show spatial intensity variation across the beam cross-sections. These changes give rise to spatial variations in GSD as well as SF production across the focused laser spots of pump IR, probe IR, and visible beams.

In Figure 11, the intensity profile of SF beam through the beam cross-section is shown. For this simulation, the probe IR is given a Gaussian profile with an arbitrary width and the visible beam is considered spatially flat. Experimentally this target can be achieved by focusing the probe IR and using collimated visible beam without focusing. This intensity profile for the SF signal generated by the probe IR and visible beams is called the spatial profile (SP).

SF Intensity (normalized units)
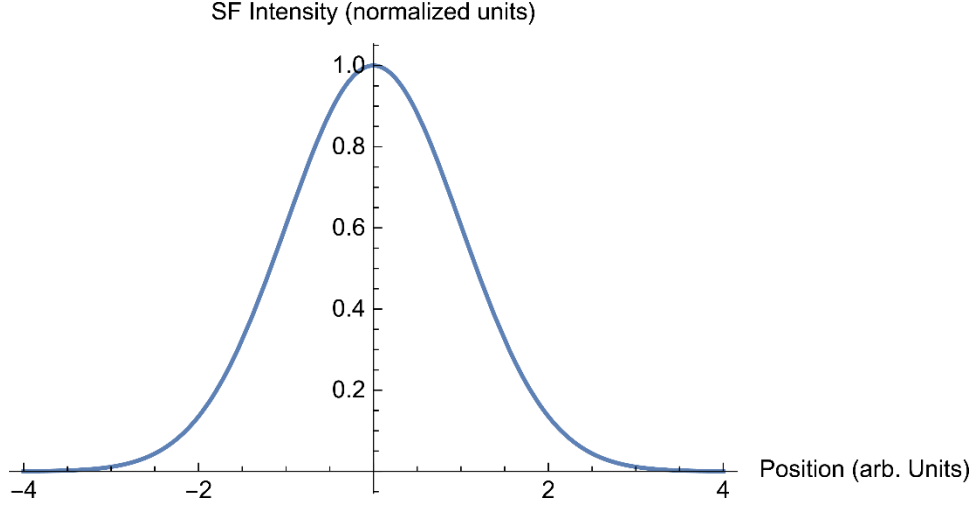
Figure 11: SFG from a Gaussian shaped Probe IR of an arbitrary width and a broad, collimated visible beam. The intensities of both beams are kept arbitrary.

The addition of donut shaped pump IR changes the spatial distribution of the ground state resulting in a modified SP for the SF signal. To simulate the donut shape, the pump IR is modeled by an arbitrary Bessel beam (Bessel beam of first kind) with an outer diameter similar to the diameter of the Gaussian probe IR beam. The results are shown in Figure 12. In this figure, the intensity profile for the donut shaped pump IR beam through the beam cross-section is shown in orange. Although the probe IR and visible beam profiles are kept the same, the SP for the SF signal changes.
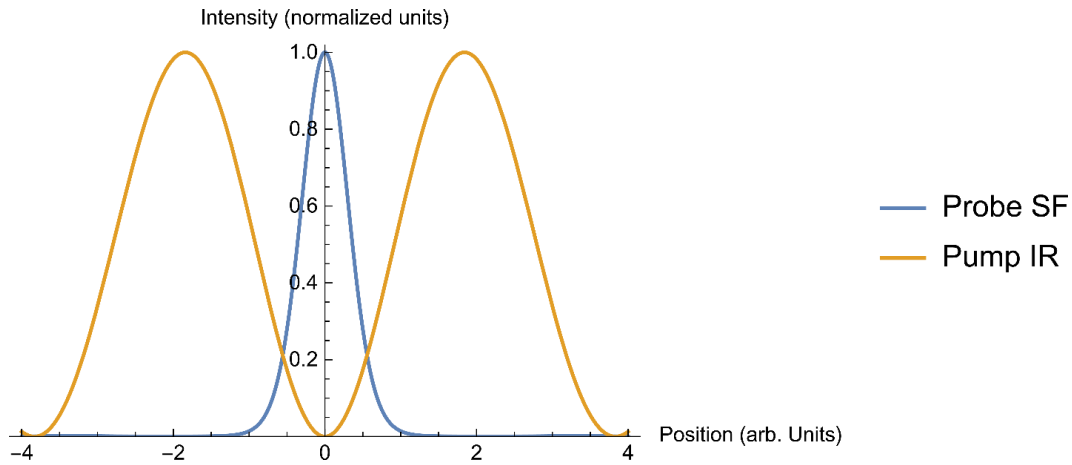
Figure 12: The probe SF intensity profile modified under the influence of pump IR. The outer diameter of pump IR is same as the outer diameter of probe IR in these simulations. The pump IR fluence used in this simulation is $1000\frac{J}{m^2}$.

For a clear comparison, the probe SF intensity profiles with and without pump IR are shown in Figure 13. These results indicate that the addition of donut-shaped pump IR, with a same outer diameter as the probe IR, leads to an improved resolution.
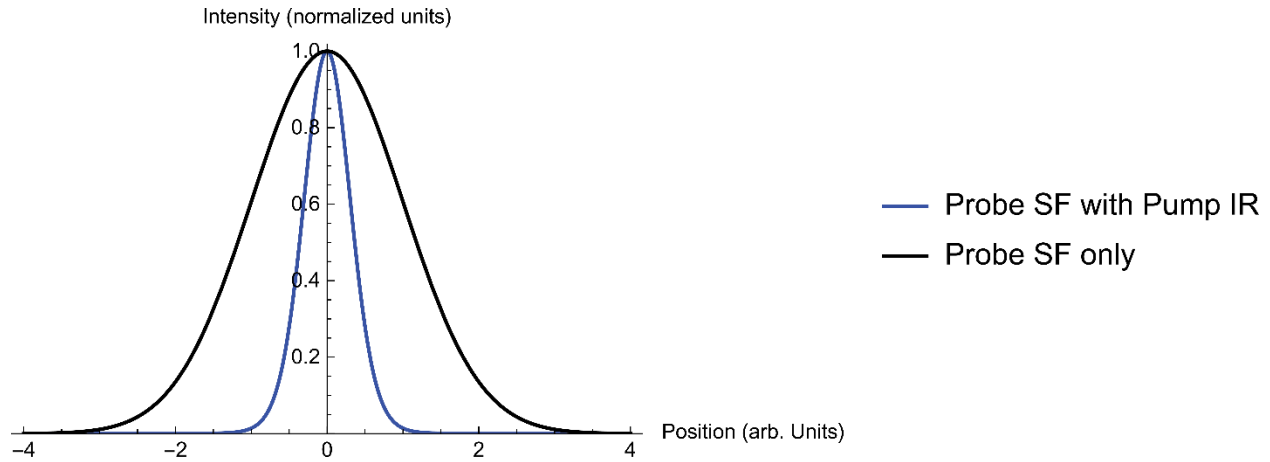
Figure 13: Comparison of probe SF profiles with and without the ground state depletion by pump IR.

3.4 Optical Setup

The top view of the optical setup for the super-resolution raster scanning microscope is shown in Figure 14. The xy-plane defines the horizontal tabletop and the z-axis runs vertical. The OPG/OPA provides the mid-IR and visible beams. The mid-IR beam received from the OPG is vertically polarized. At this wavelength, it is invisible; therefore, a guide beam provided by a 632 nm diode laser is combined with the mid-IR using a piece of double-side-polished germanium plate. This plate is placed at Brewster angle for the mid-IR to provide polarization purification as well.

Afterwards the mid-IR beam passes though a birefringent optics that can control the polarization of the mid-IR. Using this optic, the mid-IR polarization is rotated to generate horizontally polarized light. The mid-IR then passes through collimating 4F telescope that controls the divergence of the

beam. Typically, the telescope is configured to provide a beam waist of $1\ \text{cm}^2$. This collimated beam is then split into a pump IR beam and a probe IR beam using a CaF$_2$ wedge. The pump IR is composed of the portion that passes straight through the wedge whereas the probe IR is the primary reflection from the wedge surface. The tip-tilt of the wedge can be tuned to generate any combination of split ratios. Typically, the wedge is adjusted to proved 78 % power for the pump IR (85 µJ) and 10 % power for the probe IR (15 µJ). The remaining 12 % is lost in secondary reflections. The probe IR is sent directly to the sample and the pump IR makes its way to the sample after passing through a delay line.

The visible beam provided by the OPG/OPA is passed through a delay line to compensate its temporal mismatch with the mid-IR. In this delay line, the visible beam passes through a combination of half wave plate and linear polarizer. This pair controls the intensity as well as the polarization of the visible beam. Typically, it is configured to provide a horizontally polarized beam with respect to the optical table. Down the delay line, the visible beam passes through a collimating telescope that controls the divergence of the beam. Finally, the beam makes its way to the sample.

The sample is held in an upright position with sample surface in laboratory xz-plane. The surface normal is along the y-axis. To insure correct tip-tilt of the sample, a back-reflecting guide beam is utilized. The pump IR, visible, and probe IR beams are incident on the sample in the xy-plane at $67°, 53°$, and $-67°$ (with respect to the surface normal), respectively. Both pump IR and probe IR are focused on the sample surface. The probe IR is focused with a $+75$ mm focal length CaF$_2$ lens. The pump IR is focused with a ZnSe custom-built vortex-phase-plate lens that has a focal length of $+75$ mm. Details of the vortex-phase-plate lens are described later. The visible beam reflected

off the sample surface is sent to a pinhole target for marking the correct position for the sample along the laboratory y-axis. The sample is placed on a 3-axis motorized stage with tip-tilt adjustments.
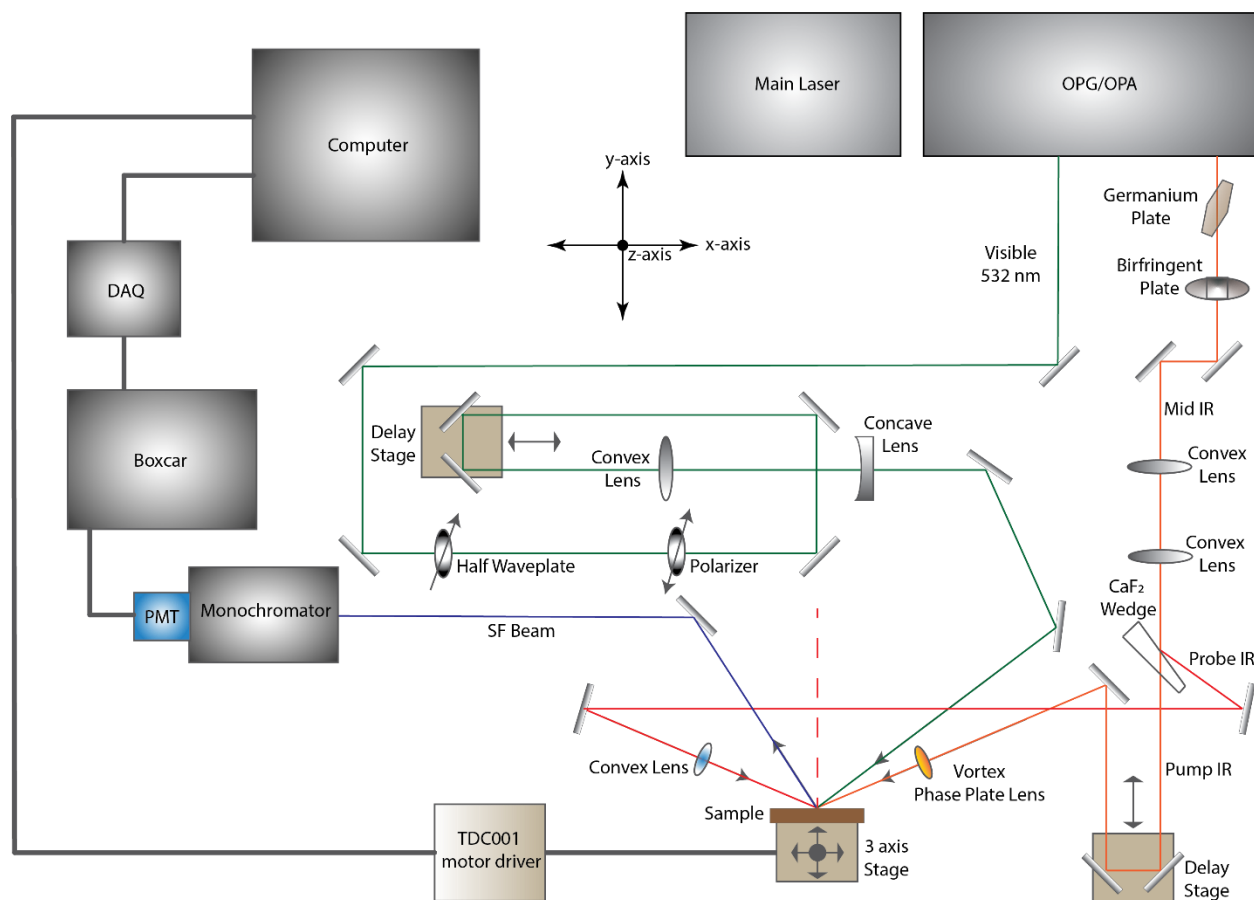
Figure 14: Top view of the optical setup for super-resolution raster scan microscope. X and Y axis are in the horizontal plane. Red, orange, and green lines represent the probe IR, the pump IR, and the 532 nm visible beams, respectively. The SF signal is shown in blue.

For multiple chemical systems, e.g., the surface hydrogen on silicon used in this study, the SFG requires the input visible and/or IR beams to have an electric field component normal to the sample surface (i.e., along laboratory y-axis). Such a requirement rules out any normal-incidence geometries. Therefore, the visible and mid-IR beams are incident at steep angles of 67° and 53°,

respectively. However, this oblique incidence elongates the focal spot shapes in the plane of incidence by a factor of 2.5. To ensure a proper geometric overlap, both pump and probe IR beams are incident at same absolute angle.

The SF signal generated by the counter propagating pair of probe IR and visible beams, is sent directly to a monochromator that filters any unwanted stray light. The filtered SF light is then detected by a PMT. The output current from the PMT is then registered by a computer using the procedure described earlier in chapter 2. In the computer, homebuilt LabView programs implement the experiment.

3.5 LabView and Motion Electronics

There are two main LabView programs written for this project. One of them is utilized for performing SFG spectroscopy and the other one is used for performing raster scan microscopy with fixed mid-IR wavelength. The code for both these programs is given in the appendix.

The SFG spectroscopy program scans the mid-IR wavelength by tuning the OPG/OPA and simultaneously records the SF signal. It is capable of plotting individual as well as average spectra. The front panel for this program is shown in Figure 15. The logical flow of the processes taking place in this program is shown in Figure 16. The program configures OPG/OPA software to the user specified mid-IR scan range and speed. As the OPG/OPA starts scanning the IR frequency, the program starts records the Boxcar output through DAQ along with the current IR frequency. At the end of the scans the data is saved, the parameters are reset, and OPG/OPA is brought back to the starting IR frequency.
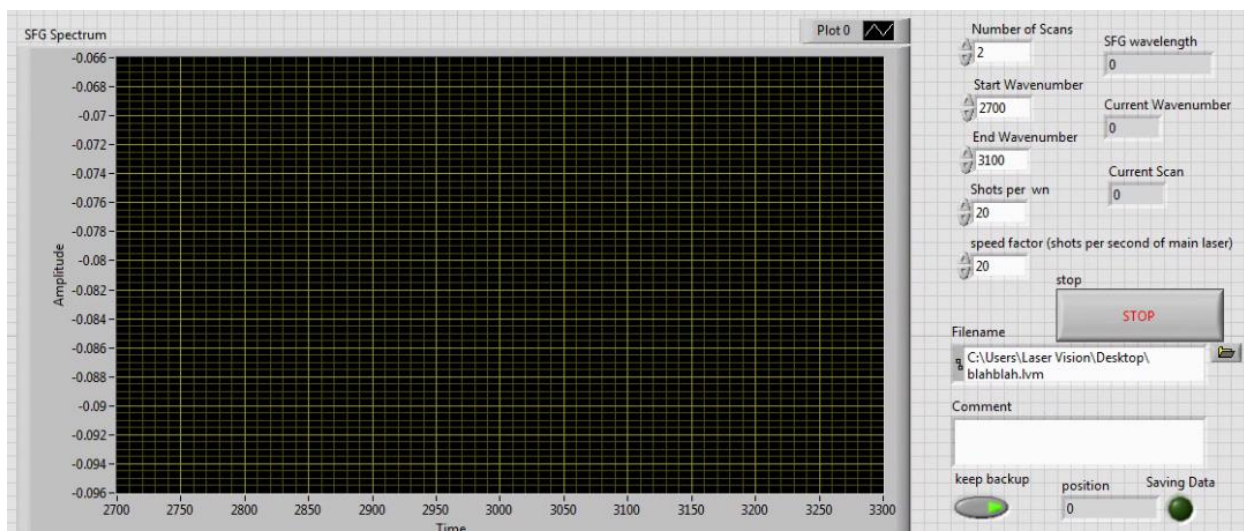
Figure 15: Front panel of LabView program created for collecting spectra. The x-axis represents IR wavelength and the y-axis shows SF signal amplitude.

Figure 16: Logical flow of steps for SFG spectrum collection program.

The sample is placed on a 3-axis translation stage in which the z-axis is motorized using ThorLabs Z825-B motor. This motor is driven by a Thorlabs TDC001 Driver, which is controlled by the homebuilt LabView program for raster-scanning microscopy. The smallest possible step on this stage is 29 nm [97]. The raster-scanning microscopy program scans the sample position along the z-axis and collects the probe SF signal from each point. Figure 17 shows the front panel of the program.
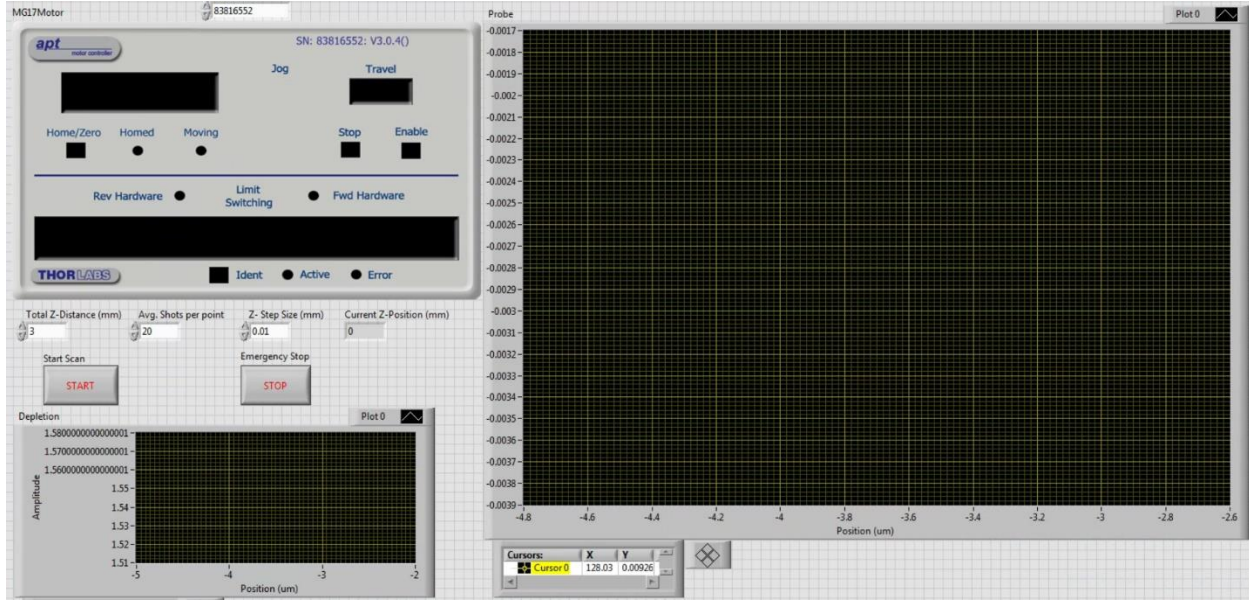
Figure 17: Front panel of LabView program for raster scanning SFG microscopy.

The logical flow of the main processes in this program is shown in Figure 18. The overall procedure is initiated by starting the motor-controller software and setting the correct parameters in the TDC001 drive for the stage and the motor. Afterwards, the user-defined scan range, step size, and average number of laser shots for each step are configured. Once these parameters are set, the scan starts. During the scan, as the sample moves along the vertical z-axis direction, the probe SF signal is collected and plotted at each sample position. At the end of the scan, the data is saved and the scanning parameters are reset. In this approach, increasing the pulses per point increases the SF signal and the total scan time.
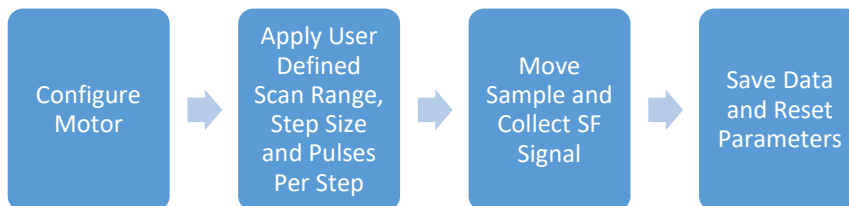
Figure 18: Logical flow of processes inside LabView raster scanning program.

3.6 IR Beam Alignment Procedure

The performance of GSD based super-resolution raster-scanning microscopy technique is crucially dependent on the precise overlap of the pump IR, probe IR, and the 532 nm visible beams. Since both pump IR and probe IR are in the mid infrared region, they are invisible to a human eye as well as most imaging devices. Although a 632 nm guide beam is combined with the mid-IR in the optical setup, it only serves as a general guide and helps to ensure rough alignment. The two are slightly separated as they pass through refractive elements in the optical setup. Furthermore, the focal spots for both pump IR and probe IR are considerably small, making it impossible for the naked eye to ensure precise overlap of the two. Therefore, it is important to have a scheme for imaging the focal spots of both pump and probe IR on the sample surface.

The mid-IR light can be converted into visible light with a detectable intensity using SFG process in nonlinear crystals such as KTP. This process is called 'upconversion' and it has been utilized in multiple mid-IR imaging devices [98-100]. In these devices the mid-IR light is combined with a visible or near IR light inside a nonlinear crystal. The high SFG efficiency of the crystal produces a visible SF light that is then imaged by a regular CCD camera. However, the crystals utilized in these devices often need to be precisely oriented to produce the required SF signal. Furthermore, for this microscope, the beam profiles on the sample surface are required. Therefore, a thin film of KTP power is utilized as an upconversion target for imaging both probe IR and pump IR beams. The powder is composed of KTP microcrystals. As a result, there are always multiple particles that are oriented in the correct direction for upconverting mid-IR. Consequently, the KTP powder target does not need to be oriented in any particular direction for mid-IR beam profiling.

Using the KTP powder target, the mid-IR imaging scheme is shown in Figure 19. On the KTP powder film, the 532 nm visible is combined with pump and probe IR beams to produce a visible SF light, which is then imaged by a combination of 10X objective and a CCD camera. The 532 nm visible fills the entire filed of view. The pump and probe IR beams are focused; therefore, the intensity profile of the SF light depends only on the intensity profiles of the pump and probe IR beams. Using this imaging technique, one can ensure the spatial overlap and correct beam profiles for both pump and probe IR in this super-resolution raster scanning microscope.
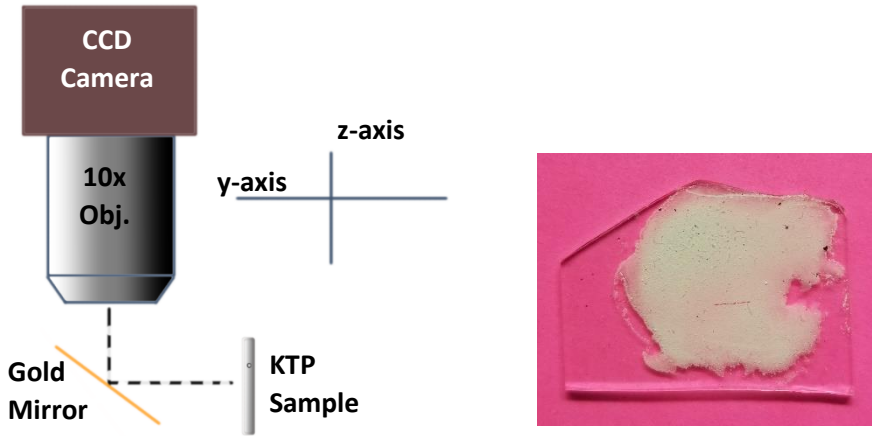
Figure 19: KTP sample scheme for visualizing and ensuring beam shape, quality, and overlap at the sample position. The inset (right) shows KTP sample.

3.7 Beam Shaping

As described in the super-resolution scheme and simulation earlier, the pump IR beam must be shaped in the form a donut. The required beam shape is achieved by a custom-built ZnSe vortex-phase-plate with an inbuilt convex lens of +75 mm focal length. The phase-plate imparts different phase to different sections of the beam passing through it. At the focal spot, these sections of the beam interfere with each other to produce a dark region in the center through destructive

interference. The simulation results for the phase-plate provided by the manufacturer are shown in Figure 20. In this simulation, the beam is propagating along the z-axis and the focal spot is observed in the xy-plane. This geometry is different from the one utilized in the optical setup for the super-resolution microscope where the beam is traveling in xy plane and the focal spot is imaged in xz plane at 67° incidence angle.
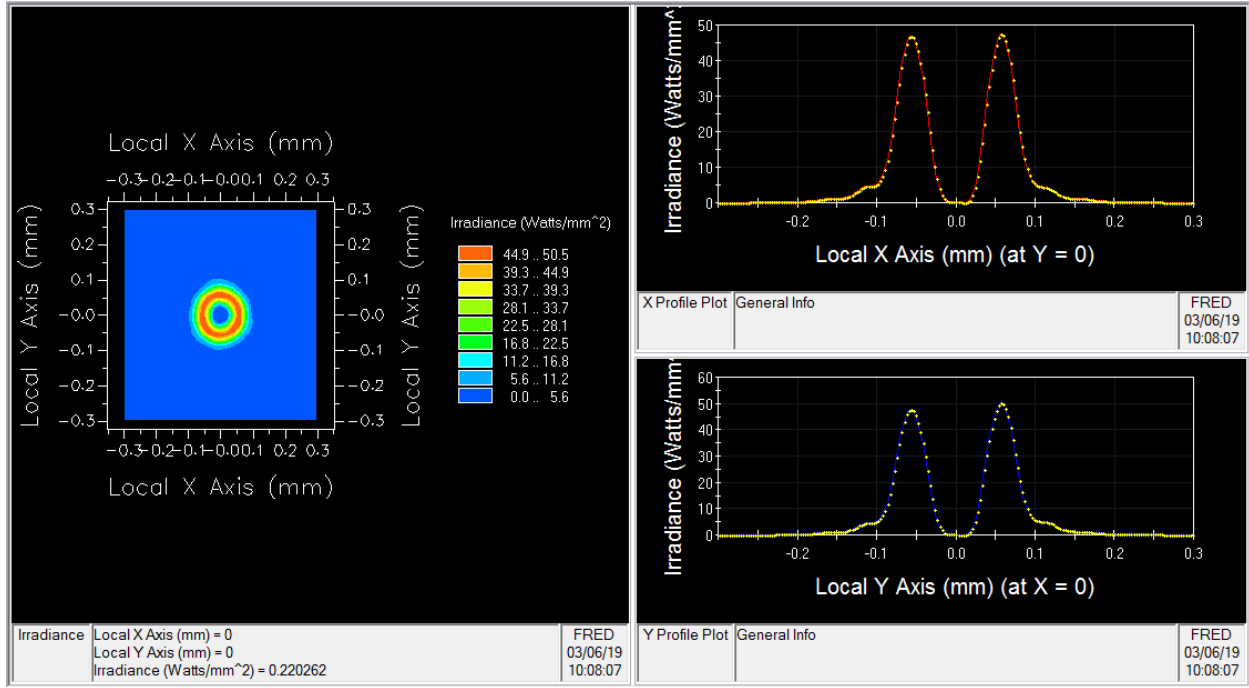
Figure 20: Simulation results for the phase-plate focal spot for normal incidence. The beam is traveling in z direction and the focal spot is observed in xy-plane (left panel). On the right the two panels show line profiles for the intensity along x-axis (top) and y-axis (bottom). The input beam is considered Gaussian with 1 cm diameter [101].

The left panel shows the focal spot for a normal incidence geometry on the surface in xy-plane. The right two panels show line profiles for intensity along x-axis (top) and y-axis (bottom). The Input beam has 1 cm diameter. The donut shape at focal spot has an outer diameter of 200 μm and an inner diameter of 50 μm.

Due to oblique angle of incidence in the current application, different portions of the focused beam reach the sample at different distances from the lens. Therefore, it is important to have a simulation for the Raleigh length of the donut. The results provided by the manufacturer are shown in Figure 21. The results show a Raleigh length of $\sim$500 μm. This ensures that in oblique incidence the beam shape and quality will not be compromised.

In the setup, the real pump IR beam shape produced by the phase-plate and the probe IR beam shape on the KTP powder sample are shown in Figure 22. Since beams are incident on sample surface (xz-plane) in an oblique geometry in the xy-plane, their shapes are stretched along horizontal x-axis. However, the profiles are not distorted along the vertical z-axis; therefore, along z-axis, they match with the simulation results shown earlier. The uneven bright and dark spots in these images are the result of inhomogeneities and roughness of the KTP powder film.
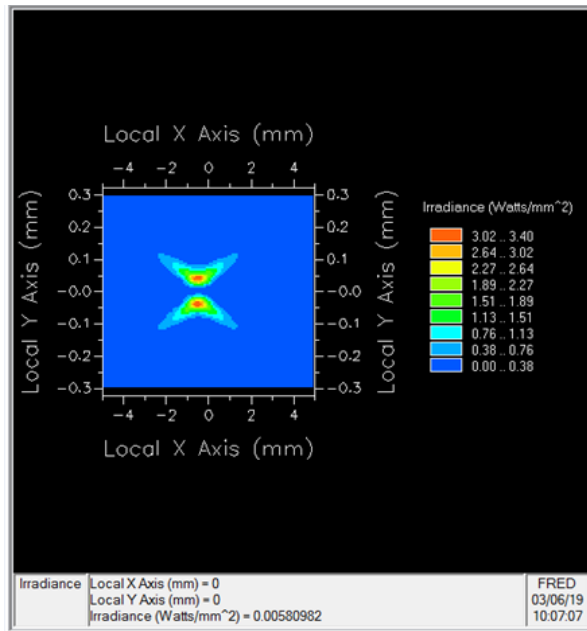
Figure 21: Intensity profile in the plane of incidence [101].
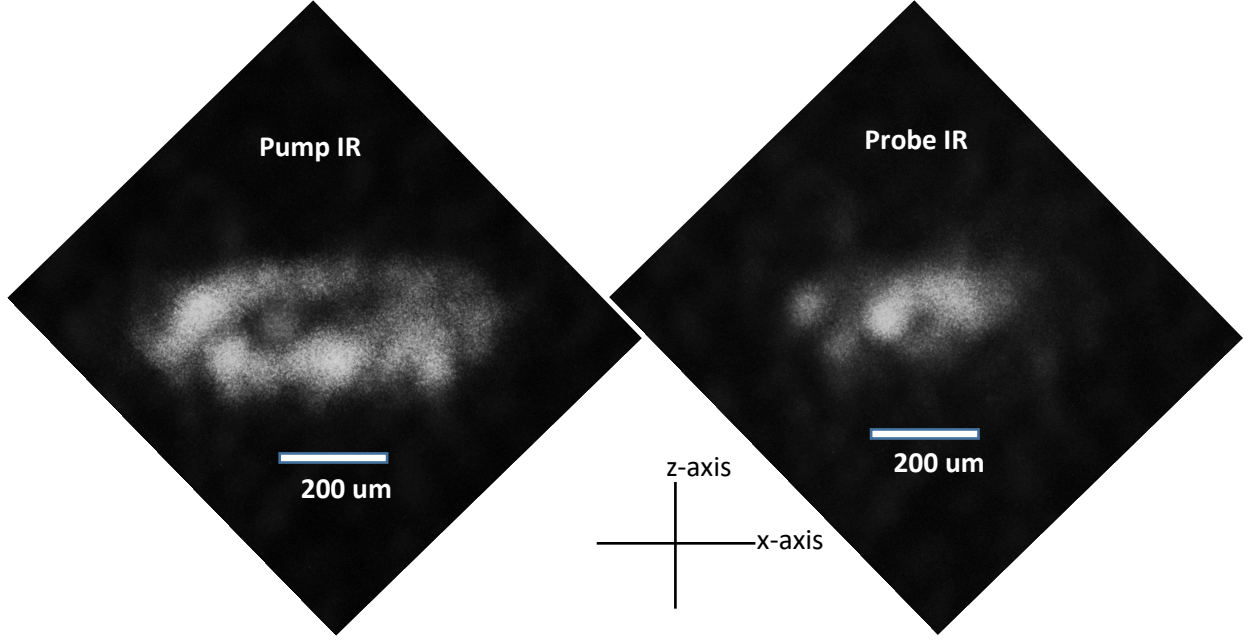
Figure 22: Beam profiles on KTP powder sample. The profiles are stretched along x-axis due to oblique angle incidence.

The average intensity profiles along the vertical z-axis are shown Figure 23. These profiles are obtained by utilizing the pixel intensities in the stripes marked by the yellow regions. These stripes pass through the center of the pump IR and probe IR focal-spot images. For each stripe, the pixel intensities along horizontal x-axis are averaged to generate the profiles shown in the bottom panel. These intensity profiles indicate that the required beam shapes are achievable. However, the pump IR intensity in the center of the profile is not zero. Either this can be from an artifact of the imaging technique or a real non-zero intensity in the center of the donut-shaped pump IR beam. The imaging artifact can arise from the uneven surface of KTP powder and defocusing of the camera lens used to image the surface of the KTP powder. These factors can be controlled by using a KTP powder sample with better surface quality and an improved imaging capturing system. Furthermore, the pump IR can be cleaned with a pinhole system before the vortex optics to ensure a proper Gaussian beam because the vortex optics' design requires a Gaussian beam input.
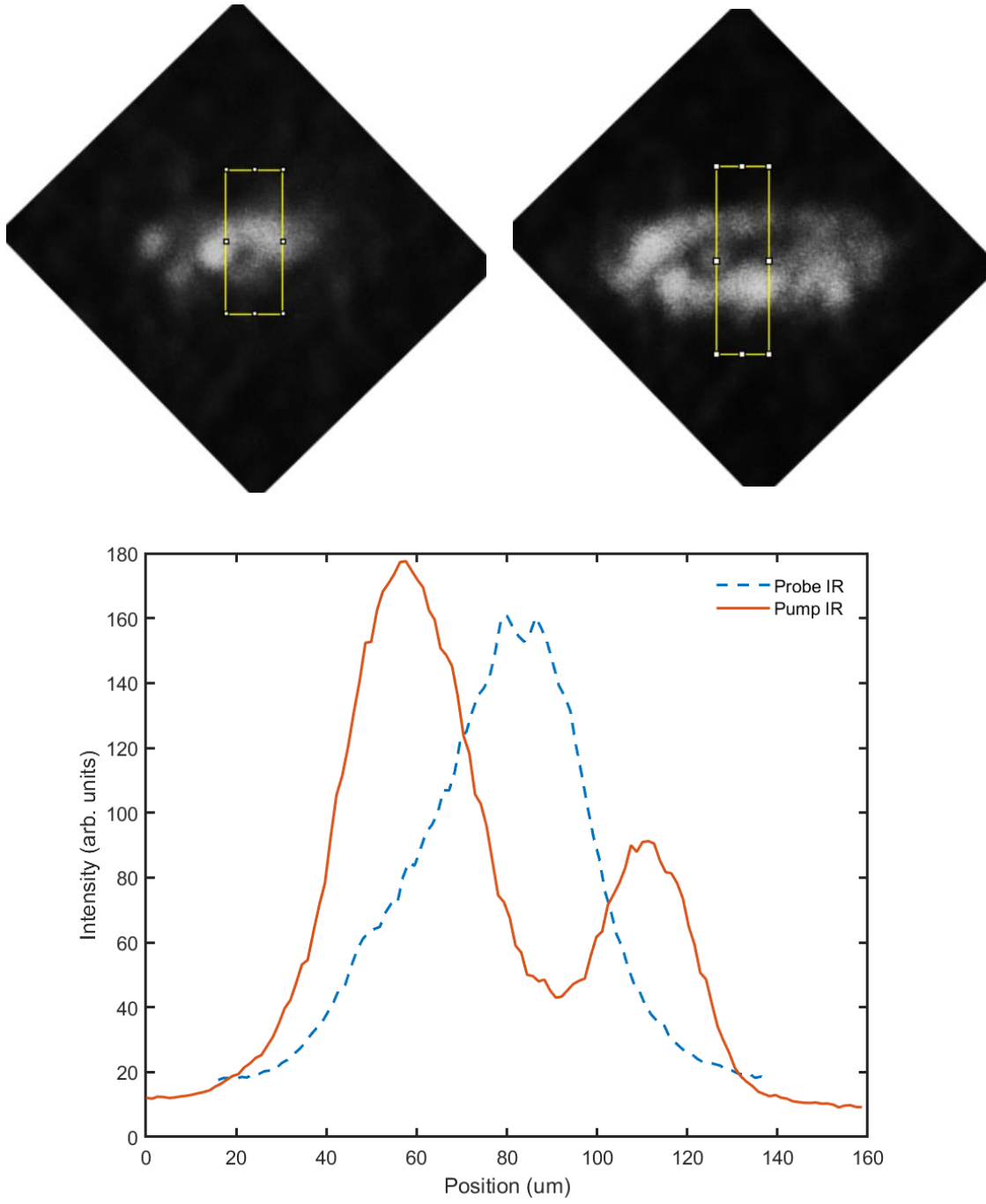
Figure 23: Average intensity profiles along the vertical z axis for the pump and probe IR. On the top, the regions selected for generating the pump and probe line profiles are indicated by the yellow outlines. On the bottom, the average vertical profiles through the center of the two beams are plotted.

Chapter 4

Resolution Enhancement: Results

In this chapter, the performance of super-resolution microscope is tested with a chemical system. The sample edge is scanned using the SF from the probe IR and visible beams. Two types of scans are collected with pump IR turned ON and OFF. The intensity profiles acquired from these two experiments are then analyzed to extract the effective resolution for the two raster scans.

4.1 Sample

The GSD based super-resolution raster scanning SFG microscopy was put to test using a hydrogen terminated silicon surface as sample. The silicon substrate had 111 orientation. On this surface, each Si atom is covalently bonded to one hydrogen atom. The system shows only a single Si-H stretch vibration at 2073 cm^{-1}. In this wavelength range, the silicon substrate is transparent, as a result the sample can handle high mid-IR intensities of the focused pump and probe IR. Furthermore, the system does not show any nonresonant SFG signal. Only a strong resonant SFG is observed when IR is at 2073 cm^{-1}. The lifetime of this vibration is 1 ns at room temperature, which is ideal for GSD using the 21 ps long laser pulses available in this experiment [65, 66].

The sample can be oxidized, however, it can survive for up to half an hour without any noticeable degradation in SFG resonant or nonresonant signals under ambient conditions. With sufficient exposure to the environment, a thin oxide film starts developing because of oxidative sample degradation. This film generates an intense nonresonant background SF. Therefore, whenever possible, the sample is kept in an ultra-pure nitrogen environment.

42

The sample preparation procedure is described in multiple publications [102-105]. The process used for this study is outlined in the Figure 24. The Si(111) sample is cleaned by sonication in acetone and then in water for 15 min each. Afterwards the sample is oxidized in freshly prepared piranha solution for at least half an hour. This process generates a think oxide layer on the silicon surface. The sample is then rinsed with ultra-pure Milli-Q water to remove any acid from the surface. Meanwhile a 30 % NH_4F aqueous solution is de-oxygenated by bubbling ultra-pure nitrogen for half an hour. The freshly rinsed silicon sample is then dipped in the NH_4F solution. In this solution, the oxide layer is etched for 10 min. The etching process terminates the silicon with surface hydrogen. Finally, the sample is removed from the solution and blow-dried with nitrogen.
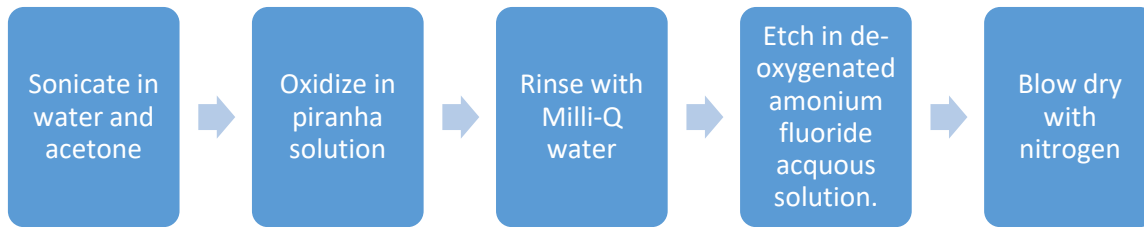
Figure 24: Preparation procedure for hydrogen terminated silicon surface.

Two sets of experiments were performed. The first set tested the GSD and associated SF signal suppression achievable with the optical setup. The second set confirmed the resolution enhancement.

4.2 SFG Signal Depletion

The resolution enhancement for the modified raster scanning microscope critically depends on the quantity of the GSD and associated SF signal suppression. Therefore, GSD experiments were

performed on the Si(111):H sample. If the pump IR is incident on the sample at the same time as probe IR-visible pair, it will generate SF signal of its own. This signal can leak into the detection setup designed for detecting SF associated with probe IR-visible pair. However, if the pump IR and the probe IR-visible pair are separated by T_2^*, i.e., the decoherence time for the Si-H stretch, the SF production form the pump IR vanishes. The decoherence time provides the timescale for the loss of coherent oscillation of the induced polarization in the Si-H population. For this vibrational mode, it is 33 ps [65, 66]. Therefore, in these GSD experiments, the pump IR reached the surface 33 ps before the probe IR-visible pair. The Si-H stretch show a vibrational lifetime of 1ns, which implies that each Si-H can stay excited for a far longer duration than the decoherence time; therefore, a 33 ps delay did not affect the ground state population dynamics considerably.

Both pump and probe IR were focused on the sample surface with $+75$ mm CaF_2 lenses. The pump IR and probe IR contained 85 μJ and 15 μJ energy per pulse, respectively. To avoid sample damage, the visible beam was not focused and its intensity was kept as low as possible. The Si(111):H sample was prepared and placed in a cell purged with ultra-pure nitrogen. The cell was fitted with CaF_2 windows for the input and output laser beams. SF spectra were alternatively collected with pump OFF and pump ON. The results are shown in Figure 25.

These spectra indicate that the SF signal lacked a nonresonant contribution and displayed only one single strong resonance peak at 2073 cm^{-1}. Since the lifetime of Si(111):H vibration is about 1 ns, the natural linewidth of the spectral peak is sharp; however, the broadening observed in Figure 25 was due to the broad frequency distribution in the mid-IR generated by the OPG/OPA.
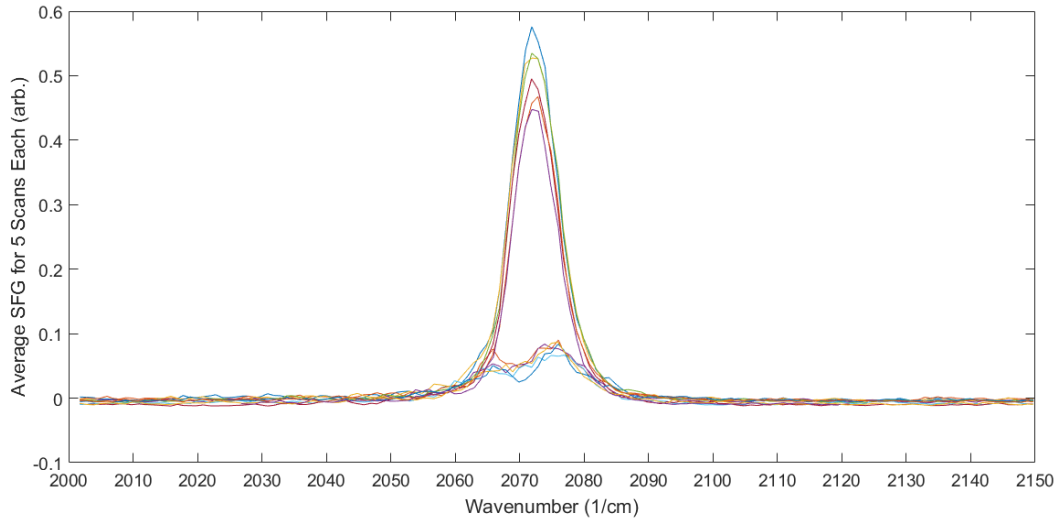
Figure 25: Probe SF spectral scans with Pump IR ON and OFF. Starting with pump OFF, the successive scans alternate between pump ON and pump OFF. The 1st pair of scans is blue, 2nd green, 3rd yellow, 4th orange, 5th red, and 6th purple. The decrease in peak intensity across successive scans is due to the sample damage induced by the incident beams.

When the pump IR was ON, the resonant SF signal dropped. The dropped SF signal shown in Figure 25 has a M-shaped spectral profile with a dip at $2073 \, \text{cm}^{-1}$. To understand this shape, consider that at any given wavenumber, the OPG generates a mid-IR output with a spectral distribution where most power is concentrated in the central frequency. The Si-H stretch has a sharp resonance frequency (due to its 1 ns long lifetime). When OPG's central frequency is matched with the resonance frequency of the Si(111):H stretch, maximum population is pumped out of the ground state due to increased relevant pump IR intensity. When the central frequency is in the neighborhood of the resonance frequency, there is a relatively small fraction of intensity at $2073 \, \text{cm}^{-1}$. The GSD induced by this intensity is not as complete as in the previous case. Therefore, due to non-linear dependence of the SF signal on the ground state population (Chapter 1, Eq. 14), the SF signal shows an M-shaped profile with a dip at $2073 \, \text{cm}^{-1}$.

45

The consecutive scans reveal that the resonant signal with pump IR OFF decreases with the passage of time. This indicates the degradation of the sample. Si(111):H can degrade through oxidation of the surface hydrogen by the atmospheric oxygen. However, in these spectra the associated nonresonant signal does not increase. Therefore, this degradation is non-oxidative in nature and could be laser-induced substrate damage. In conclusion, these results indicate that the probe SF can be depleted by 90 % at best, with the available experimental setup.

4.3 Resolution Improvement

The resolution for the probe SF was tested by scanning the edge of Si(111):H sample; since only the SF signal is detected, this created a chemically sensitive knife edge experiment for beam profiling. The mid-IR was set at the resonance frequency of the Si(111):H stretch mode. The pump IR beam was shaped with vortex-phase-plate to generate a donut shaped profile that was then imaged onto the KTP powered along with probe IR. The probe IR focal spot had a width of 200 μm along the z-axis and the pump IR had an outer and inner diameter of 200 μm and 50 μm, respectively. At 2073 cm^{-1}, the silicon substrate was transparent with a reflection of 2.6 % for 65° incidence; therefore, the pump and the probe IR energies were kept at 85 μJ and 15 μJ, respectively. The visible beam energy was kept at 35 μJ with a beam diameter and spot size of $\sim 1\ mm^2$. After ensuring the overlap and correct shapes of pump and probe IR, the KTP powder sample was replaced with freshly prepared Si(111):H sample. The experiment was performed in the open air to avoid any beam movement by the CaF_2 windows of the sample cell. Under these ambient conditions, the atmospheric oxygen can react with the sample and form a thin silicon oxide layer, which can degrade the GSD and compromise the resolution improvement. However, to limit the oxidation damage artifacts, the experiment was completed in less than half an hour.

The sample was brought into the laser beams by moving it along the z-axis with 10 μm steps and the SF signal was acquired for 40 shots at each step. The results are shown in Figure 26.
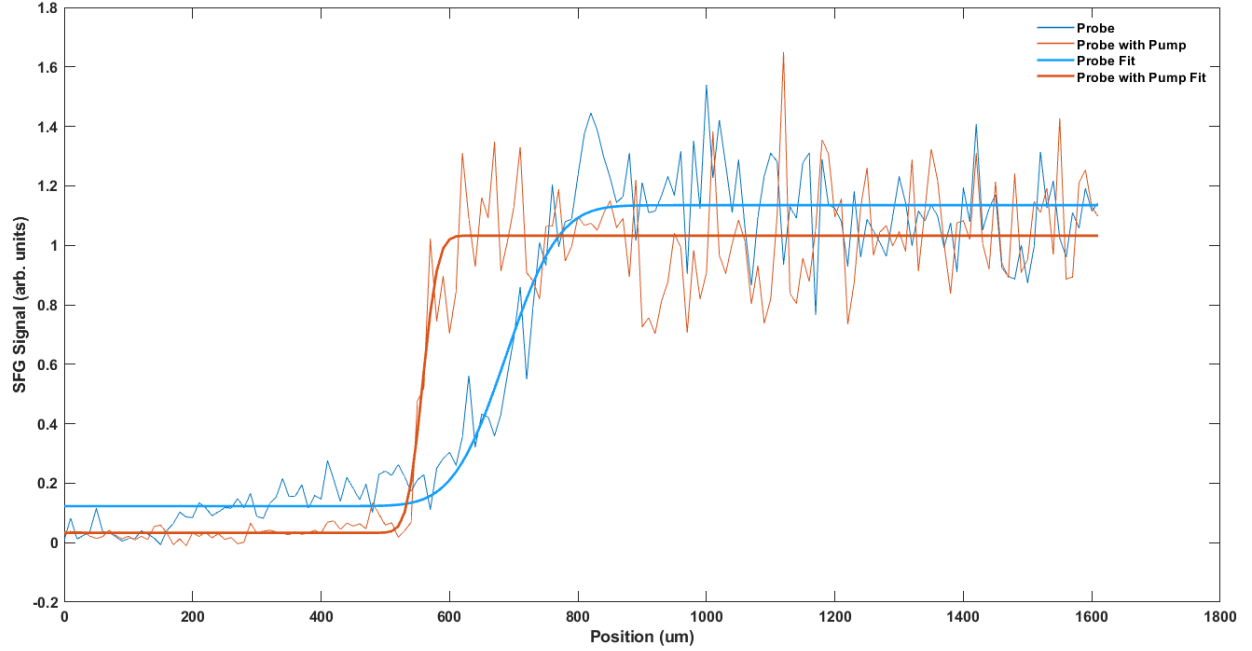
Figure 26: Step edge scan results with Si(111):H sample moved long the z-axis. The probe SF with pump IR OFF and pump IR ON are plotted along with curvefitting results.

First, the z-scan was performed with pump IR turned OFF. The collected SF signal is shown in blue. However, slight SF degradation from laser damage was observed after the scan. Therefore, the z-scan with pump IR turned ON was performed by slightly shifting the sample along x-axis. These results are displayed in orange.

The curve fitting was performed with cumulative distribution function of Gaussian distribution given by

$$\frac{a}{2}\left(1 + \text{erf}\left(\frac{x - \mu}{\sigma\sqrt{2}}\right)\right) + b \qquad Eq.\,(18)$$

where

$$\text{erf}(x) = \frac{2}{\sqrt{\pi}} \int_0^x e^{-t^2} \, dt \, . \qquad\qquad Eq. \, (19)$$

In these equations, the overall signal scaling and offset are summarized by parameters a and b, respectively. μ captures the center and σ represents the standard deviation of the Gaussian corresponding to this cumulative distribution. For this experiment σ indicates effective resolution. Therefore, an improved resolution will result in decrease in σ. The curve fitting results are summarized in Table 1.

Table 1: Curve fitting results for the edge scan of Si(111):H sample with probe SF

Parameter	Probe only	Probe with Pump
a	1.012	0.9993
b	0.1228	0.03323
μ	688 µm	557.9 µm
σ	64.64 µm	18.74 µm
$RMSE$	0.1258	0.1463
R^2	0.9366	0.9133

The low values of Root Mean Squared Error (RMSE) and high values of Residue Squared (R2) in the last two rows indicate good curve fitting for both scans. The a and b values of both scans suggest similar signal quality. There is slight shift in the recorded mean position of the beam i.e., μ, which results from an experimental shift in the starting z position.

The SP functions corresponding to the pump IR OFF and ON scans are shown in Figure 27.
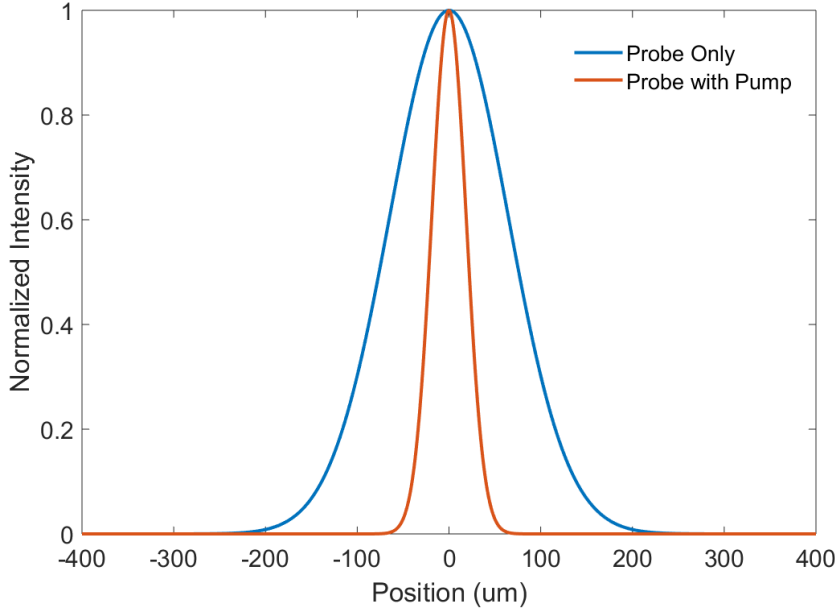
Figure 27: The spatial profiles calculated form the curve fitting performed on the probe SF knife-edge scan with and without pump IR.

These SP's show a resolution improvement of more than $3 \times$, proving the effectiveness of this super-resolution technique. The addition of pump beam changes the FWHM from $154\,\mu m$ to $44\,\mu m$, an improvement of $3.5 \times$.

4.4 Conclusion and Future Direction

The modified raster scanning system with structured pump IR beam shows promising resolution improvement for the SF microscopy. This resolution improvement stems from the depletion of ground state population from the peripheries of the probe IR focal spot. These results indicate a resolution enhancement by $3 \times$. Since the spot sizes are still much larger than the diffraction limit, this experiment serves as proof of concept for the super-resolution technique at this stage. Because

the central dark spot in the structured pump beam is not limited by the Abbe diffraction limit, these results can be further refined, and true sub-micron resolution can be achieved by using improved and specialized optics.

The IR laser beam can be cleaned in a 4F system with high power pinhole ($<$ 50 μm diameter) such as the ones available at Lenox Laser [106]. It would ensure a proper Gaussian profile for the IR beam that will result in improved focusing and beam shaping performance for the rest of the optical setup. The focusing lenses for the 4F system and probe IR can be replaced with Hybrid Aspheric lenses, which offer near diffraction limited spot size and high NA. These can be obtained for vendors such as Edmund Optics [107]. Finally, a vortex optics, which can produce sub micron vortex, can be acquired from II-VI Company (i.e., the vendor for the current vortex optics) [101].

The ultimate resolution limit for this technique will be determined by the sample's damage threshold and the detection limit of SF signal. In that regard, specialized detection techniques such as photon counting can serve as potential remedies. Although the sample studied in this work had a vibrational mode with very long lifetime, this technique can be extended to samples with short lifetime such as C-H stretch using femto-second lasers.

Chapter 5

SFG Studies of Rubrene Single-Crystal Surface

5.1 Introduction

Recently, electronic properties of organic materials have been a focus of research interest due to their ability to deliver flexible and efficient devices such as LED displays [108-112], light harvesting devices [113-117], and other electronic applications. Rubrene has been one of the extensively studied candidates due to its utility in Organic Light Emitting Devices (OLEDs) and Organic Field Effect Transistors (OFETs) [118-124]. Single-crystal rubrene or 5,6,11,12-tetraphenyltetracene, has shown high carrier mobility ($\sim 40 \frac{cm^2}{V.s}$), a desirable quality for enhancing OFET performance [125, 126]. As a result, multiple studies have been carried out to understand the crystal structure, charge transport, electronic states, and other optical and electrical properties [125-136].

Along with the crystal structure and bulk properties, rubrene's surface properties are also becoming increasingly important. For example, in OFETs, rubrene is often used in contact with Ionic Liquid (IL) dielectrics for superior performance. However, complex interactions on the IL – rubrene interface can affect the device performance. This necessitates the surface characterization of the rubrene single-crystals with chemical sensitivity. Traditionally, rubrene has been studied with either surface-selective (AFM, STM) [137-141] or chemically-sensitive (XPS, IR, Raman) techniques [142-146]; therefore, the required level of surface characterization has not been achieved.

In this chapter, an SFG analysis for a single-crystal rubrene is presented to understand the orientation of surface molecules.

5.2 Rubrene Molecular Structure

The rubrene molecule consists of a tetracene backbone with four phenyl rings attached to the two central rings of the backbone, two on each side. The molecular structure is shown in Figure 28 with molecular axis L, M, and N [147]. The L-axis runs along the length, M spans the width, and N goes perpendicular to the tetracene plane. The phenyl rings twist perpendicularly to the ML-plane as displayed in the center and right panels of Figure 28. The molecule is centrosymmetric with a C_{2h} symmetry group [147, 148].
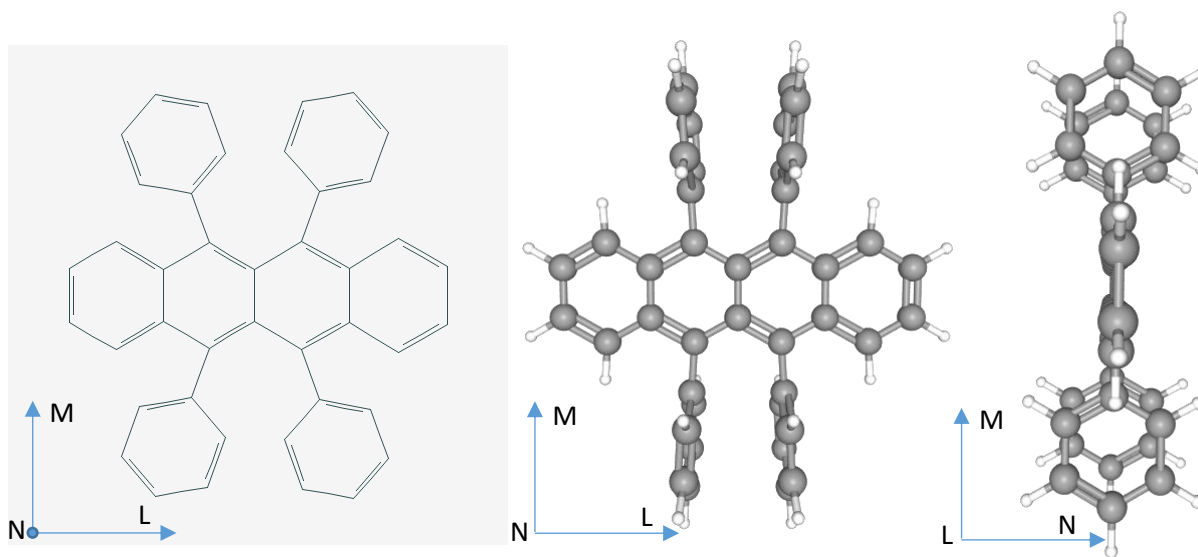
Figure 28: Molecular structure of rubrene. The basic bond diagram is on left. The center and right figures illustrate the molecular geometry in 3D.

5.3 Sample

The samples were provided by Dr. Okaue Daijiro from Surface-Interface Lab, Fukui Group, Osaka University. These were prepared by a vapor-transport method in which high-quality rubrene powder is vaporized in a higher temperature portion of a two-stage tube furnace. The vapors are then carried to a relatively cooler portion of the tube using a flow of inert gas such as argon. In the cooler portion of tube, the vapors condense to form reddish-orange or reddish-amber colored crystals with orthorhombic symmetry [149]. These crystals display largest crystal growth along a and b crystal axis. The c-axis, that is perpendicular to both a- and b-axis, shows minimum crystal growth; resulting in a thin flake like single-crystal samples. In ab-plane, the molecules are packed in a herringbone arrangement [150, 151].
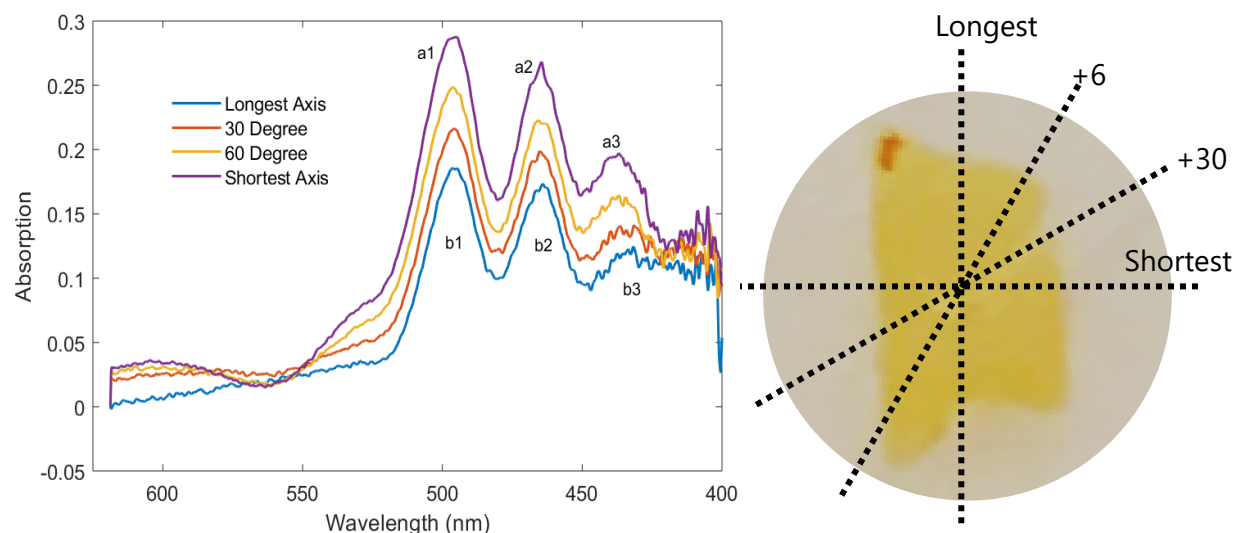
Figure 29: Rubrene single-crystal with the corresponding absorption spectrum. The absorption bands along a- and b-axis are represented by the purple and blue lines, respectively. The labels a_i and b_i indicate absorption peaks.

The sample utilized for rubrene surface-studies is displayed in Figure 29. It was about 20 μm thick with a ~2.5 mm length and a ~1.5 mm width. In such sample the crystallographic a- and b-axis are in the surface plane with c-axis perpendicular to the surface. To identify the a- and b-axis of

the sample, UV-vis spectroscopy was performed with light polarized along the length and width of the sample. From rubrene literature, the absorption along the three axis follows $A_a > A_b > A_c$; therefore, the a- and b-axis can be determined by looking at the azimuthal dependence of the absorption [147, 148]. The absorption profiles are shown in Figure 29. These profiles indicate that the a-axis is along the length and the b-axis is along the width. This leaves c-axis perpendicular to the surface. This assignment was matched with the crystal-growth literature for vapor-deposition of rubrene [147-152].

The crystal structure and the molecular arrangement for the rubrene sample were confirmed by Hamid Vali from Yang group at University of Houston. The characterization was performed with Reflection High-Energy Electron Diffraction (RHEED) at room temperature. The RHEED utilized electrons with kinetic energy of 30 keV, giving a de Broglie wavelength of 0.07 Å. The single-crystal surface was analyzed along different surface orientations (marked by in-plane indices h and k). The results are summarized in Table 2.

Table 2: RHEED analysis of the single-crystal rubrene surface performed along differed surface indices

(hk) in-plane Index	(31)	(21)	(32)	(11)	(23)	(13)
From fitting (Å)	3.98	5.19	2.88	6.36	2.26	2.33
Theoretical (Å)	3.99	5.09	2.86	6.44	2.27	2.36
Deviation %	+0.2	-1.9	+0.7	+1.2	+0.4	+1.3

These results indicate that the sample was a single-crystal with lattice parameters $a = 7.10 \pm 0.07$Å and $b = 14.4 \pm 0.07$Å. The surface of the sample was in ab-crystal plane with index (001) and the c lattice parameter was 26.8 ± 0.07Å. The molecules pack in a herringbone pattern in the

ab-plane (001 crystal facet) [152, 153]. The resulting unit cell is shown in Figure 30. The M-axis of the molecules is parallel to the crystalline c-axis. Furthermore, the molecules can be categorized into two groups, one with molecular L-axis rotated clockwise and the other with L-axis rotated anti-clockwise about crystalline c-axis.
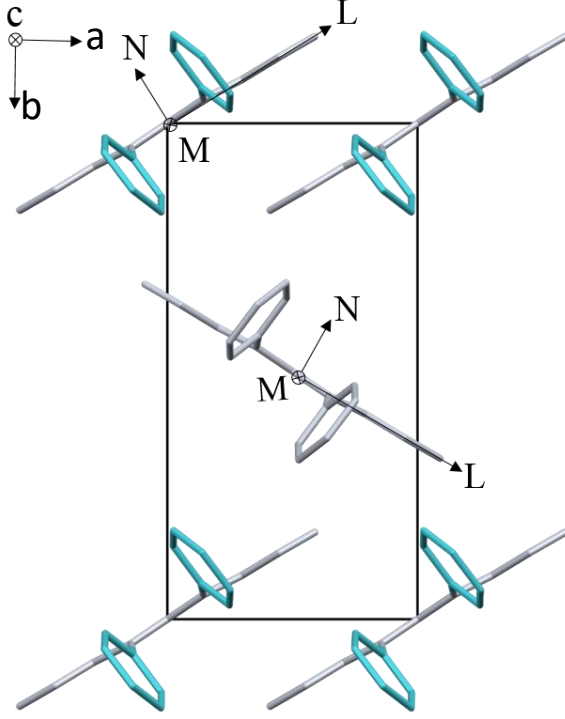
Figure 30: A unit cell in a single-crystal rubrene. The crystal axis are denoted by a, b, and c. The molecular axis are represented by L, M, and N.

The refractive indices for the three crystallographic axis follow $n_a \sim 1.7 < n_b \sim 1.9 < n_c \sim 2.0$. In the absorption spectra, peaks a2, a3, b2, and b3, arise from molecular transition with transition dipole predominantly along molecular L-axis [147, 148]. Therefore, the angle α between molecular L-axis and crystalline a-axis can be found from the absorption ratio between peaks a2 and b2 as well as peaks a3 and b3 using the following relation [147]

$$\frac{A_a}{A_b} = \cot^2 \alpha \qquad\qquad Eq.\,(20)$$

The a2 and b2 absorption peaks give $\alpha = 38.8°$, whereas a3 and b3 yield $\alpha = 38.2°$. Therefore, an average value of 38.5° is considered, which is in close proximity to the literature value (37°) [147, 148]. However, the orientation of the phenyl rings which project out of the surface, remains unknown. This orientation can be analyzed using SFG spectroscopy.

5.4 SFG on Rubrene

5.4.1 Experimental Technique

The SFG spectroscopy was performed with a specialized setup on the single-crystal rubrene with mid-IR scanned from 2700 cm^{-1} to 3200 cm^{-1}. The visible wavelength was held fixed at 532 nm. The sample was placed inside a rotatable cell with a 1 mm thick CaF_2 window. The cell was purged with ultrapure nitrogen to avoid photo-oxidation of the rubrene due to the visible laser and atmospheric oxygen [154, 155]. The experimental geometry is shown in Figure 31.

The visible and mid-IR beams were incident in the xz-plane of the laboratory frame-of-reference (Figure 31A) at 50° and 60°, respectively. The sample was placed flat in the laboratory xy-plane (Figure 31B). The sample was rotated in the xy-plane and the SFG spectra were collected at each step using two polarization combinations; in the first combination, the polarization of SF, visible, and mid-IR were all p-polarized with respect to the plane of incidence, this combination is termed PPP. For the second combination, the SF and visible were s-polarized, and the mid-IR was p-polarized with respect to the plane of incidence; this second combination is called SSP. These polarization combinations were selected because surface phenyl group systems similar to rubrene surface, exhibit insufficient SF signal for all other polarization combinations [156].

To avoid any systematic artifact, the data was acquired with randomized steps for a complete 360° rotation. The azimuthal angle sequence in the xy-plane was $0°, 30°, 60°, 90°, 150°, 240°, 330°,$ $120°, 210°, 300°, 180°, 270°, 360°.$
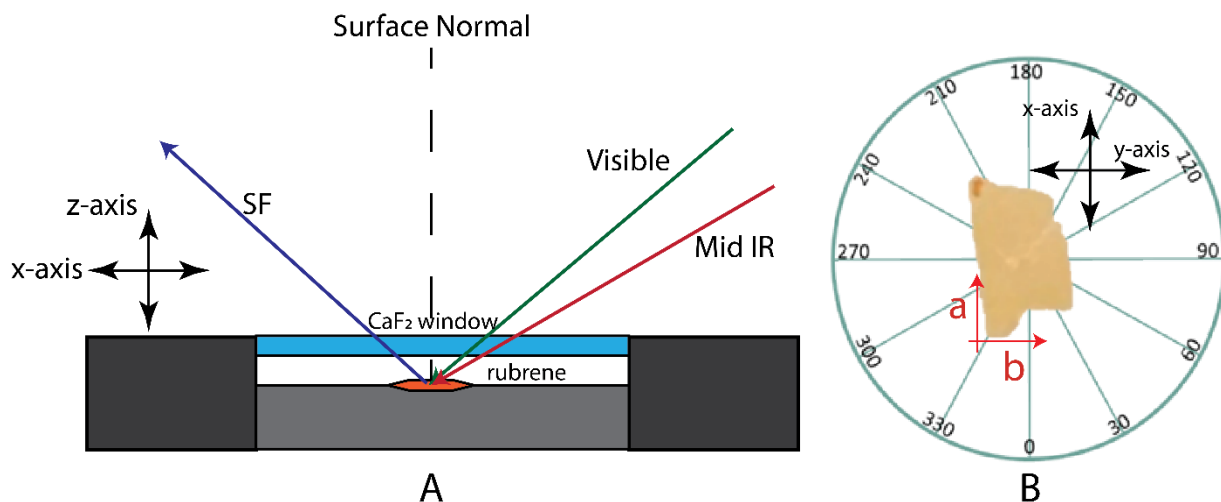
Figure 31: The SFG setup for the rubrene single-crystal. (A) shows experimental geometry in the plane of incidence i.e., laboratory xz-plane. (B) shows the top view of the rubrene sample in the rotatable cell. The surface of rubrene is in laboratory xy-plane and the surface normal is along laboratory z-axis for this study.

5.4.2 Results

The SFG spectra obtained from the PPP and SSP polarization combinations are shown in Figure 32 and Figure 33, respectively. Every spectrum in these two sets is an average of five scans. In PPP spectra, the nonresonant background SF displays a broad profile, which changes with sample rotation. On the other hand, in SSP spectra, the nonresonant signal is very low. In both PPP and SSP spectra, a main resonance peak/dip is observed around 3058 cm^{-1}.

Besides the main resonance peak, there are minor peaks at low frequencies in both PPP and SSP spectra. Their frequency range is in C-H stretch region for CH_3, CH_2, and CH groups. Since

rubrene molecules do not contain any such groups, these peaks are attributed to the organic contaminants on the rubrene surface.
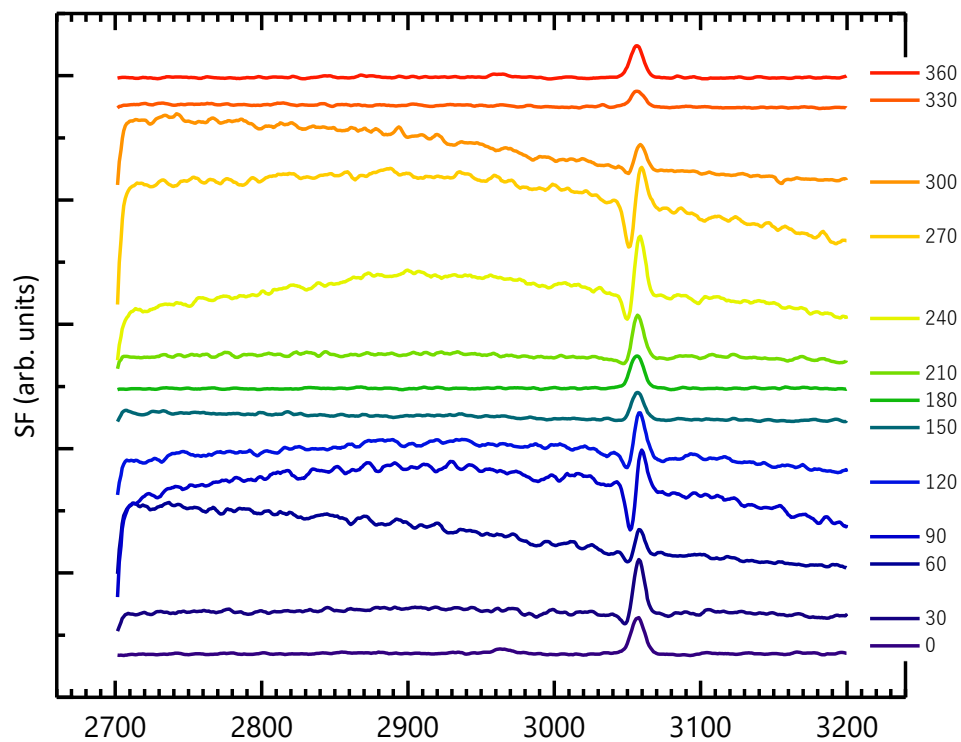
Figure 32: Rubrene SFG for PPP polarization combination. Each one of these spectra was collected at different azimuthal angle in the laboratory frame. The corresponding azimuthal angle is given on the right of each spectrum. The sudden fall in the nonresonant SF at the start is due to the cutoff of the signal detector.
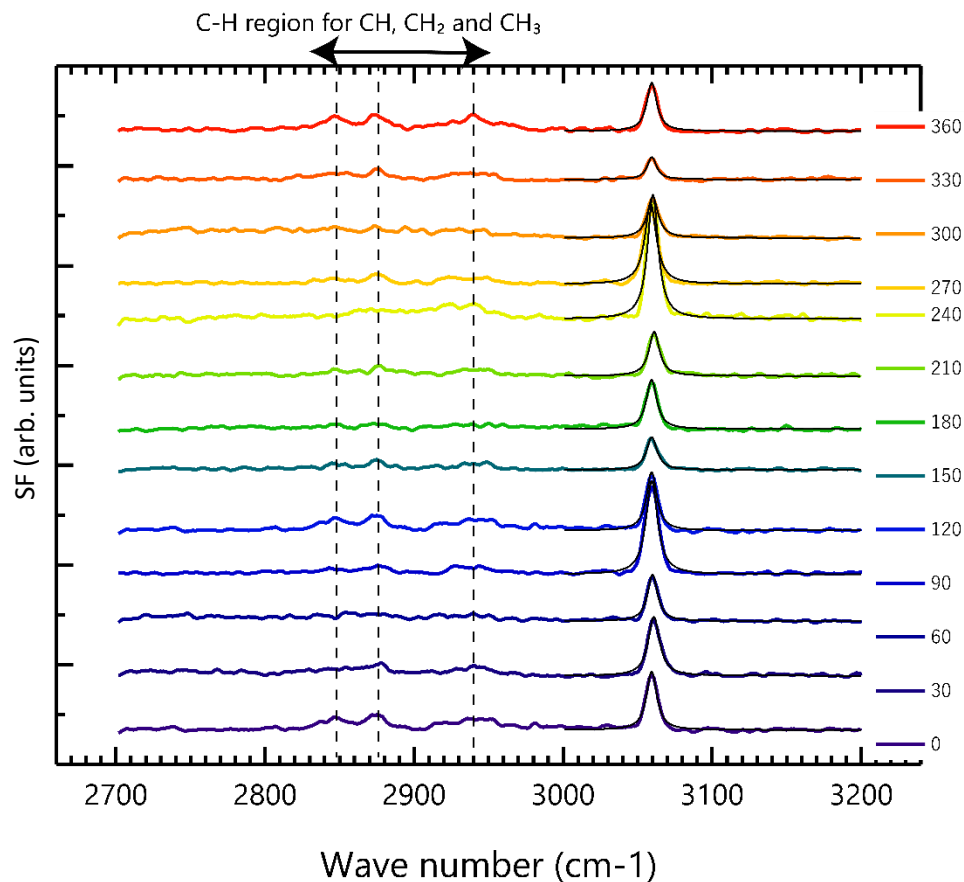
Figure 33: Rubrene SFG for SSP polarization combination. Each one of these spectra was collected at different azimuthal angle in the laboratory frame. The corresponding azimuthal angle is given on the right of each spectrum. The dashed lines represent the peaks found in C-H stretch region for CH, CH$_2$, and CH$_3$ groups.

5.4.3 Spectral Curve Fitting

The workflow of data analysis for spectral curve fitting of the SF spectra is shown in Figure 34. This procedure was applied to both PPP and SSP spectral sets individually. Each spectrum consisted of five scans, which were averaged and then smoothed with a 5 cm^{-1} moving average because the frequency resolution of the mid-IR produced by the OPG/OPA is $\geq 5 \text{ cm}^{-1}$. Afterwards, for each polarization combination (PPP or SSP), the spectra were normalized from zero to one by selecting a global minimum and a maximum in that set.

59
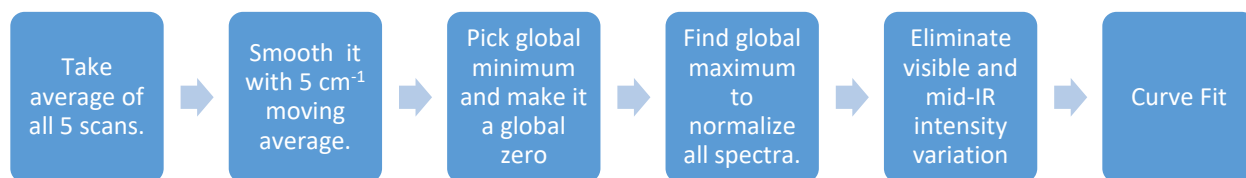
Figure 34: Data preparation procedure for spectral curve fitting of PPP and SSP SFG on rubrene.

To eliminate any variation in the SF signal due to a change in the intensity of the mid-IR produced by the OPG/OPA, a gold spectrum was acquired and used as a reference because gold provides a nearly flat nonresonant SFG response in the mid-IR frequency-range used in this experiment. The averaged gold spectrum is shown in Figure 35.
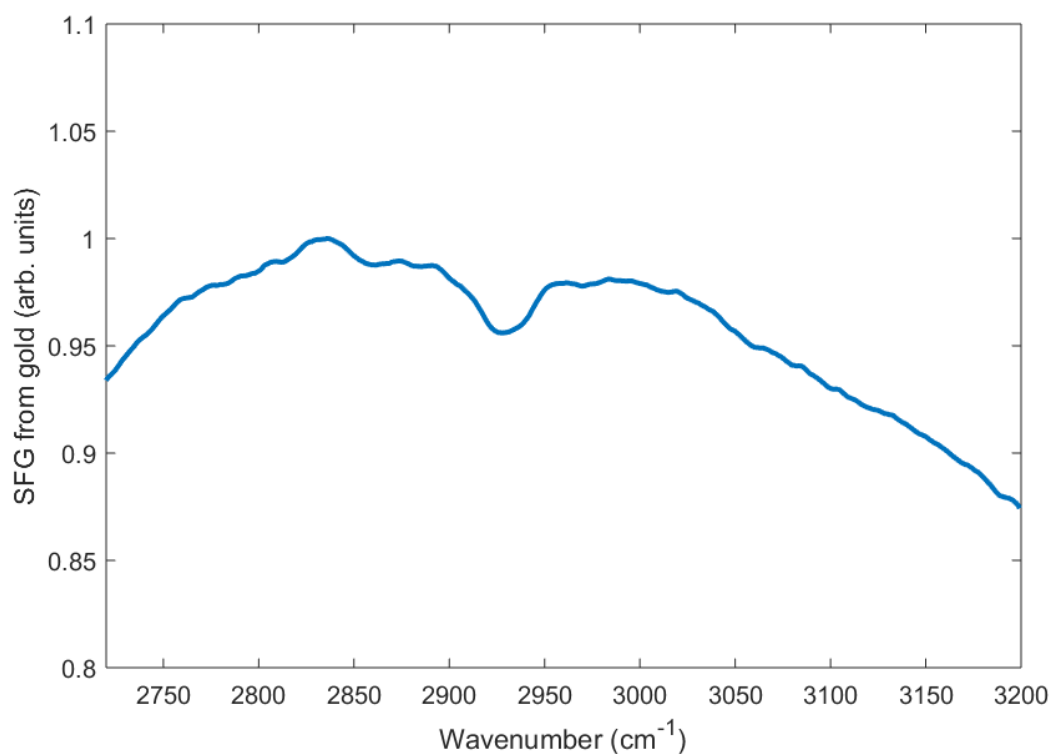
Figure 35: Gold SFG response collected in PPP polarization combination. The plot shows normalized gold SF signal with $25\ cm^{-1}$ smoothing to remove any artifacts from noise.

This spectrum has been normalized by the maximum value in its corresponding data set. Furthermore, a $25\ \mathrm{cm}^{-1}$ moving average has been applied to remove any artifacts from noise

60

because the goal here is to extract the slow variations in the mid-IR intensity from the OPG/OPA. Variations in this spectrum are an indicator of changing mid-IR intensity across the scan. Using this gold spectrum as an indicator of the mid-IR intensity profile, the rubrene spectra were normalized to remove any mid-IR intensity dependence. Furthermore, as the polarization combination is changed, the visible and the SF beams exhibit intensity variation due to tilted optics in their path. Before reaching the sample, the visible beam encounters two silver mirrors oriented at 45° and a CaF$_2$ window. The mirrors reflect 95.4 % of light for p polarization and 97.7% of light for s polarization. The CaF$_2$ window transmits 99.6% visible light for p polarization and 82.0% for s polarization. On the other hand, for the SF emitted from the sample, the CaF$_2$ window shows 99.9 % transmission for p polarization and 80.15 % transmission for the s-polarization. The intensity variations in the SF signal introduced by the combination of these factors were accounted for by adjusting the relative intensities of the PPP and SSP spectra. Finally, the rubrene spectra were used for spectral curve fitting.

The spectral curve fitting was performed with following equation that considers contributions from both resonant and nonresonant SF signals. The resonant term contains only a single resonant vibrational mode.

$$I_{SF}(\omega_{IR}) = \left| A e^{-\left(\frac{(\omega_{IR}-\mu)^2}{\sigma^2}\right)} e^{i\phi} + \frac{B}{\omega_{IR} - \omega_{res} + i\Gamma} \right|^2$$

In this equation the nonresonant and resonant amplitudes are represented by A and B, respectively; ω_{res} represents the resonance frequency, ω_{IR} is the frequency of the mid-IR, and Γ is the mode damping rate. The nonresonant signal follows a Gaussian profile centered at μ with standard deviation σ. The resonant signal is fit to a Lorentzian profile (typical of a lifetime spectral

broadening). The relative phase between the resonant and nonresonant background is captured by ϕ. A curve-fitting example is shown in Figure 36.
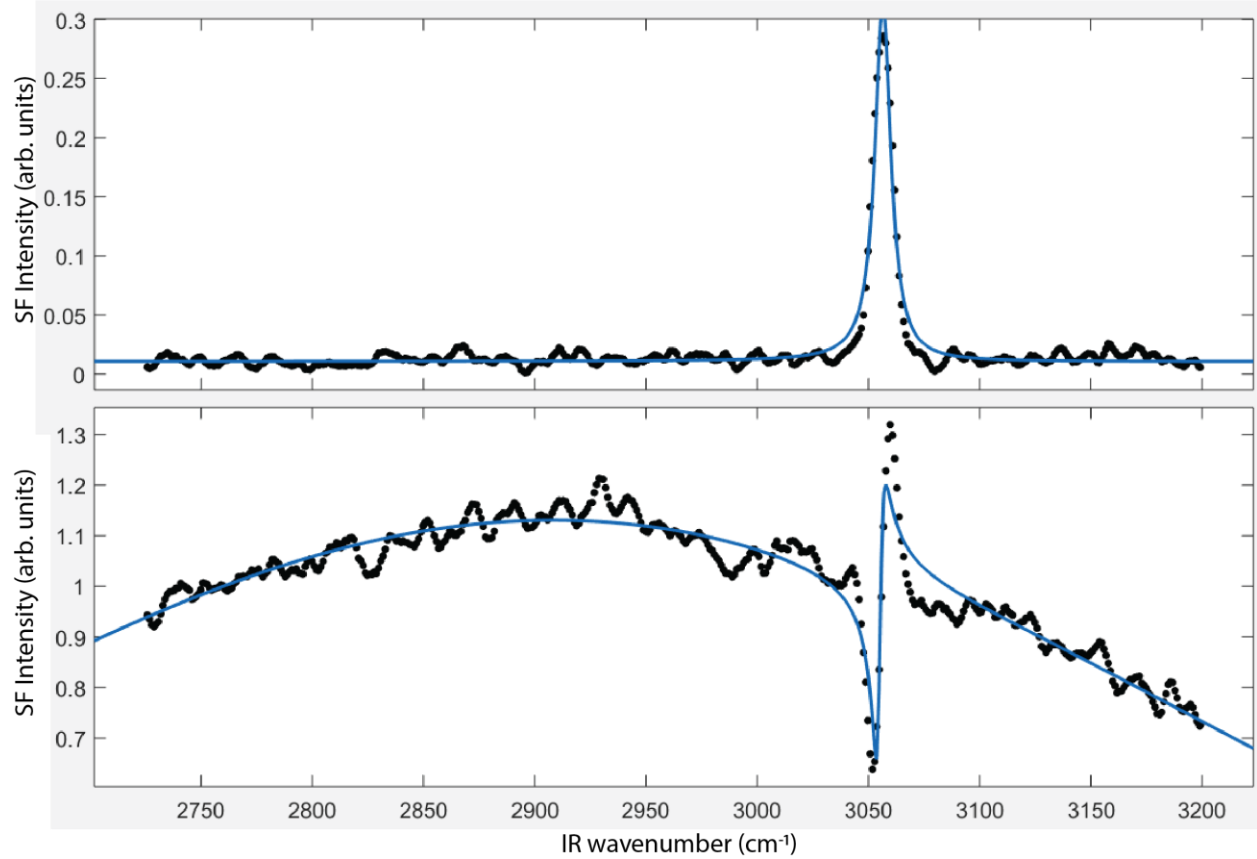
Figure 36: Spectral fitting (blue curve) along with the experimental data points (black dots) for rubrene spectra. The two example spectra shown here were obtained at different azimuthal angles with the PPP polarization combination.

The spectral fitting results for PPP are shown in Figure 37. The figure contains polar plots of individual curve fitting parameters. In these plots, the azimuthal angle of crystal in lab frame and the magnitude of fitting parameter are plotted as angle and radius, respectively. The resonant amplitude, nonresonant amplitude, phase, and damping rate for the SF response, all show a 2-fold symmetry.
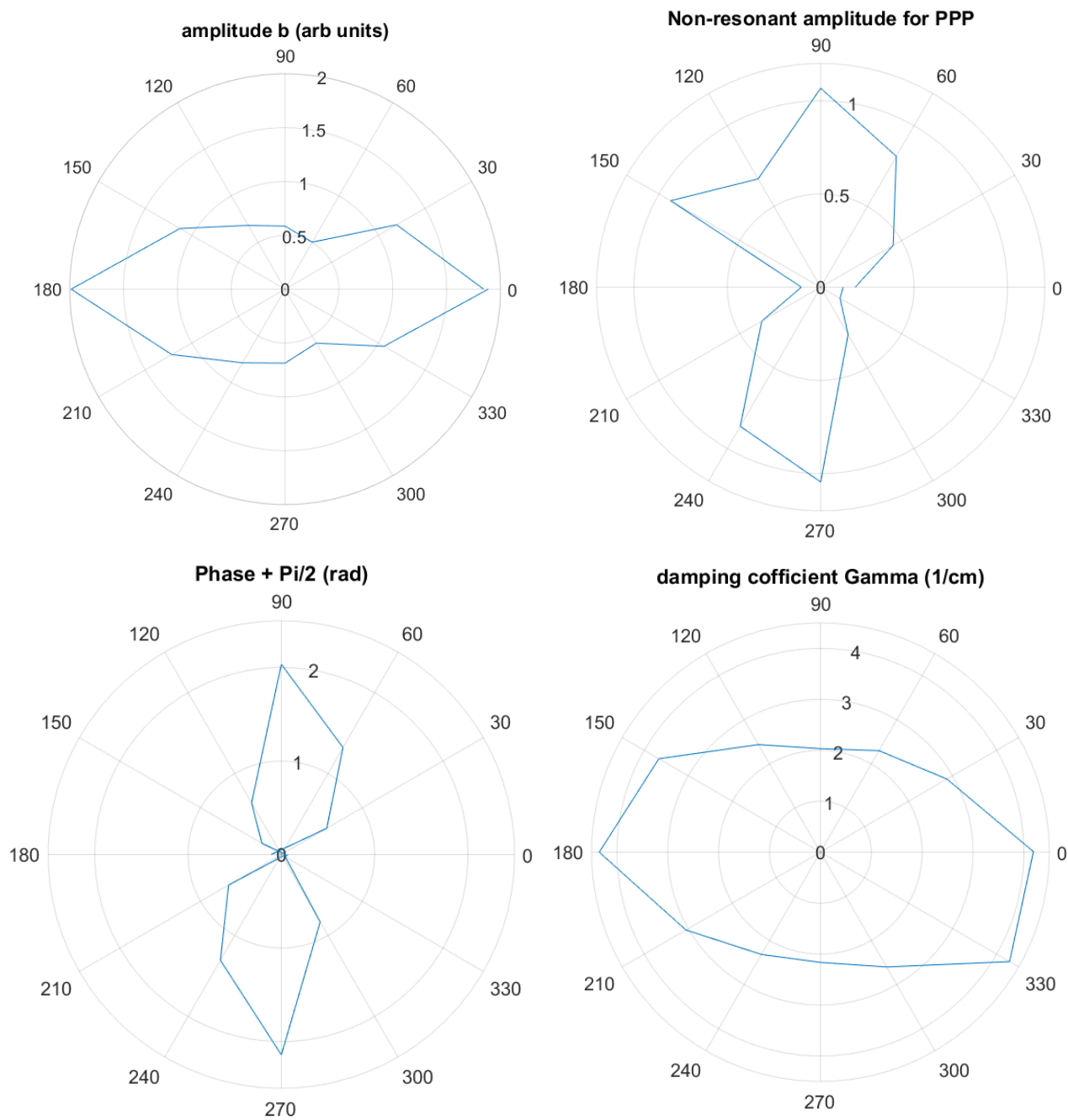
Figure 37: Spectral curve fitting results for PPP SFG spectra plotted on polar plots with radial distance from the center representing magnitude. All components i.e., resonance amplitude, nonresonant amplitude, damping, and relative phase show anisotropy. The damping displays only slight variation; however, the other components show large change in magnitude.
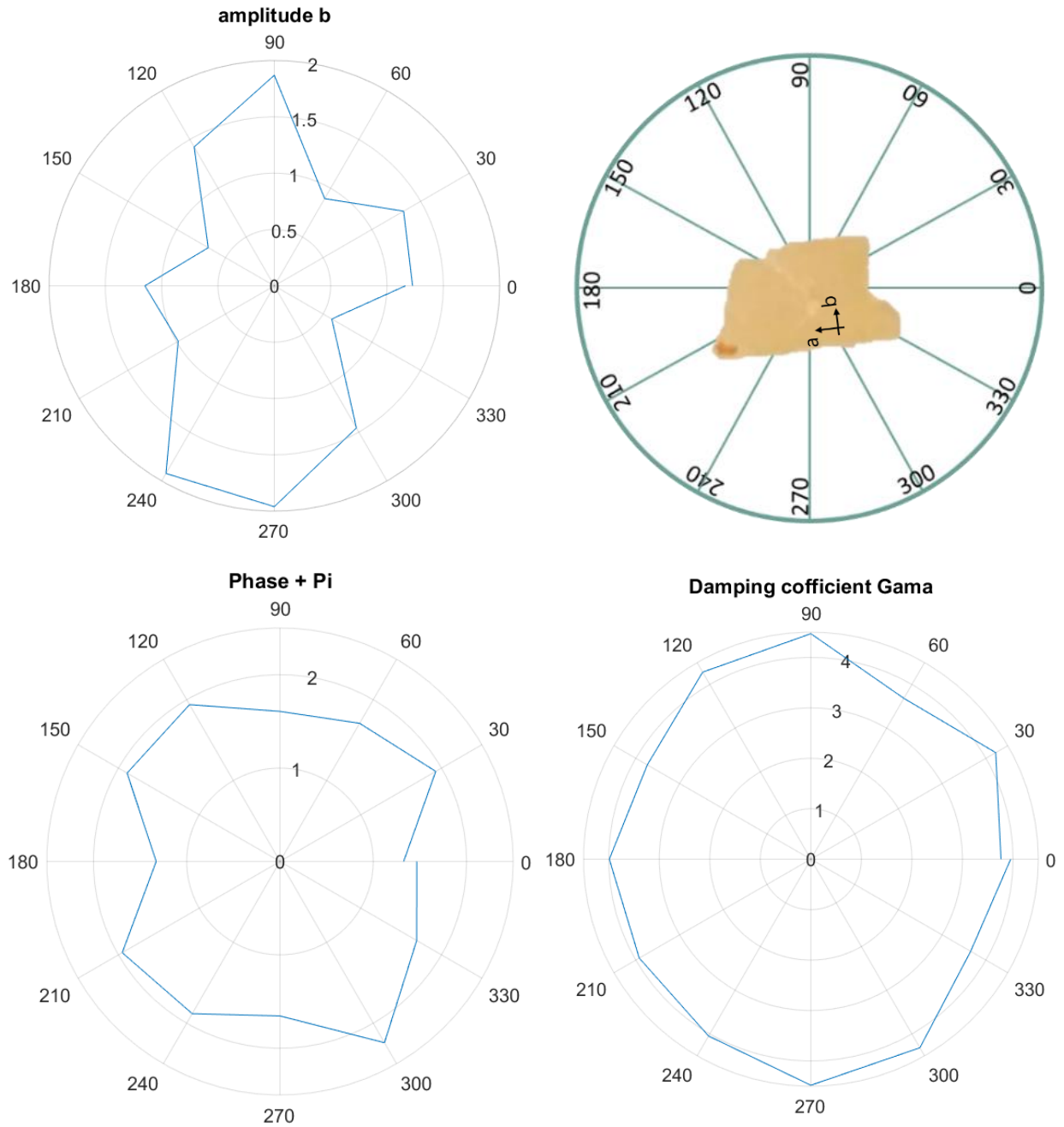
Figure 38: Spectral fitting results for SSP spectra containing polar plots of the resonance amplitude, phase, and damping coefficient. Furthermore, the actual sample is also shown for reference.

The results of SSP curve fitting are shown in Figure 38. The figure only shows the polar plots associated with resonant amplitude, relative phase of nonresonant signal, and damping rate

because the appreciable nonresonant signal was absent from the SSP spectra. Both resonant amplitude and phase for the SF response, display a pseudo 4-fold symmetry; however, the damping rate stays relatively unchanged.

The comparison between resonance amplitudes for PPP and SSP polarization combinations is shown in Figure 39. The red bars represent 95% confidence interval. The two amplitudes not only maximize at different azimuthal orientations but also show different shapes.
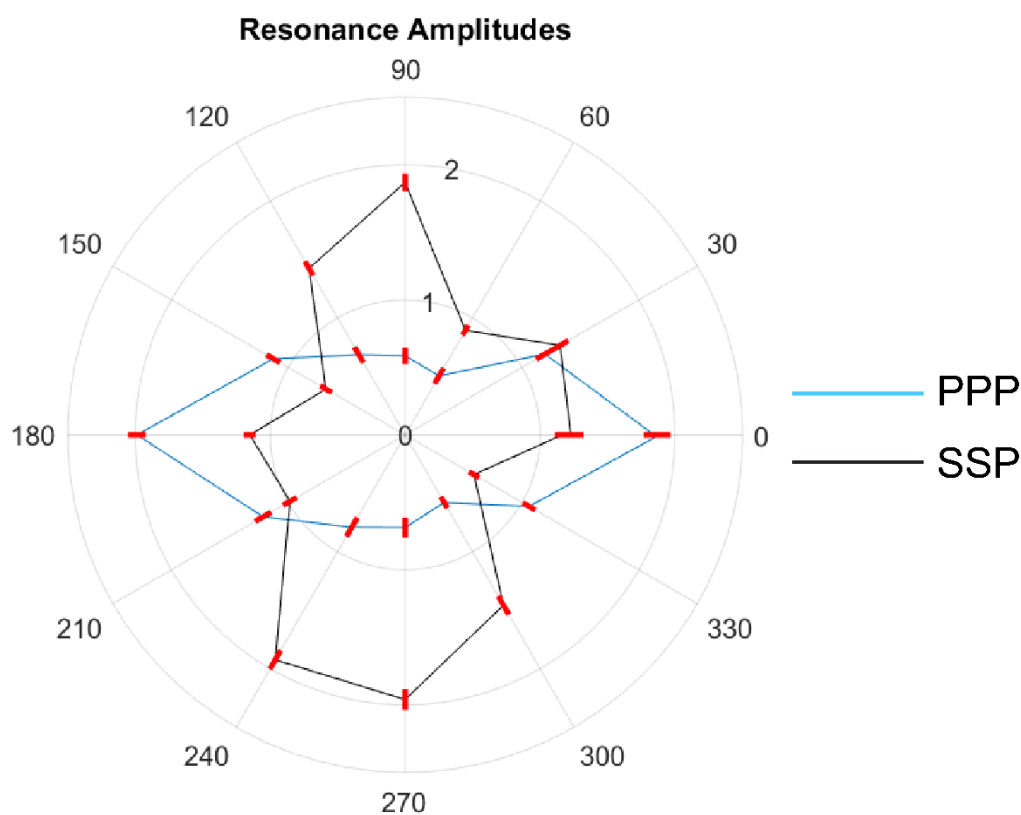
Figure 39: Comparison between the resonance response amplitude from PPP and SSP polarization combinations with red bars indicating 95% confidence interval. The maxima for the two amplitudes are azimuthally shifted by 90°.

A particular value of importance is the resonance amplitude ratio between the PPP and SSP polarization combinations as it can be utilized to extract the orientation of the functional groups responsible for the resonance response. The polarization ratio is shown in Figure 40.
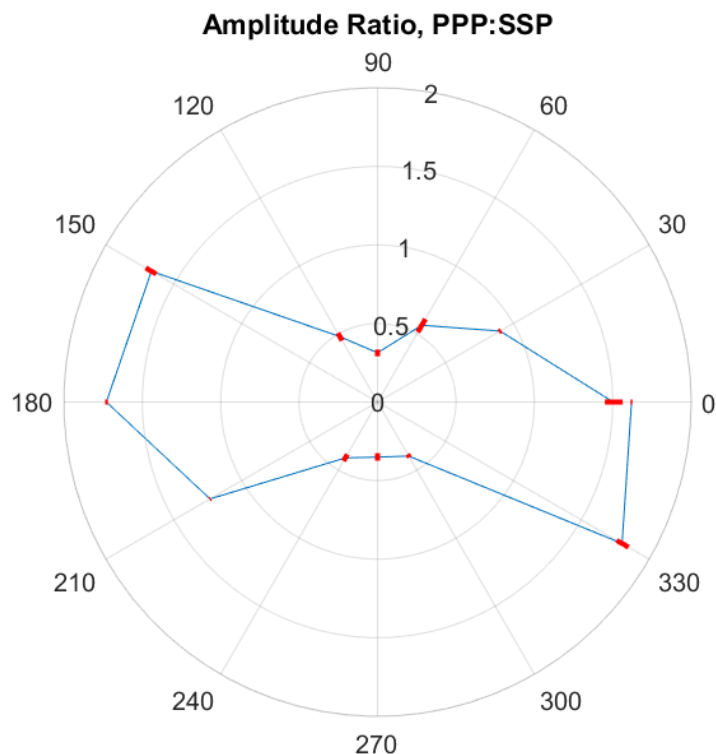
Figure 40: Resonance response amplitude ratio between the PPP and SSP polarization combinations. For every data point, the red bars represent the intervals obtained by taking the ratio between its maximum and minimum values within 95% confidence interval.

5.5 Orientation Analysis

The resonance peak at 3058 cm^{-1}, seen in both PPP and SSP spectra, is in C-H stretch range of the phenyl rings; therefore, it is assigned to the C-H symmetric stretch mode v_2 of the phenyl rings [157, 158]. The phenyl rings responsible for this resonant SFG response must be on the surface of the single-crystals as the ones in the bulk of the crystal experience a centrosymmetric environment.

Since the rubrene surface is in crystal ab-plane, the two phenyl rings attached to the upper-side of each surface molecule are projected outwards. The orientation of these phenyl rings, particularly the tilt from the surface normal, can be obtained from the SFG response [43, 157, 158]. Figure 41

shows the orientation relation from the molecular frame to the crystal frame and then from the crystal frame to the laboratory frame.
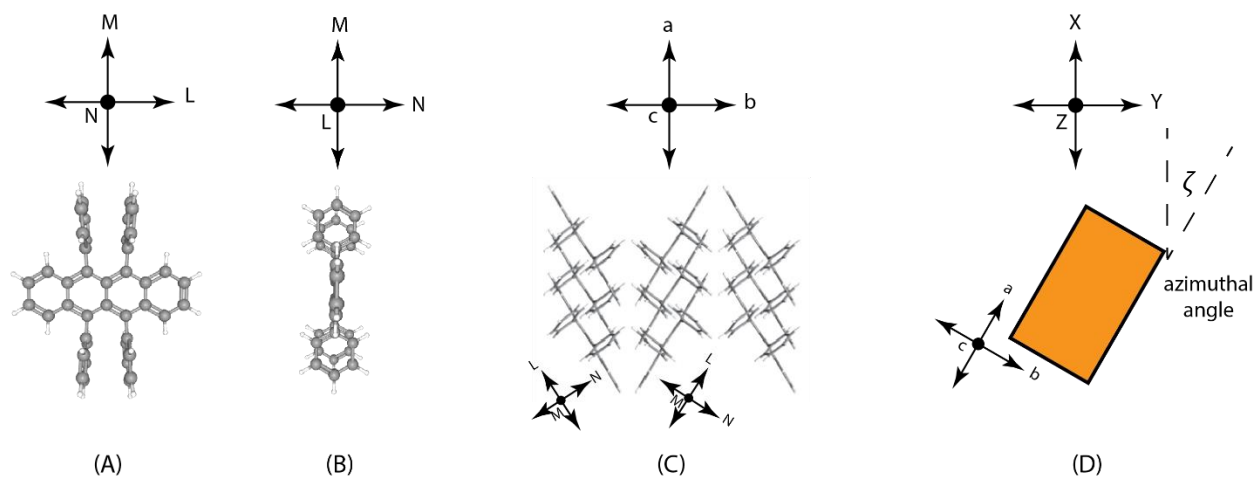
Figure 41: The orientation relation between the molecular, crystal, and laboratory frames. (A) and (B) represent the molecular structure from two different viewing angles. (C) shows the molecular orientation on the crystal's surface in ab crystal plane. Finally, (D) represents the orientation relation between crystal abc-axis and laboratory xyz-axis. If the azimuthal angle is zero degrees, the a- and b-axis align with laboratory x- and y-axis. The tilted representation emphasizes azimuthal rotation ζ.

From Figure 41 (A) and (B) it can be seen that the phenyl ring planes are tilted ∼90° with respect to the tetracene backbone plane. Therefore, the phenyl rings are approximately in the molecular MN-plane with normal directed along molecular L-axis. According to Figure 41 (C), there are two types of orientations for the molecules on the crystal surface; one with molecular L-axis rotated clockwise and the other with anticlockwise from the crystalline a-axis. The molecular M-axis and the crystal c-axis are parallel. Finally, in Figure 41 (D) it is observed that the crystal frame can be easily related to the laboratory frame through a simple azimuthal rotation about the laboratory z- or crystalline c-axis.

The complete set of degrees of freedom for the phenyl rings on the surface of the single-crystal are shown in Figure 42. For determining the orientation, SFG response is simulated and orientation parameters are tuned to fit the simulation to the experiment results.
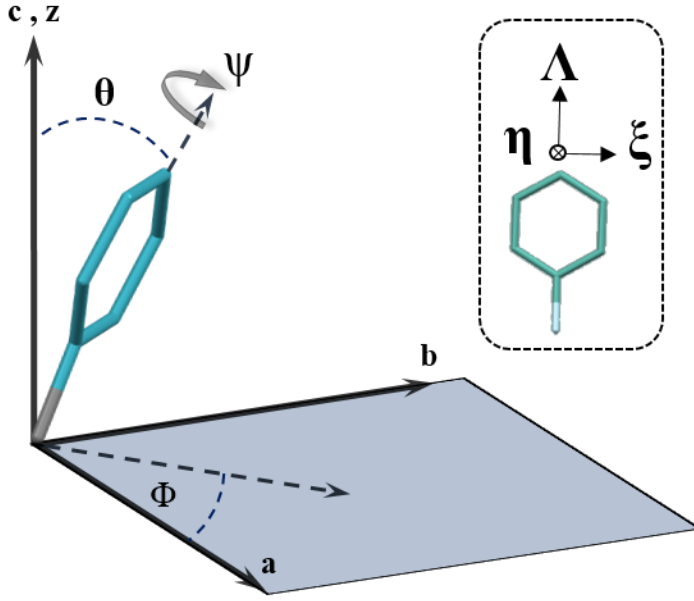
Figure 42: Angular degrees-of-freedom for a phenyl ring on the rubrene single-crystal's surface. The a, b, and c are the crystal axis. Their relation to the laboratory and the molecular axis is explained in the previous figure. Λ, η, and ξ are the native axis for the phenyl ring.

The SF signal can be described by

$$I(\omega_{sf}) = \frac{8\,\pi^3\omega_{sf}^2\sec(\Omega_{sf})^2}{c^3 n_1(\omega_{SF})n_1(\omega_{vis})n_1(\omega_{IR})}|\chi_{eff}^{(2)}|^2 I(\omega_{vis})I(\omega_{IR})$$

where $\chi_{eff}^{(2)}$ represents effective nonlinear susceptibility, c is the speed of light, Ω_{sf} is the SF emission angle from the rubrene surface, n_1 is the refractive index of air, and ω's represent the frequencies for SF, visble, and IR beams [42, 43, 159]. The effective susceptibility is given by

$$\chi_{eff}^{(2)} = [\hat{e}(\omega_{sf}).L(\omega_{sf})].\chi_{ijk}^{(2)}:[L(\omega_{vis}).\hat{e}(\omega_{vis})][L(\omega_{ir}).\hat{e}(\omega_{ir})]$$

where $\hat{e}$'s are the electric field polarization vectors, L's are Fresnel factors, and $\chi_{ijk}^{(2)}$ is the macroscopic nonlinear susceptibility with $(i,j,k) \in (x,y,z)$. The effective susceptibilities for the SSP and PPP polarization combinations take the following forms [43]:

$$\chi_{eff, \ ssp}^{(2)} = L_{yy}(\omega_{sf})L_{yy}(\omega_{vis})L_{zz}(\omega_{ir})\sin(\Omega_{ir})\chi_{yyz}^{(2)}$$

$$\chi_{eff, \ ppp}^{(2)} = -L_{xx}(\omega_{sf})L_{xx}(\omega_{vis})L_{zz}(\omega_{ir})\cos(\Omega_{sf})\cos(\Omega_{vis})\sin(\Omega_{ir})\chi_{xxz}^{(2)}$$
$$-L_{xx}(\omega_{sf})L_{zz}(\omega_{vis})L_{xx}(\omega_{ir})\cos(\Omega_{sf})\sin(\Omega_{vis})\cos(\Omega_{ir})\chi_{xzx}^{(2)}$$
$$+L_{zz}(\omega_{sf})L_{xx}(\omega_{vis})L_{zz}(\omega_{ir})\sin(\Omega_{sf})\cos(\Omega_{vis})\cos(\Omega_{ir})\chi_{zxx}^{(2)}$$
$$+L_{zz}(\omega_{sf})L_{zz}(\omega_{vis})L_{zz}(\omega_{ir})\sin(\Omega_{sf})\sin(\Omega_{vis})\sin(\Omega_{ir})\chi_{zzz}^{(2)}$$

In these equations, Ω_i represents the emission angle for the SF, and incidence angle for the visible and IR beams. The Fresnel factors are given by:

$$L_{xx}(\omega_i) = \frac{2n_1(\omega_i)\cos(\gamma_i)}{n_1(\omega_i)\cos(\gamma_i) + n_2(\omega_i)\cos(\Omega_i)}$$

$$L_{yy}(\omega_i) = \frac{2n_1(\omega_i)\cos(\Omega_i)}{n_1(\omega_i)\cos(\Omega_i) + n_2(\omega_i)\cos(\gamma_i)}$$

$$L_{zz}(\omega_i) = \frac{2n_2(\omega_i)\cos(\Omega_i)}{n_1(\omega_i)\cos(\gamma_i) + n_2(\omega_i)\cos(\Omega_i)}\left(\frac{n_1(\omega_i)}{n'(\omega_i)}\right)^2.$$

Here, $i \in (sf, vis, ir)$; therefore, ω_i can be frequency for SF, visible or IR beam. The refractive indices for the rubrene bulk and the rubrene surface are represented by n_2 and n', respectively. At any given azimuthal angle ζ (see Figure 41 D), the refractive index n_2 is calculated by taking Euclidian sum of the refractive indices along crystalline a- and b-axis, i.e., $n_2 = \sqrt{(n_a\cos(\zeta))^2 + (n_b\sin(\zeta))^2}$ and $n' = \frac{n_1+n_2}{2}$.

The macroscopic susceptibilities can be related to the molecular hyperpolarizability, which in turn can be expressed as a function of IR transition dipole and Raman polarizability as expressed in Eq. 6 through Eq. 8 in chapter 1.

For v_2 vibrational mode, the nonzero hyperpolarizability terms are $\beta_{\xi\xi\Lambda}$, $\beta_{\eta\eta\Lambda}$, and $\beta_{\Lambda\Lambda\Lambda}$ [157-160]. Furthermore, from Raman depolarization ratios, $\beta_{\Lambda\Lambda\Lambda} \cong 0.69\beta_{\xi\xi\Lambda}$ and $\beta_{\eta\eta\Lambda} \cong 0$ [157, 158]. Using these values with Eq. 6 from chapter 1 gives

$$\chi_{ijk}^{(2)} = N_s \langle R_{ijk,\xi\xi\Lambda}(\theta,\psi,\phi)\rangle\beta_{\xi\xi\Lambda} + N_s\langle R_{ijk,\Lambda\Lambda\Lambda}(\theta,\psi,\phi)\rangle\,\beta_{\Lambda\Lambda\Lambda}.$$

In this equation, $\langle\rangle$ represent the average over entire surface population of the phenyl rings. $R_{ijk,\eta\eta\Lambda}(\theta,\psi,\phi)$ are trigonometric functions obtained from Euler transformations connecting $\beta_{\eta\eta\Lambda}$ and $\chi_{ijk}^{(2)}$. Similarly, $R_{ijk,\Lambda\Lambda\Lambda}(\theta,\psi,\phi)$ connect $\beta_{\Lambda\Lambda\Lambda}$ with macroscopic susceptibility [160]. Both of them are functions of phenyl ring orientation. Their detailed expression are given in appendix.

To determine the exact orientation of the phenyl rings (θ,ψ, and ϕ), curve fitting was carried out in Mathematica, in which experimental SFG response for the PPP and SSP polarizations was compared to the simulated one. The orientation distributions for θ,ψ, and ϕ in the phenyl ring populations were modelled by delta functions. Due to the herringbone arrangement of the surface molecules, two types of phenyl groups were considered in the surface population, one with ϕ clockwise and the other with ϕ anticlockwise from the crystalline a-axis.

To understand the azimuthal dependence of different components in the effective susceptibility, Figure 43 shows a plot of the Fresnel factors, macroscopic susceptibility, and effective susceptibility. For these simulations, the initial magnitude of ϕ was estimated by the UV-vis results presented earlier to be $\sim38°$. On the other hand θ and ψ were given initial values of $\sim0°$.
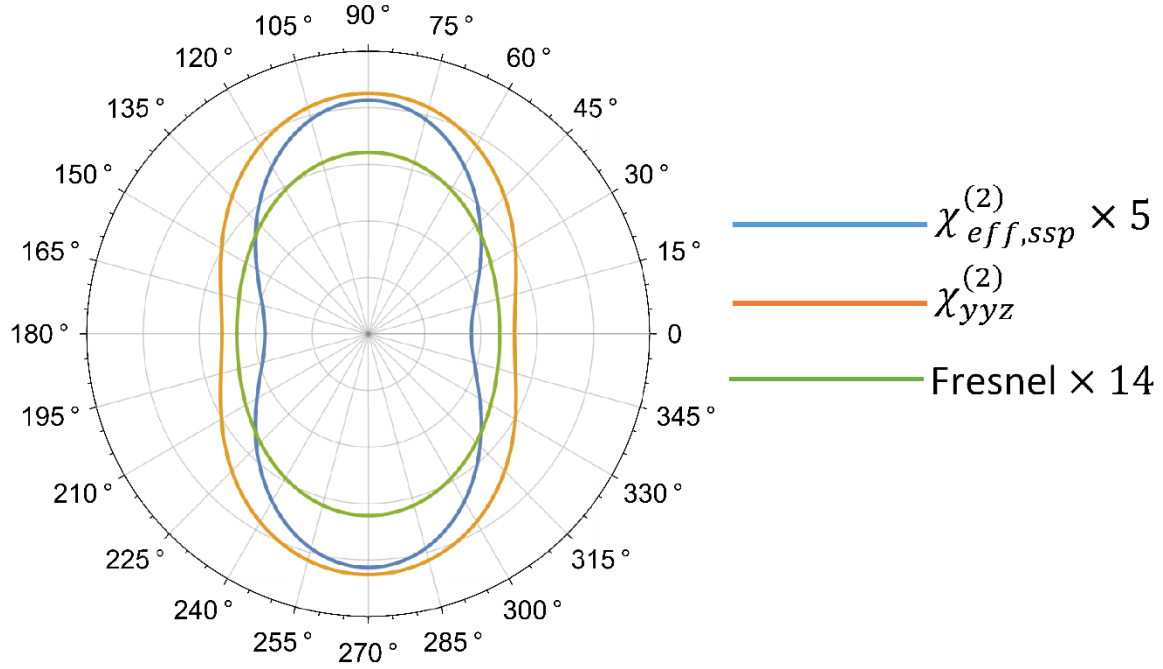
Figure 43: Azimuthal variation in the effective susceptibility, macroscopic susceptibility, and Fresnel factors for the SSP polarization combination. For this simulation $\theta = 0°, \psi = 0°$, and $\phi = 38°$.

Both susceptibilities and Fresnel factors show anisotropy; however, the azimuthal distribution of Fresnel factors is independent of θ, ψ, and ϕ. Different choices of these parameters change the profiles of effective susceptibility and macroscopic susceptibility.

The azimuthal behaviors of $\chi^{(2)}_{eff,ppp}$ and $\chi^{(2)}_{eff,ssp}$ simulations are presented in Figure 44. The azimuthal orientation of maxima for both quantities matches with the experimentally obtained results. Upon changing θ and ϕ, the shapes of the two curves change but their orientation stays the same; however, changing ψ, changes their orientations.
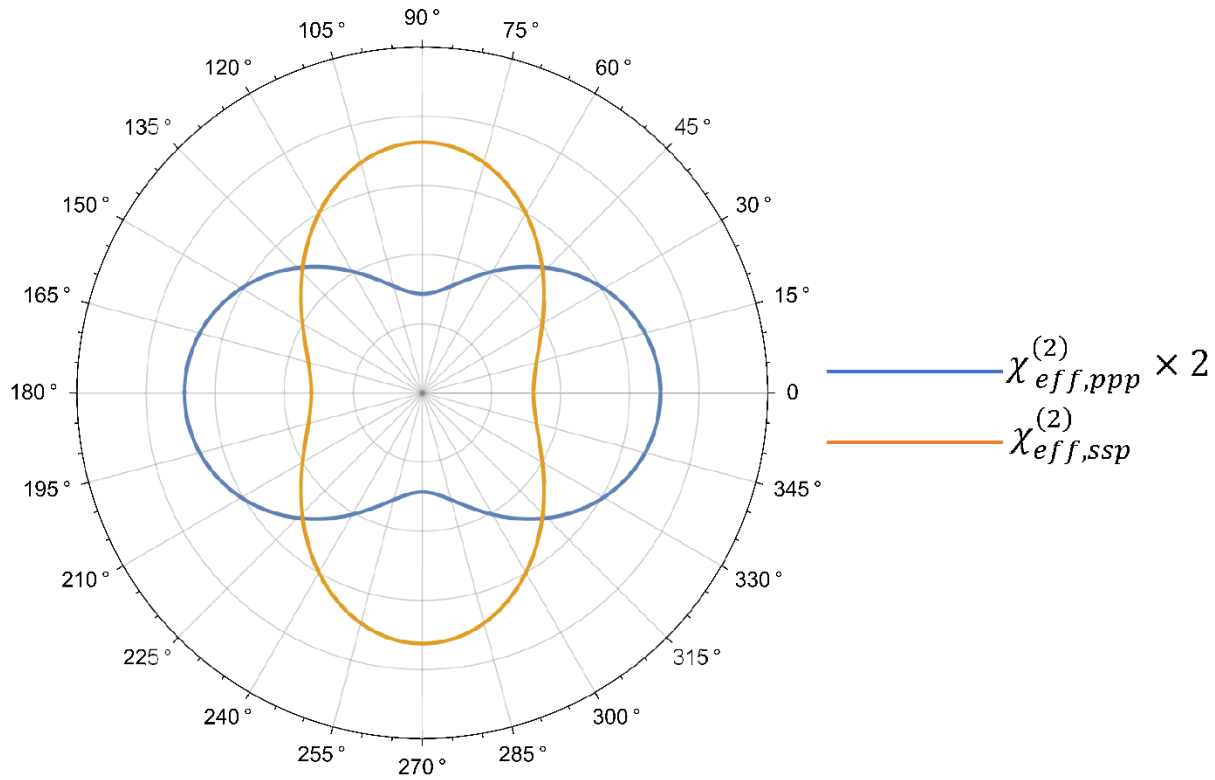
Figure 44: Azimuthal variation in PPP and SSP effective susceptibilities. For this simulation $\theta = 0°, \psi = 0°$, and $\phi = 38°$.

Finally, to calculate the orientation for the surface phenyl groups, the experimentally obtained SFG amplitude ratio between PPP and SSP polarization combinations is curve-fitted with theoretically calculated ratio. The results are presented in Figure 45 and summarized in Table 3. The three panels in Figure 45 show the progression of the curve fitting, highlighting the effect of each parameter individually.

72
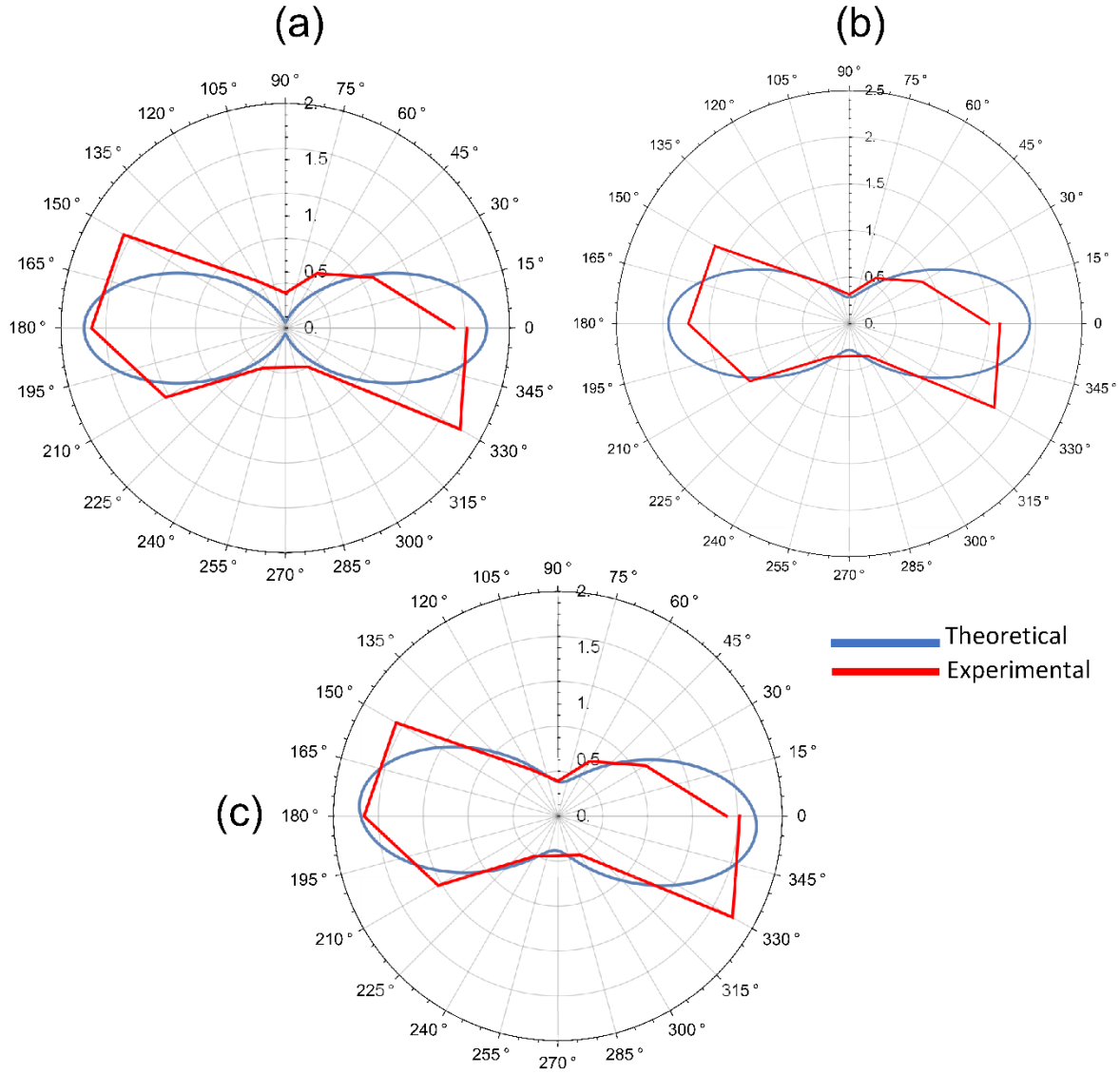
Figure 45: Fitting between simulated and experimental SFG amplitude ratios between PPP and SSP polarization combinations. Plots (a), (b), and (c) show the progression of the fitting process with final fit achieved in plot (c). In plot (a) $\theta = 0°, \psi = 0°$, and $\phi = 32°$. In plot (b) $\theta = 45°, \psi = 0°$, and $\phi = 32°$. Finally, in plot (c) $\theta = 45°, \psi = 7°$, and $\phi = 32°$.

Parameter	Value	Standard Error
θ	45°	13°
ψ	12°	12°
ϕ	33°	3°

The variation of simulated ratios using the full range of parameters presented in Table 3 is shown in Figure 46. The default values of the parameters are $\theta = 45°$, $\psi = 12°$, and $\phi = 33°$. The figure contains three sets of curves, each presenting the variation of one parameter. For every parameter, the corresponding set contains three curves, one at the lower bound, one at the median, and one at the upper bound of the parameter. Panel (a) indicates that the variation in θ changes the elongation and central dip of the ratio curves. In panel (b), the variation of ψ introduces elongation variation was well as rotation of the curves. Finally, in panel (c), different values of ϕ induce elongation and squeezing of the ratio curves.
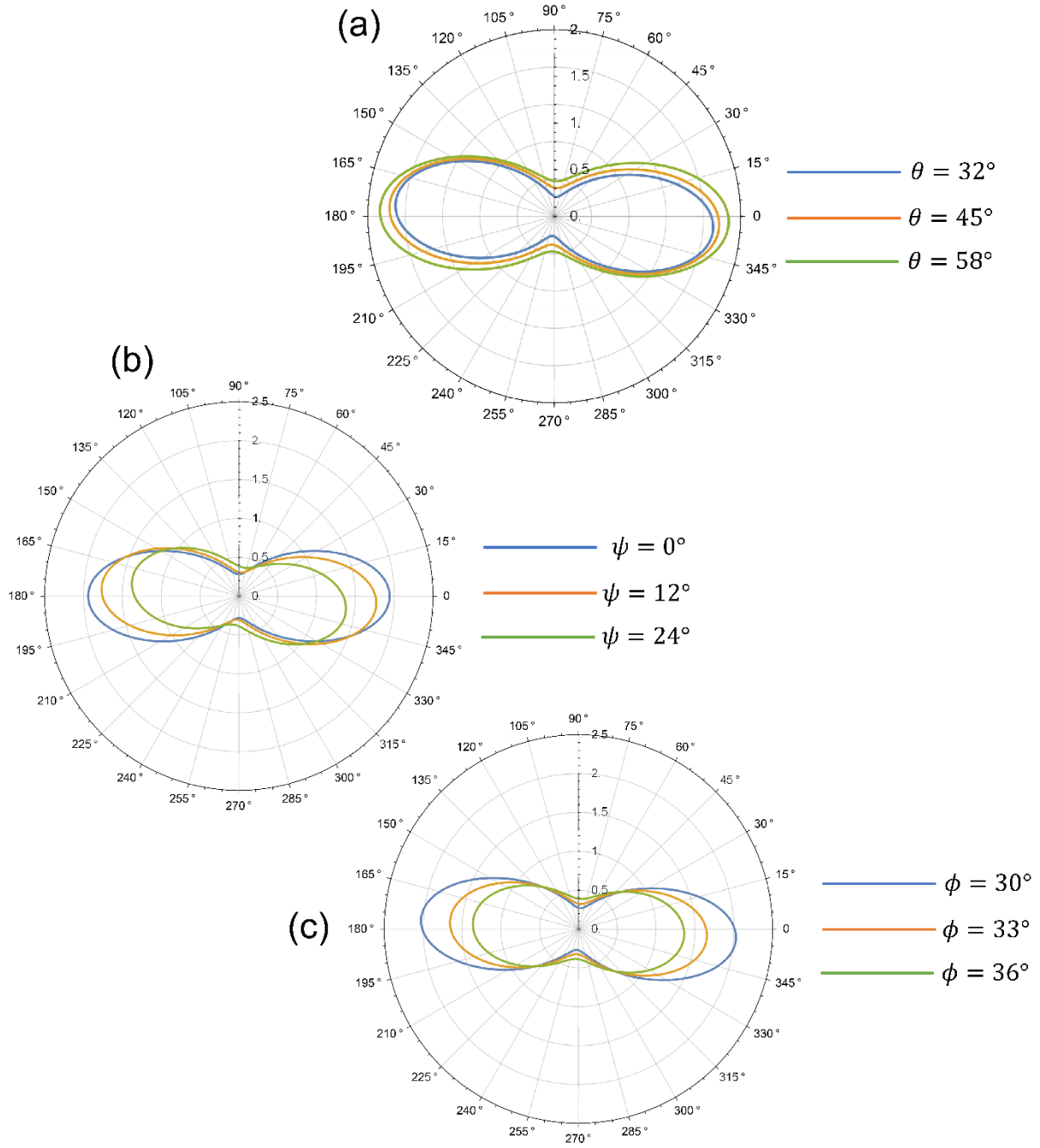
Figure 46: Variation in the simulated polarization ratio by changing the orientation parameters individually across the range of the curve fitted results. The default values are $\theta = 45°, \psi = 12°$, and $\phi = 33°$. In each panel, only one parameter is changed while the other two are kept at their default values. (a) represents the variation in θ, (b) shows curves for different values of ψ, and (c) shows variation in ϕ.

5.6 Discussion

The nonresonant signal, observed only in PPP polarization combination, followed a Gaussian profile centered around 2600 cm^{-1} to 2700 cm^{-1}. Its amplitude displayed a two-fold symmetry with largest magnitude at 90° and 270°. These azimuthal angles correspond to orientations in which crystalline b-axis is in the plane of incidence for the SFG setup. Furthermore, since the nonresonant signal was not observed in SSP combination, it indicates that this signal requires an electric field component of the visible or SF light along the crystalline c-axis i.e., normal to surface (a condition not fulfilled by SSP).

This signal is possibly from electronically resonant SFG response from the rubrene single-crystal. Figure 47 shows two possible energy level pathways for such SFG process. In (A), the visible beam at 532 nm is resonant with the electronic or exitonic transition, and in (B) the SF beam at 466.2 nm is resonant with a transition between two stationary electronic levels. From the fitting performed on vibronically nonresonant SF signal, the mid-IR for this component is centered at 2650 cm^{-1}.
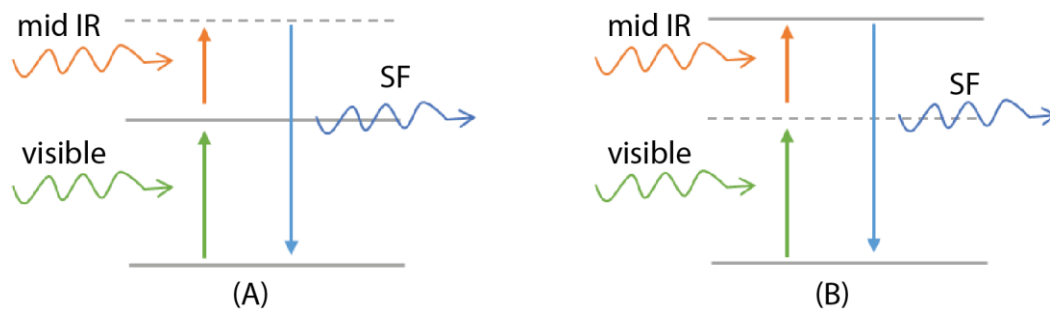
Figure 47: Two different energy pathways for electronically resonant SFG from rubrene single-crystals. The solid energy levels represent stationary electronic states.

For visible beam, the 532 nm wavelength corresponds to 2.33 eV energy. This energy is very close to a 2.35 eV excitonic transition observed in oblique incidence in the bc-plane of rubrene single-crystal using p-polarized light by Tavazzi et. al., [148]. Their results are shown in Figure 48. They attributed it to c-polarized transition in the crystal under weak intermolecular interactions. They also assigned its molecular origins to molecular M-axis. Since this transition depends on an intermolecular interaction, the azimuthal anisotropy of that interaction can lead to a rotational anisotropy of nonresonant response as well. Coincidently, an anisotropic azimuthal response was observed in the vibronically nonresonant SFG for PPP polarization combination. This vibronically nonresonant SFG showed largest amplitude along crystalline b-axis with a 2-fold symmetry as shown in Figure 37. On the other hand, it is possible that the intermolecular interaction that causes azimuthally anisotropic behavior for vibronically nonresonant SFG is also connect to the intermolecular π-stacking which results in characteristic high charge mobility along crystalline b-axis.
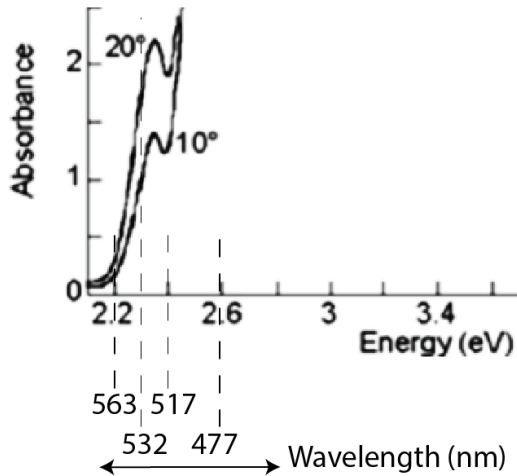
Figure 48: Absorption bands form the excitonic transitions observed in a single-crystal rubrene at an oblique incidence of 20° *and* 10° *in the bc crystal plane. Image adapted from publication by Tavazzi et. al., [148].*

The SF beam, with mid-IR centered in the $2600\ \text{cm}^{-1}$ to $2700\ \text{cm}^{-1}$ range, is produced at ~465.2 nm. This wavelength corresponds to 2.659 eV energy that is close to absorption peak observed at 2.67 eV in normal incidence geometry with both a and b polarized light i.e., transitions a3 and b3 in Figure 29. Its molecular transition dipole origins are in molecular LN-plane [147, 148].

The transition dipole for 2.67 eV absorption is predominantly along molecular L-axis, which lies in ab crystal plane i.e., the crystal surface plane. To access this transition, the incident light has to have electric field components along crystal surface plane. Any p-polarized light has electric field components both parallel and perpendicular to the surface. However, s-polarized light is completely along the surface. If this transition were involved in producing vibronicaly nonresonant SF signal as suggested by Figure 47 (B), the nonresonant signal would have been present in SSP as well. However, the SSP combination does not show nonresonant SF signal. Therefore, one can conclude that the nonresonant SFG signal (observed only in PPP polarization combination) is originating from the energy level description (A) of Figure 47. It must be noted that for this system only PPP and SSP polarization combinations generate considerable SF signal.

The orientation results achieved from the SFG exhibit large margins of error for both θ and ψ. However, the results for ϕ had relatively high accuracy. The value of ϕ is in agreement with theoretically calculated values in literature but it is slightly different from the one calculated using UV-vis spectra [147]. A 45° θ indicates a considerable tilt from the surface normal despite the large standard error. Similarly, the extracted value of ψ indicates that the phenyl rings do not show large twists. A possible reason for these large margins of error is the delta distribution assumption for the orientation of the phenyl rings on the surface. Finally, these results indicate that the surface

phenyl rings exhibit an ordered-orientation which can lead to different steric and electrostatic interactions if the rubrene interface is in contact with other media such as ionic liquids.

5.7 Conclusion

Multiple techniques were utilized to complement each other in characterizing the rubrene single-crystal surface. Using both RHEED and UV-vis absorption, the molecular arrangement, crystal structure, and crystal orientation were confirmed. With the help of structural information, the molecular orientation (especially that of the surface phenyl rings) was determined with SFG. Furthermore, the vibronicaly nonresonant response indicated complicated pathways for the SFG process due to the visible and SF photon energies matching with prominent electronic transitions. However, to completely resolve its origin, a SFG experiment with tunable visible and tunable mid-IR can be utilized.

Chapter 6

Neural Networks for Chemical Image Analysis

6.1 Introduction

Spectroscopic imaging generates spatial maps of chemically meaningful spectra. In these maps or images, each spatial pixel contains a spectrum. The identification and characterization of chemical species on each pixel requires careful analysis of the associated spectrum (pixel spectrum). Over the past two decades, SFG spectroscopic imaging has been developed into a reliable technique for analyzing surface chemistry [44-46, 161-164]. The image contrast in SFG microscopy can be developed from multiple, chemically meaningful, processes that generate variations in SFG spectra such as molecular orientation, surface coverage, functional groups, oxidation, and substrate orientation [44-46, 163, 164]. Traditionally, the chemical information is extracted from the pixel spectra through spectral curve fitting. However, typical curve fitting requires good quality spectra with low noise.

The SFG process is typically quite weak. Consequently, the SF intensity produced by the chemical systems is very low. Furthermore, in most imaging applications, the SF intensity is distributed over a large detector area. Therefore, generating good-quality pixel spectra in SFG imaging requires long acquisition times [46, 163, 164]. However, this limits the utility of the SFG imaging only to those chemical systems, which are stable over long periods and exhibit slow physical or chemical dynamics. By reducing the acquisition time for the SFG imaging, the spectral quality degrades. Consequently, the chemically meaningful imaging contrast is compromised.

Furthermore, the variations in SFG spectra are dependent on a complex interplay between variety of different features such as chemical nature, orientation, packing, substrate, environment, and experimental geometry [41-43]. Often these dependencies are nonlinear in nature. Consequently, the complex sensitivity to a variety of features complicates the scientific interpretation of the SFG spectra. Therefore, the full utility of the SFG spectroscopic microscopy requires a sophisticated spectral fitting and interpretation; this limits the noise tolerance and margin of error for the curve fitting process. Typically, in SFG images with high spectral noise, the spectral quality required for the curve fitting is achieved by averaging multiple pixel spectra in a process called pixel binning. The binning process improves the spectral quality but reduces the spatial resolution of the image. Because of this tradeoff, the full spatial resolution of the SFG imaging process is not achieved.

Neural Networks (NNs) are a set of machine learning algorithms that are particularly useful in solving problems where accurate physical or mathematical models are difficult or impossible to make [165]. NNs are, simply put, a collection of connected computation units called perceptrons. After the invention of a mathematical model for biological neurons by McCulloch and Pitts in 1943, the first perceptron was introduced by Rosenblatt in 1958 [166, 167]. However, multiple mathematical, algorithmic, and technological advances were required before NNs could prove useful in any practical application. With new mathematical and technological developments, a fresh set of algorithms called Neural Networks and Deep Networks have recently gained popularity by solving highly complex problems in both scientific and industrial fields [168-172].

To solve problems, NNs need to be trained on large amounts of data [165]. This training also requires extensive computational resources. Historically these issues limited their utility. However, increasingly digitized methods of data collection have ensured the availability of high

volumes of digital data. Furthermore, advancements in computer technology has procured extensive computation resources for training NNs to very high degrees of accuracy. NNs have shown the ability to learn complex patterns in data without any starting information on the underlying rules. They have also displayed accurate prediction and identification ability. Consequently, these algorithms are being deployed in a variety of complex tasks such as face recognition [172], content recommendation (Amazon and Netflix) [173], stock exchange prediction, and object classification [174, 175].

A typical spectral curve fitting process utilizes a hand-written mathematical model that it then fits to the spectral data for extracting chemical information; however, NNs learn the relevant spectral features for identifying chemical qualities through training on examples. If an ample amount of training data is available, the NNs can be deployed to provide the chemical features for the SFG spectroscopic imaging. The absence of a starting physical or chemical model makes NNs ideal for performing the complex chemical identification on the SFG spectra, which are often non-linearly dependent on multiple factors. Interestingly SFG imaging generates spectroscopic images with a spectrum contained in each pixel, providing the required large amount of spectral data for training NNs to a high accuracy. For example, an 1064×1064 image contains 1132096 spectra, one in each pixel. These spectra are relatively independent since imaging provides a one-to-one mapping of the spatial points on the sample surface to the pixels in the camera. As a result, the NNs can learn the relevant parameters or features in spectra that generate the chemical contrast from examples and then provide the correct chemical label, orientation or other characteristic of new spectral data.

In this chapter, I have utilized the NNs for providing chemical contrast in the SFG spectroscopic imaging through variation in SFG-active groups on thiol Self Assembled Monolayers (SAMs). The NN is trained on example-spectra from SFG images of different SAMs. Afterwards, the NN is given previously unseen spectral data for identification. The predictions are then utilized to construct chemically accurate spatial maps. Finally, the performance of NN is gauged at different spectral noise levels and other parameters. The results demonstrate that NNs can successfully operate at high levels of spectral noise where spectral fitting cannot yield useable results without extensive averaging through pixel binning. Therefore, the NNs can generate a chemical map while preserving spatial resolution in situations where spectral fitting decreases image resolution by pixel binning.

6.2 Neural Network Basics

The basic unit of a neural network is a perceptron (shown in Figure 49). It receives multiple inputs and generates a single output. The inputs are used to calculate a weighted sum given by the following equation

$$y = \sum w_i x_i + b$$

In this equation, w_i is the weight for input x_i and b is a constant called 'bias'. The following relation then converts the weighted sum to an output

$$f(y) = \begin{cases} 0, & y < 0 \\ y, & y \geq 0 \end{cases}$$

This particular relation is called Rectified Linear function. Another popular choice for calculating the output is a sigmoid function i.e.,

$$f(y) = \frac{1}{1 + e^{-y}}$$

The weights, bias, and the choice of function for generating output is unique to every perceptron.

At this very basic level, a perceptron is only capable of handling simple linear analysis.
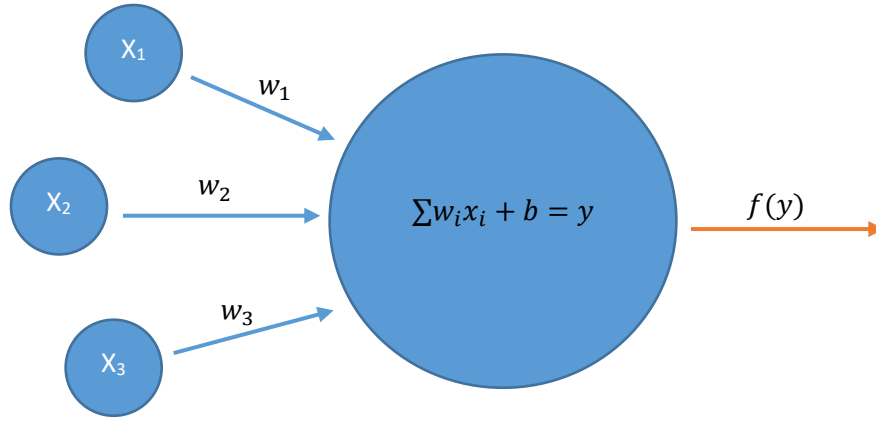
Figure 49: Functional layout of a perceptron. x_i represent inputs, w_i represent weights, b is the bias, and f(y) is the output.

To perform complex tasks, a network of interconnected perceptrons is created. The perceptrons can be connected in multiple ways; Figure 50 represents a Fully Connected NN. Each node in this network represents a perceptron. Each edge represents a connection between two perceptrons, in which the output of a perceptron on the left is received as an input for the perceptron on the right. The perceptrons are categorized into categories called layers. All perceptrons belonging to the same layer are vertically aligned in the Figure 50. In this model a perceptron from a particular layer is not connected to the other perceptrons of the same layer; however, it is connected to all the perceptrons from the adjacent two layers.

There are three types of layers in the NN. The first type is called the Input layer. It receives the spectral data for the NN. Each perceptron in this layer receives the intensity value from a unique frequency along the input spectra and then passes it without modification to all the perceptrons in the next layer.

The next layer is called a Hidden layer because its inputs and outputs are not observable outside the NN. Perceptrons in the hidden layer calculate the weighted sums and generate outputs, which are then sent to every perceptron in a second Hidden layer. Perceptrons from both hidden layers utilize rectified linear function for computing the output from the weighted sums of the inputs. The outputs of the perceptrons in the second Hidden layer sent to the perceptrons in the final layer called the Output layer.

In the Output layer, each perceptron utilizes the sigmoid function to compute its output from the weighted sum. The output of all the perceptrons in the Output layer is combined to generate the final prediction by selecting the perceptron with highest numerical output.

In a NN there can be multiple hidden layers with multiple perceptrons but only one input and one output layer. For the chemical identification of a given SFG spectrum, the number of wavelengths in the spectrum determines the number of perceptrons in the input layer, whereas the number of chemical labels available for the prediction determines the number of perceptrons in the output layer. For example, for the classification of SFG spectra from five different SAMs, each containing 71 unique wavelengths, a NN will have 71 perceptrons in the input layer and 5 perceptrons in the output layer. Each perceptron of the Output layer will generate the probability that the input spectrum belongs to a certain class.
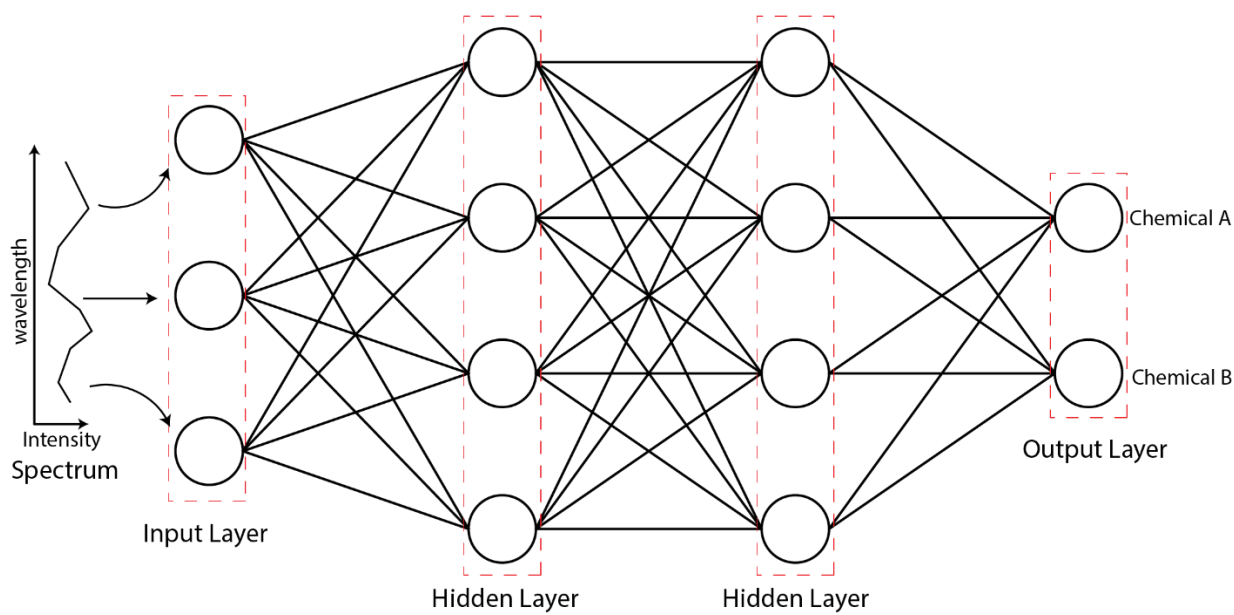
Figure 50: A fully connected Neural Network with two hidden layers. The input layer has three perceptrons, the hidden layers have four perceptrons each, and the output layer contains two perceptrons. The spectral data enters the network from the left. The Output layer perceptrons generate the probabilities of possible chemical labels for the spectra.

For a NN to produce the desired performance, the weights for every perceptron in the network need to be configured. This is achieved by training the NN on spectra with known qualities. For example, if a NN is tasked with identifying which chemical a given spectrum belongs to, the NN will be trained on spectra of different chemicals. In the training process, the NN will start with random values for the weights in each perceptron. The predicted chemical label will be compared with the real chemical identity of the input spectrum called ground truth. If the prediction is incorrect, the weights of the perceptrons will be methodically corrected. This process will be repeated until desired prediction accuracy is achieved. Once the NN is trained to a required level of prediction accuracy, it can be used to provide chemical labels for spectra with unknown identities.

NNs are susceptible to overtraining, a condition where model's performance starts degrading on unseen test data but becomes better on training data. To avoid this condition, the training and testing errors are often recorded throughout the training cycles; and the training is stopped before the overfitting takes place [165].

6.3 Sample – Self Assembled Monolayers

A particular class of molecules produces highly ordered, well packed, and well oriented single molecule thick layers on substrates, often by solution deposition. These molecular monolayers are termed Self-Assembled Monolayers (SAMs) [176-180]. Although they are just monolayers, they can still alter the wetting [181, 182], catalysis [183, 184], oxidation [11], and other chemical properties of the substrates making them valuable systems for both scientific and engineering research. Furthermore, SAMs also provide ideal systems for studying surface specific spectroscopic techniques because these monolayers can be engineered with desired spatial heterogeneity, chemical signature, and orientation. Consequently, they have been a system-of-choice for studying SFG spectroscopic imaging [44, 45, 85, 88].

Alkane thiols produce SAMs on gold substrates [177]. These molecules consist of a long alkane chains with thiol head groups that bind to the gold surface. These monolayers can be prepared by solution deposition as well as stamping using PDMS patterns inked with the alkane thiol solutions (in a process called micro-contact printing) [44, 87, 88, 185]. The visibility of the SFG resonance response from the functional groups on the SAMs is also enhanced by high non-resonance SFG response of the gold substrate. This makes them ideal to test SFG spectroscopic microscopies.

The SFG imaging data was provided by Dr Alex Pikalov from Baldelli Surface Lab at University of Houston. To generate data with known chemical identities, five alkane thiol SAMs with

different chemical structures were prepared on gold substrates through solution deposition. The chemical structures of these molecules are shown in Figure 51. The details of preparation can be found elsewhere [87].
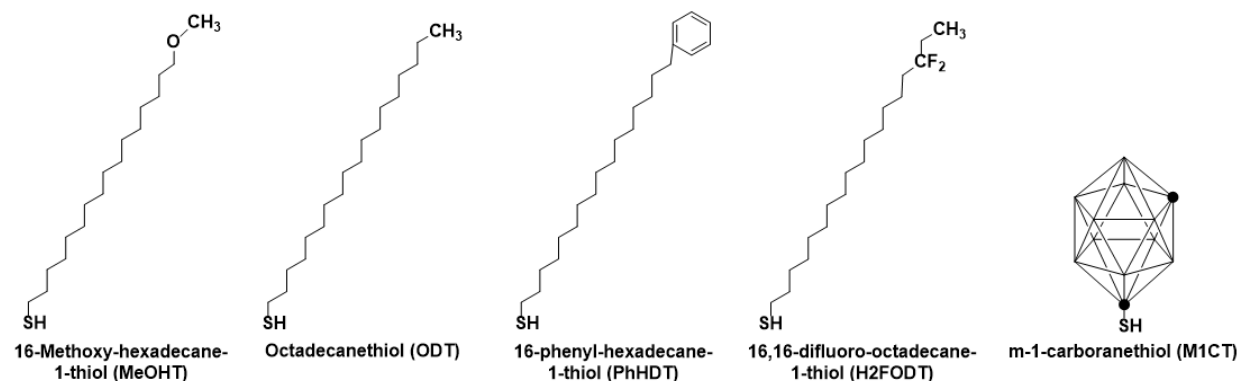
Figure 51: Alkane thiols used to prepare data for Neural Network training and testing [87].

Furthermore, an additional sample was created with four SAMs deposited through micro-contact printing and fifth one by solution deposition. The details of the procedure are described here [87].

6.4 SFG Imaging Setup

Combining mid-IR and 1064 nm laser beams produces SF close to 815 nm, which can be directly imaged by an intensified CCD camera [186-189]. The basic setup is shown in Figure 52. The 1064 nm and mid-IR beams from the OPG/OPA, are spatially and temporally over-lapped on the sample at 70° and 60°, respectively. This generates SFG from the sample at approximately 62.1° from the surface normal. The SFG beam is passed through a 1:1 relay lens to maintain the size and focus of the beam. It is then reflected off a diffraction grating that helps correct for the depth of field due to oblique geometry. The fundamental reflection from the grating is passed through a 10X microscope objective to magnify the image. A collimating tube lens and a pair of

gold mirrors then send the SF beam to an intensified CCD camera with 1064×1064 pixels. The intensified CCD camera is cooled to $-20\ °C$ and gated with a gate-width of 10 ns to suppress the thermal and background signals [186, 187]. The resulting setup generates a resolution of at least $1.2\ \mu m$ for the surface specific SFG imaging.
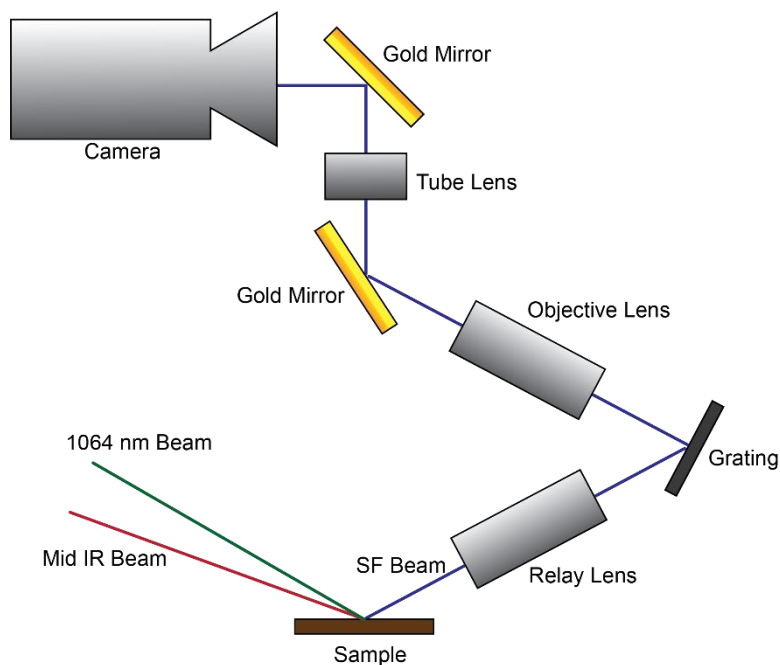
Figure 52: Schematic for direct imaging SFG microscope setup. The SF beam is represented by a blue line. The relay lens provides a one-to-one mapping of the surface to the grating. The microscope objective provides a 10X effective magnification [87].

SFG imaging is performed on five solution deposited SAMs on gold substrates by continuously scanning the mid-IR frequency from $2750\ cm^{-1}$ to $3100\ cm^{-1}$. The CCD camera saves an image after every one thousand laser pulses. Meanwhile, the mid-IR frequency changes by $5\ cm^{-1}$. Therefore, after scanning the required mid-IR range, a stack of 71 SF images is created. The pixel spectrum in each stack contains 71 data points (Figure 53).
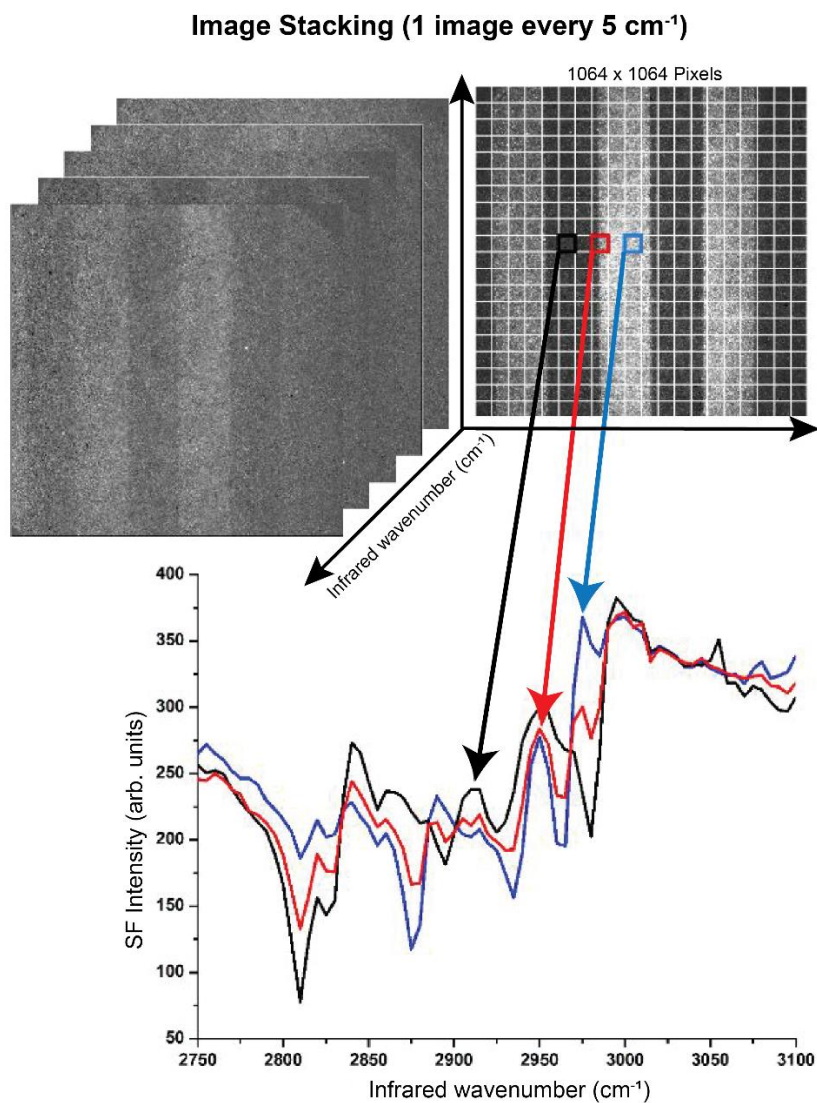
Figure 53: Mid-IR is scanned and an SFG image is acquired for every 5 wavenumbers. The image stack is shown in the top left corner. The top right corner shows a representative image from the stack with pixel binning. Extracted spectra form different regions of interest with binned pixels are represented in the bottom half [45].

6.5 Data preparation

The image stacks obtained from five different solution deposited SAMs samples were utilized to create labeled spectra. From each stack, pixels containing abnormal signals due to cosmic noise or

stray light were discarded by eliminating those pixel spectra that contained intensities that were 5 times the average intensity for the entire image at any wavelength. The remaining pixels were processed using steps shown in Figure 54.
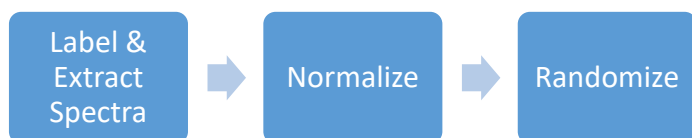
Figure 54: Data processing steps for creating training and testing data.

From the image stack of each SAMs, 71-point spectra were extracted from every pixel. These spectra were labelled with the SAMs of their corresponding image stack. This created a data set containing correctly labelled spectra. This dataset was only compatible for training NNs for chemical identification; however, for predicting additional molecular features for the surface species, new datasets were required.

In the imaging process, the spatial variation of the intensity in laser beams can create variation in the image. To remove these artifacts, each spectrum was normalized to a range of 0 to 1. This normalization also helps avoid any training bias towards high intensity spectra because computer algorithms often prioritize reducing errors on large valued inputs during training/optimization. The presence of noise, however, did not introduce bias because of random distribution of noise. In the SF image, the neighboring pixels can show slightly correlated spectral behavior. For current task, learning such correlations can cause overfitting. Therefore, to avoid overfitting, spectra were randomly shuffled. Finally, to create binned pixel data, spectra form multiple pixels were averaged.

6.6 Neural Network Training

The NNs were created in Python using Tensorflow library. The NN architecture consisted of 4 layers of perceptrons i.e., one input, two hidden, and one output layers. Each perceptron in the Input layer received the intensity value at a specific mid-IR wavenumber from the spectrum; thus, 71 input perceptrons cover the entire frequency range for the spectrum.

Every Input layer perceptron is then connected to all the perceptrons in the 1st Hidden layer. This Hidden layer contains 1000 perceptrons. These perceptrons pass their output to all the 100 perceptrons in the 2nd Hidden layer. In both hidden layers, the perceptrons used Rectified Linear Function for generating output from weighted sums of the inputs.

Every perceptron in the 2nd Hidden layer then passes its output to all five perceptrons of the final Output layer. These perceptrons utilize sigmoid function for generating the output from weighted sum of the inputs. Each one of the five perceptrons in the Output layer represents a particular SAM and generates an output value from zero to one. The output values of all five sum to one. Therefore, for any spectral input, these output values are the probabilities for the associated chemical labels. Finally, the input spectra are assigned the chemical label associated to the perceptron with maximum output value in the final layer.

To provide training and testing using spectra with known chemical identities, 70 % of the spectral dataset was used for training and 30 % was used for testing. The training spectral data was passed through the NNs multiple times and the network predictions were compared to the actual identities of the spectra. The misclassification error was calculated and then used to correct the weights of the perceptrons. After each session of training (called epoch), the NNs were

tested/validated on the remaining 30 % of the spectra, which were kept hidden from the NNs during the training phase. This created a benchmark for performance using completely unseen data after the NNs were trained on all five SAMs. Further details are provided in the appendix.

6.7 Results and Discussion

The experiments were performed with both binned and un-binned pixels. The average spectra of the entire image stacks for all five SAMs are shown in Figure 55.
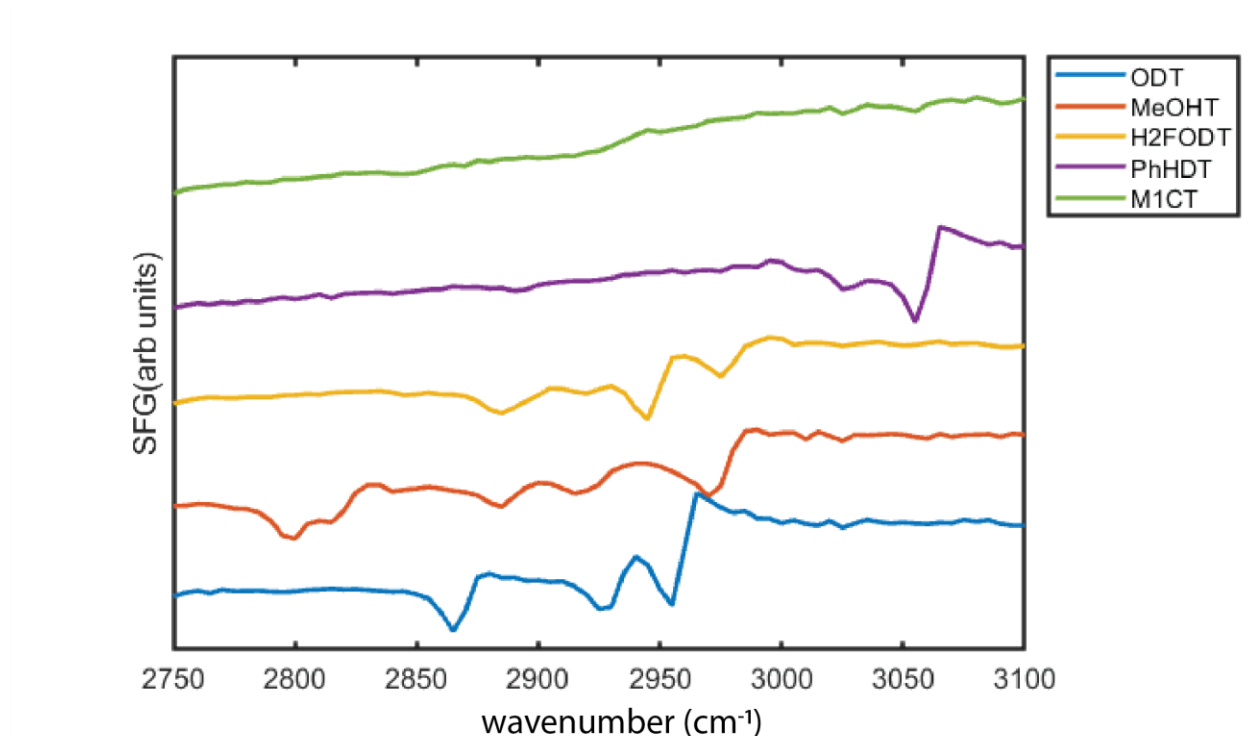
Figure 55: Spectra for SAMs from all pixels of the image stack.

However, some spectra from single pixels are shown in Figure 56 and 8x8 binning are shown Figure 57.
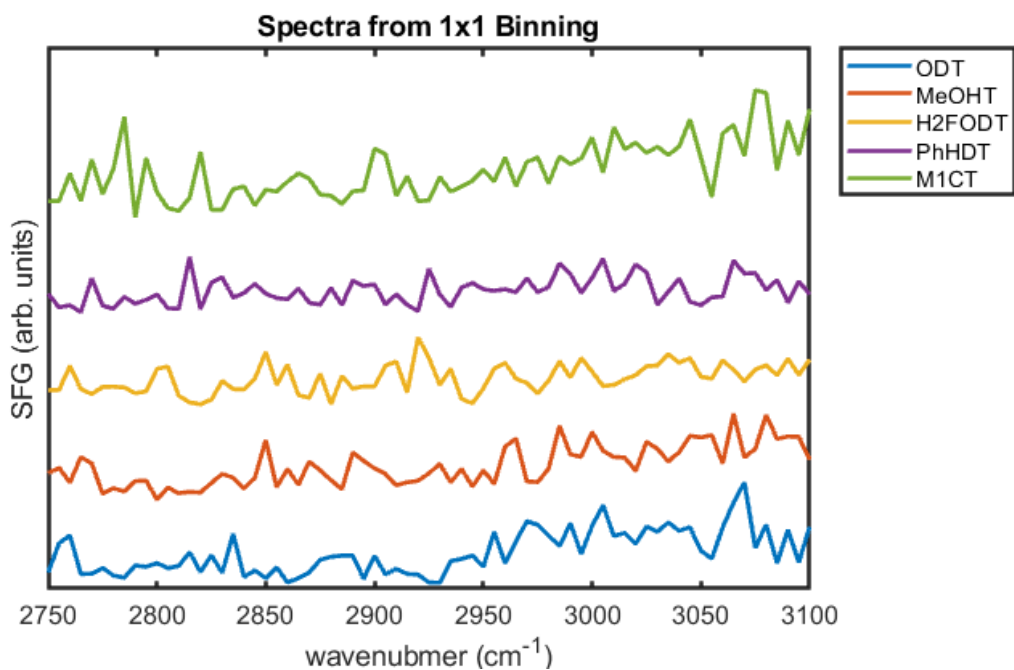
Figure 56: Example spectra from single pixels from image stacks of 5 different SAMs. These spectra have extremely low signal to noise ratio and are difficult to distinguish by spectroscopic intuition or spectral fitting.
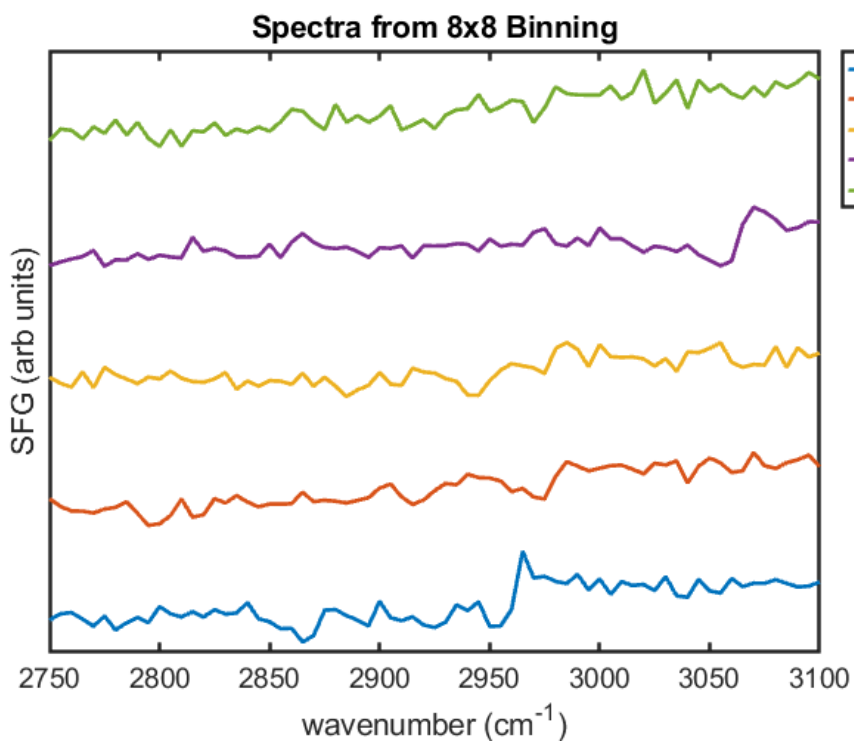
Figure 57: The spectra from binned image stacks of 5 different SAMs.

These figures indicate that the characteristic spectral features of each individual SAMs are prominent in the spectra obtained by averaging the entire image. These features are still identifiable in 8x8 binning. However, at 8x8 binning with 64 pixels averaged together, enough noise is present which can create large margins of error in a typical spectral fitting. At 1x1 level the spectral features are completely overtaken by noise. Therefore, under these circumstances, a typical spectral fitting technique would require at least 8x8 binning or more.

The NNs were trained and tested on 1x1, 2x2, 4x4, and 8x8 binned data. The results are summarized in Table 4. These values were obtained by matching the chemical labels for the maximum output value perceptrons in the output layer with the true identities of the input spectra determined experimentally. The accuracy in this discussion refers to the percentage of correct classifications.

Table 4: The test or validation accuracy of trained NNs on completely unseen data

	1x1	2x2	4x4	8x8
Correct Classification Percentage (Accuracy)	92	93.5	97.5	99.5
Pixels	1	4	16	64

The NNs performed perfect classification on 8x8 binning. At single-pixel level the chemical identification accuracy calculated from the misclassification error was still above 92 %. The relationship of the accuracy with the number of pixels averaged for the input spectra, shows the performance saturates close to ~100 % accuracy at 8x8 binning (Figure 58).
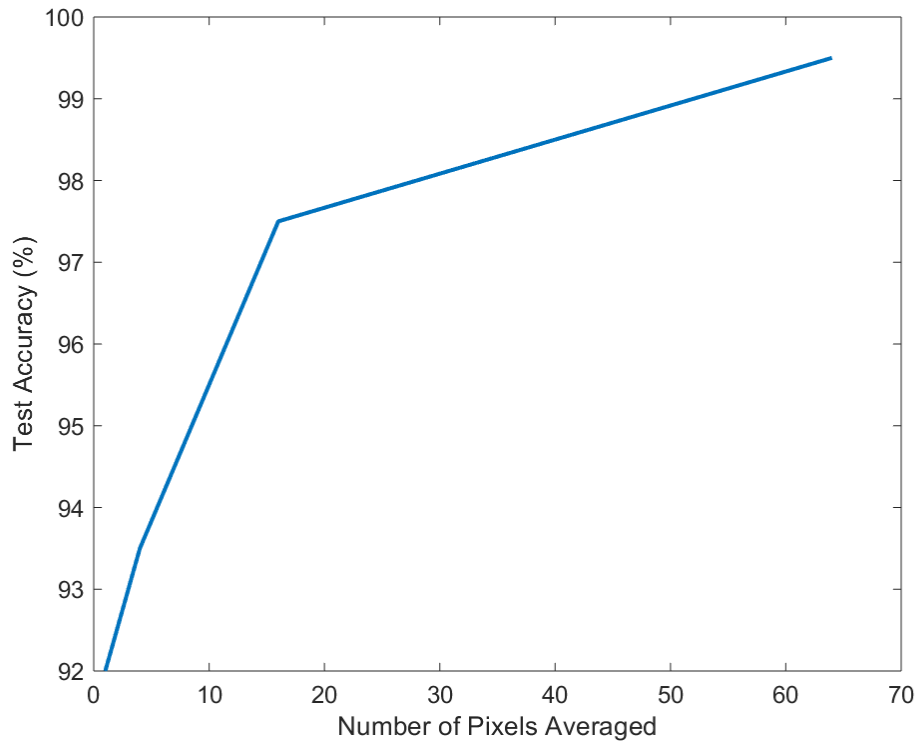
Figure 58: Relation between the accuracy and the number of pixels averaged for each spectrum.

To ensure overfitting does not take place during the training cycles, the accuracy on training and validation data is recorded for single pixels in Figure 59 and for 8x8 binning in Figure 60.

During the training cycles, with 8x8 binning data, the accuracy saturates immediately at a high level. As the training continues, the validation accuracy slightly drops indicating an overfitting. However, with comparatively noisy, single-pixel spectra the accuracy levels-off slowly at a relatively low value.
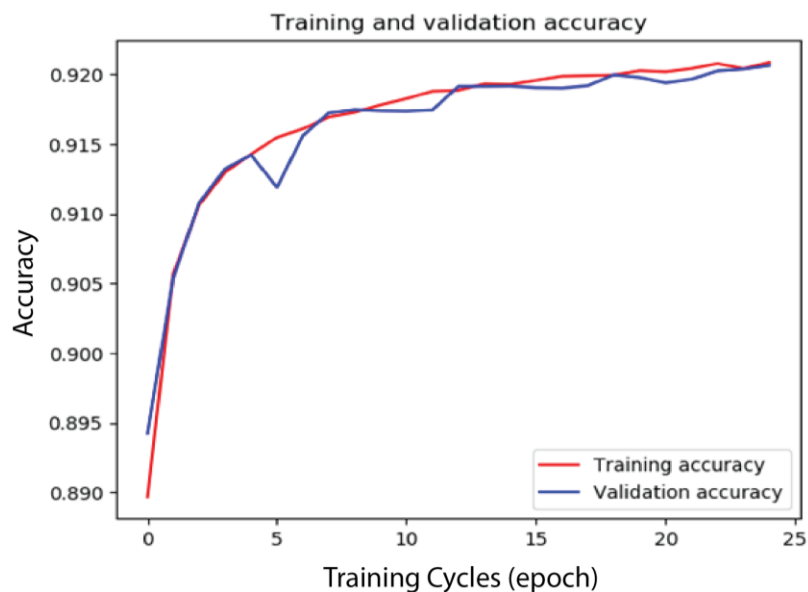
Figure 59: Tracking overfitting for training with single-pixel spectra.
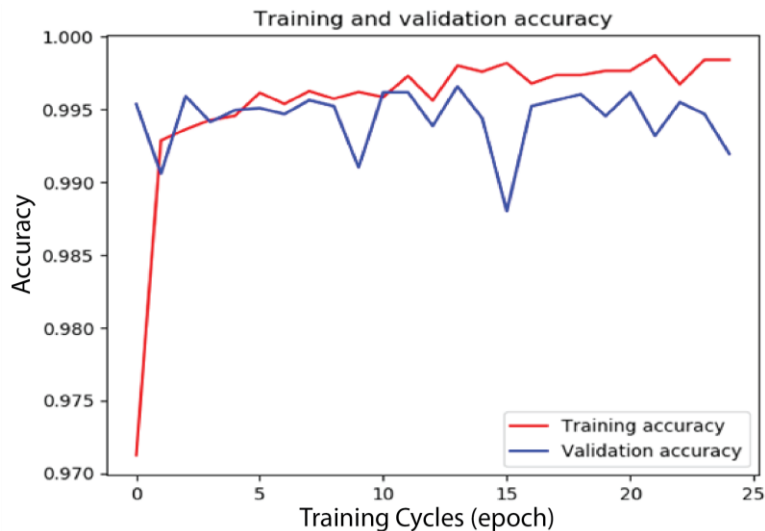
Figure 60: Tracking overfitting for training with 8x8 binned pixel spectra.

To further test the robustness of NNs for chemical identification, another image stack was acquired under slightly different laser conditions. The sample contained all 5 SAMs on a single gold substrate. ODT, MeOHT, PhHDT, and H2F were micro contact printed on the gold substrate using PDMS stamp. Afterwards M1CT was solution deposited on the open spaces in the patterns [87].

97

The single-pixel spectra were passed through a NN trained on the previous dataset and the resulting predictions for each SAMs were recorded. The predicted probabilities of each SAM were then plotted as intensity values on the corresponding pixel positions to generate an image.

The results (shown in Figure 61) produced spatial distributions, which were qualitatively similar to the shapes of stamp patterns used to create the sample. The backfilled M1CT also follows the gaps in patterns as expected from the solution deposition process. However, in this sample a quantitative comparison is not possible because the exact chemical identities of the single-pixel spectra are not known by any independent means.
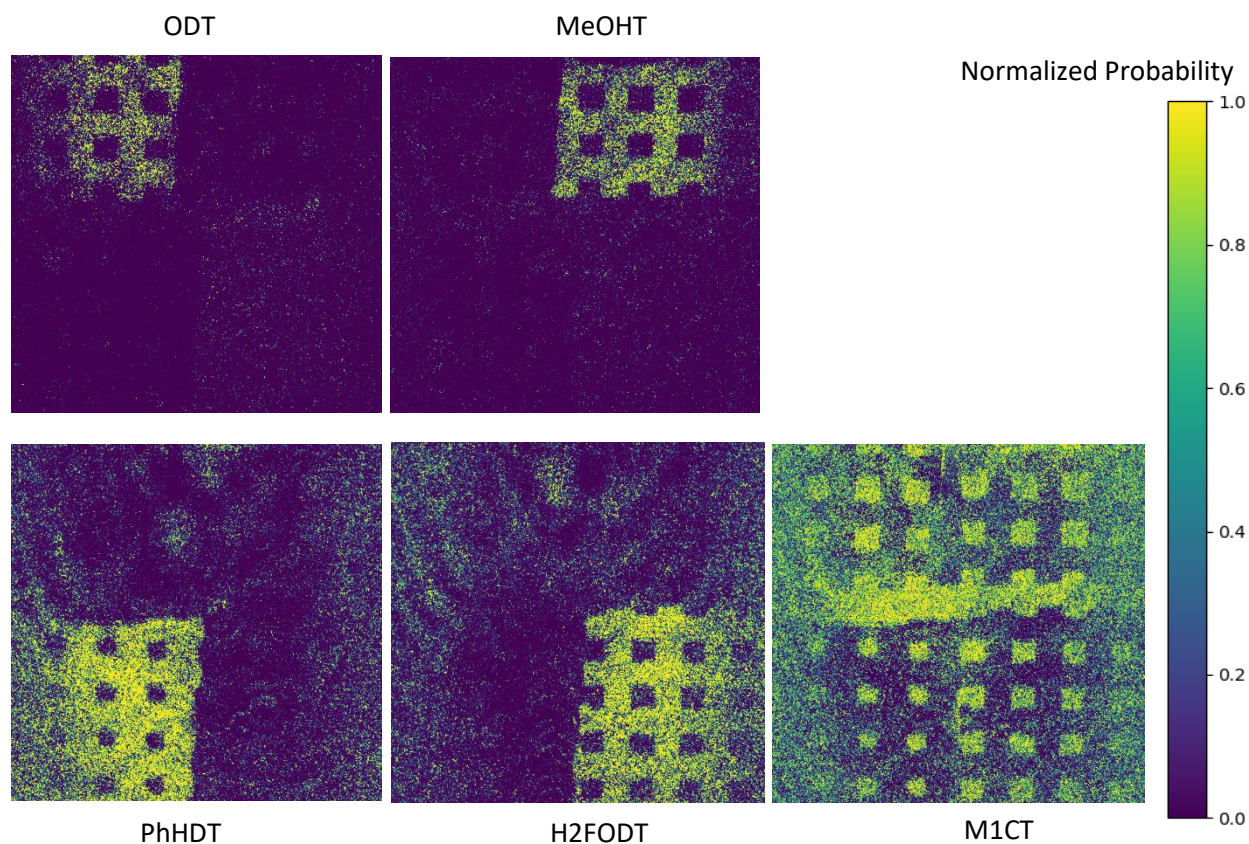
Figure 61: Spatial maps for SAMs generated by trained NNs on the single-pixel spectra. Each frame is a probability map for a single component. These spatial maps follow the shape of stamp patters used to create the SAMs.

To understand these results better, Figure 62 and Figure 63 represent binary spatial maps for different SAMs, which are created by applying 10% and 90% probability thresholds, respectively. In Figure 62, any pixel that has 10% or more probability for a particular SAM, is included in the spatial map of that SAM. On the other hand, in Figure 63, only those pixels are included in the spatial map, which carry more than 90% probability for that particular SAM. These figures effectively represent 10% and 90% confidence maps. In Figure 62, many pixels that are outside the experimentally assigned area are included in the spatial maps for different SAMs. The highest spillover is shown by M1CT. It is possibly due to the back-filling method used for its deposition.
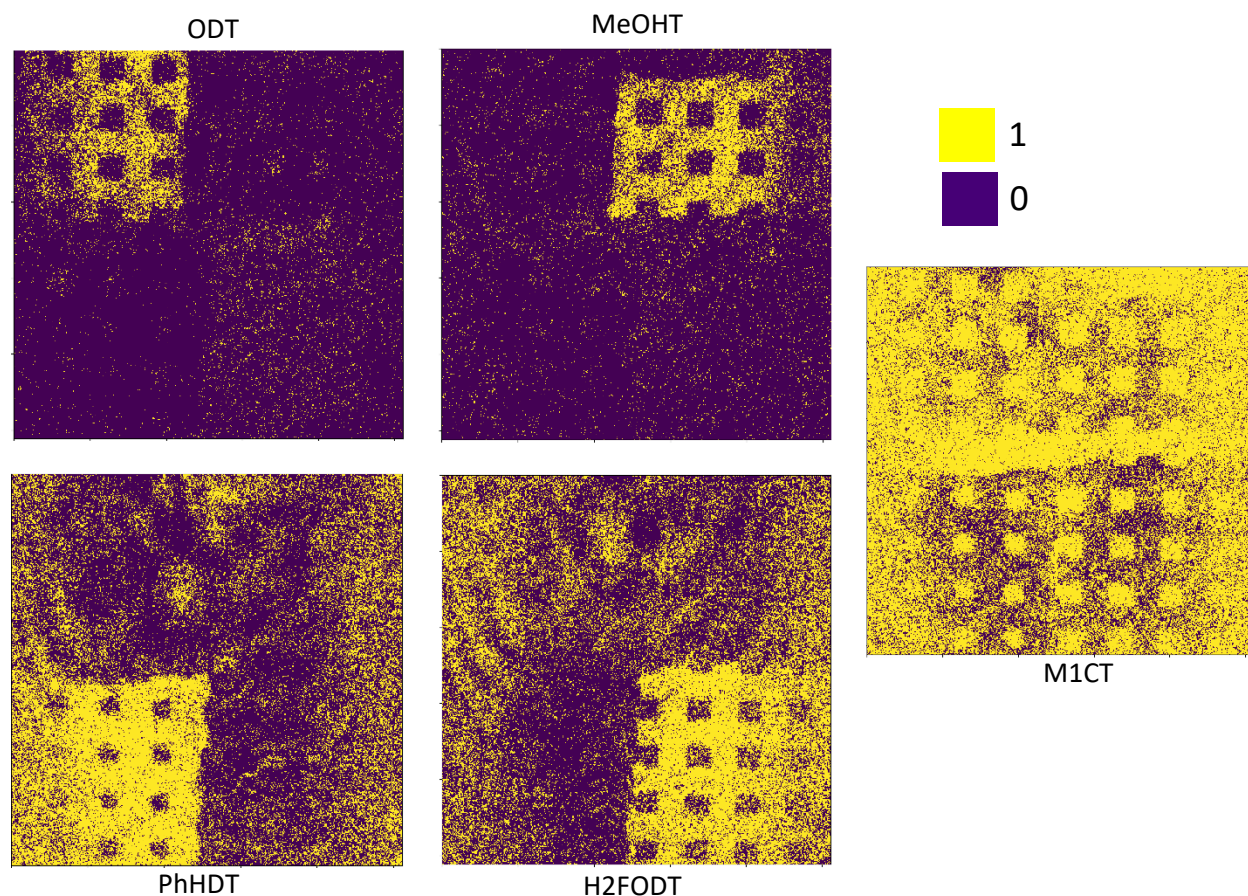
Figure 62: Binary spatial maps for different SAMs with 10% probability threshold. Any pixel that has greater than 10% probability for a SAM, is included in the map of that particular SAM.

For the 90% probability threshold, the five maps are predominantly confined to the experimentally assigned areas (selected during sample preparation process). Still, multiple pixels outside these regions show more than 90% probability. They can be considered misclassifications qualitatively.
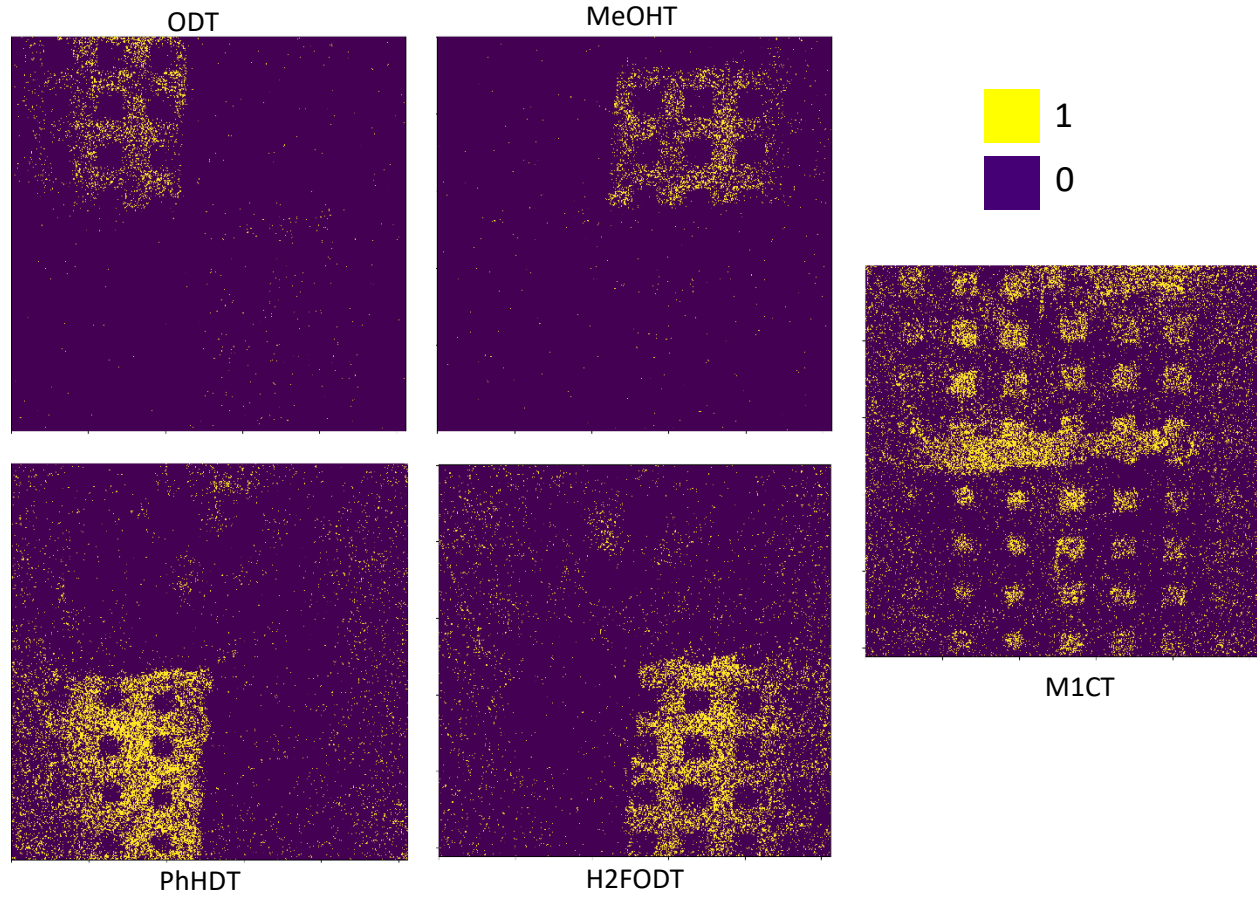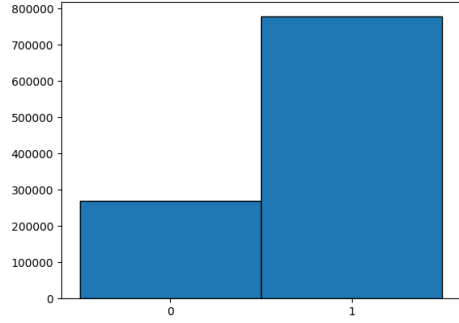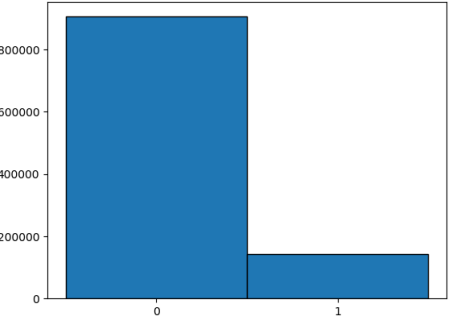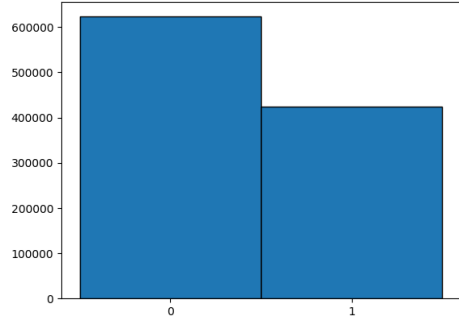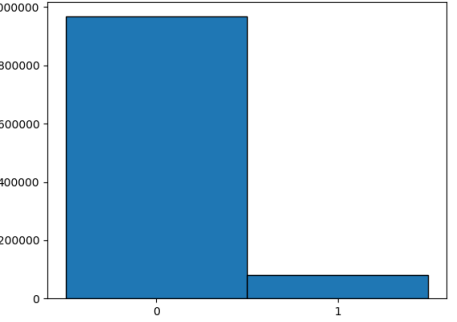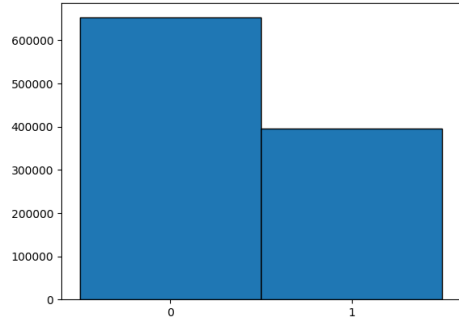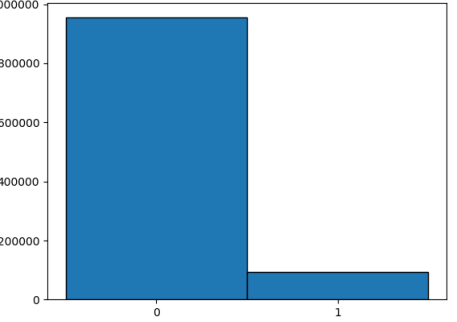
Figure 63: Binary spatial maps for different SAMs with 90% probability threshold. In these binary maps, only those pixels are included that show more than 90% probability for the corresponding SAMs.

The histograms for the maps shown in Figure 62 and Figure 63 are shown in Table 5. These histograms indicate that M1CT, H2FODT, and PhHDT occupy the majority of pixels at 10% probability threshold. On the other hand MeOHT and ODT are absent from most pixels. When the threshold is increased to 90%, all SAMs report pixel loss. The highest variation is

observed in M1CT, which is the only SAMs that exhibits more 1's than 0's at 10% probability threshold.

Table 5: Histograms for the binary spatial maps of SAMs using 10% and 90% probability threshold

	10% Probability Threshold	90% Probability Threshold
M1CT		
H2FODT		
PhHDT		

MeOHT		
ODT		
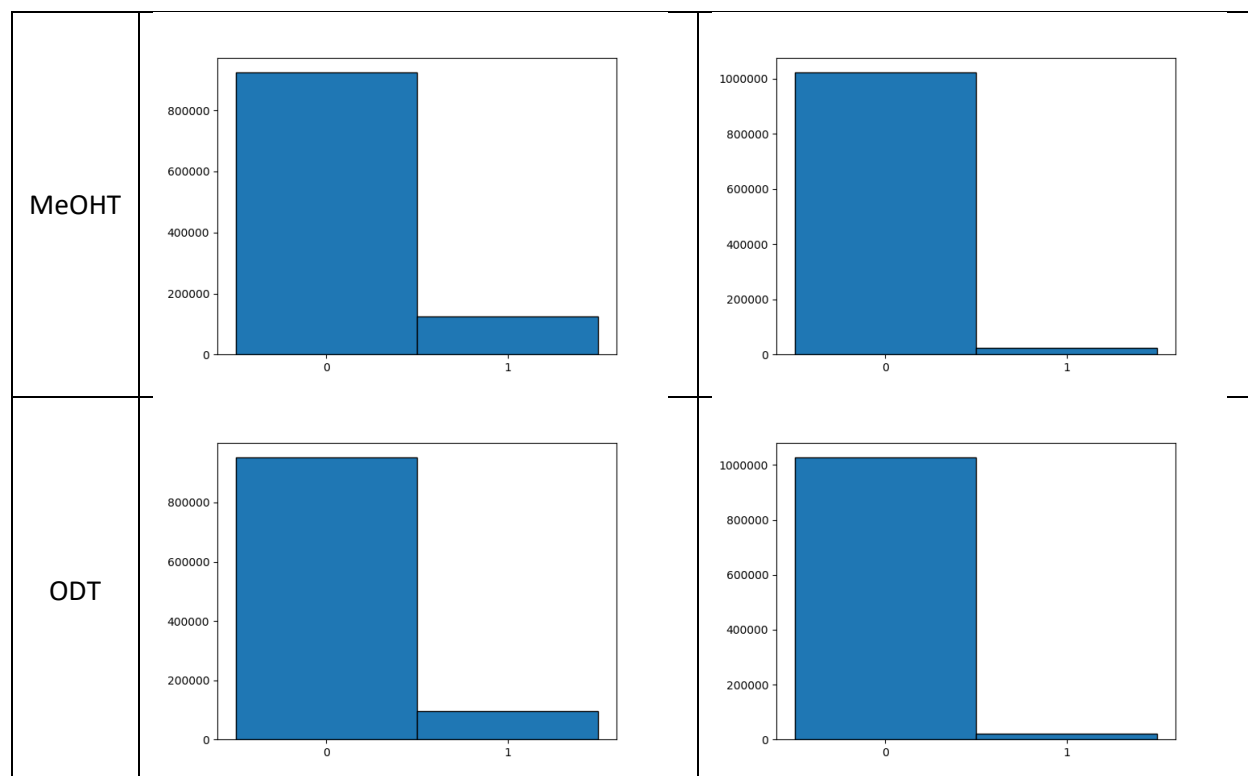
6.8 Conclusion

SFG spectroscopic imaging provides a unique tool to study the surface specific physical and chemical processes with spatial information. However, typically low signal levels generate poor signal-to-noise ratio. Consequently, long acquisition time or high spatial binning is required for extracting the chemical identities of the image pixels through spectral fitting. However, this adversely affects the duration and spatial-resolution of the SFG imaging. To overcome these challenges, NNs have shown high accuracy and potential for the chemical identification of pixels with extremely noisy spectra.

Although NNs have been tested on data with chemical contrast originating from the difference in the terminal groups, the approach can be generalized. If relevant training data is available, these NNs can be trained to identify other chemical properties that cause SFG image contrast; such as molecular orientation and spatial packing.

Another successful technique for identifying chemical identities of the spectra contained in SFG imaging is Target Factor Analysis (TFA) [45, 87], which is based on singular value decomposition of different geometric and spectral elements present in the image. TFA results in spatial maps of the chemical distribution. The results generated by NNs presented here qualitatively match with the TFA results for the same dataset. The two techniques can be used to corroborate each other.

Bibliography

1. Somorjai, G.A. and Y. Li, *Impact of surface chemistry.* Proceedings of the National Academy of Sciences 2011, **108**(3): p. 917-924.
2. Hiemenz, P.C. and R. Rajagopalan, *Principles of colloid and surface chemistry, revised and expanded.* 2016: CRC press.
3. Somorjai, G.A. and Y. Li, *Introduction to surface chemistry and catalysis*. 2nd Edition. 2010, Wiley. xii, 771 p.
4. Albanese, A., P.S. Tang, and W.C. Chan, *The effect of nanoparticle size, shape, and surface chemistry on biological systems.* Annual Review of Biomedical Engineering 2012, **14**: p. 1-16.
5. Thevenot, P. et. al., *Surface chemistry influences cancer killing effect of TiO2 nanoparticles.* Nanomedicine: Nanotechnology, Biology and Medicine 2008, **4**(3): p. 226-236.
6. Landolt, D., *Corrosion and surface chemistry of metals*. 2007: CRC press.
7. Abbott, N.L., J.P. Folkers, and G.M. Whitesides, *Manipulation of the wettability of surfaces on the 0.1-to 1-micrometer scale through micromachining and molecular self-assembly.* Science, 1992. **257**(5075): p. 1380-1382.
8. Zhu, L. et al., *Tuning wettability and getting superhydrophobic surface by controlling surface roughness with well-designed microstructures.* Sensors and Actuators A: Physical 2006, **130**: p. 595-600.
9. Engelman, D.M., *Membranes are more mosaic than fluid.* Nature, 2005. **438**(7068): p. 578-580.
10. Kim, B.J., et al., *Importance of end-group structure in controlling the interfacial activity of polymer-coated nanoparticles.* Macromolecules 2007, **40**(6): p. 1796-1798.
11. Laibinis, P.E. and G.M. Whitesides, *Self-assembled monolayers of n-alkanethiolates on copper are barrier films that protect the metal against oxidation by air.* Journal of the American Chemical Society 1992, **114**(23): p. 9022-9028.
12. Igarashi, H. et al., *Removal of carbon monoxide from hydrogen-rich fuels by selective oxidation over platinum catalyst supported on zeolite.* Applied Catalysis A 1997, **159**(1): p. 159-169.
13. Qin, L. et al., *Achieving excellent anti-corrosion and tribological performance by tailoring the surface morphology and chemical composition of aluminum alloys.* Royal Society of Chemistry Advances 2014, **4**(104): p. 60307-60315.
14. Whitesides, G.M. and P.E. Laibinis, *Wet chemical approaches to the characterization of organic surfaces: self-assembled monolayers, wetting, and the physical-organic chemistry of the solid-liquid interface.* Langmuir 1990, **6**(1): p. 87-96.
15. Samjeské, G., K.-i. Komatsu, and M. Osawa, *Dynamics of CO oxidation on a polycrystalline platinum electrode: A time-resolved infrared study.* The Journal of Physical Chemistry C 2009, **113**(23): p. 10222-10228.
16. Wakisaka, M. et al., *Identification and Quantification of Oxygen Species Adsorbed on Pt(111) Single-Crystal and Polycrystalline Pt Electrodes by Photoelectron Spectroscopy.* Langmuir 2009, **25**(4): p. 1897-1900.
17. Müller, U. and H. Baltruschat, *Displacement of ethene and cyclohexene from polycrystalline Pt and Pt(110) electrodes.* The Journal of Physical Chemistry B 2000, **104**(24): p. 5762-5767.

18. Schrader, A.M. et al., *Surface chemical heterogeneity modulates silica surface hydration.* Proceedings of the National Academy of Sciences 2018, **115**(12): p. 2890-2895.

19. Branton, D. and D.W. Deamer, *Membrane structure*, in *Membrane Structure*. 1972, Springer. p. 1-70.

20. Binnig, G. et al., *Surface studies by scanning tunneling microscopy.* Physical Review Letters 1982, **49**(1): p. 57-61.

21. Vancsó, P. et al., *The intrinsic defect structure of exfoliated MoS2 single layers revealed by Scanning Tunneling Microscopy.* Scientific Reports 2016, **6**: p. 29726.

22. Giessibl, F.J., *Advances in atomic force microscopy.* Reviews of Modern Physics 2003, **75**(3): p. 949-983.

23. Han, T., J.M. Williams, and T.P. Beebe, *Chemical bonds studied with functionalized atomic force microscopy tips.* Analytica Chimica Acta 1995, **307**(2): p. 365-376.

24. Barattin, R. and N. Voyer, *Chemical modifications of AFM tips for the study of molecular recognition events.* Chemical Communications 2008, (13): p. 1513-1532.

25. Iwamoto, R. et al., *Total internal reflection Raman spectroscopy.* The Journal of Chemical Physics 1981, **74**(9): p. 4780-4790.

26. Hoffmann, F.M., *Infrared reflection-absorption spectroscopy of adsorbed molecules.* Surface Science Reports 1983, **3**(2): p. 107-192.

27. Ivleva, N.P. et al., *Label-free in situ SERS imaging of biofilms.* Journal of Physical Chemistry B 2010, **114**(31): p. 10184-94.

28. Stranahan, S.M. and K.A. Willets, *Super-resolution optical imaging of single-molecule SERS hot spots.* Nano Letters 2010, **10**(9): p. 3777-84.

29. Palonpon, A.F. et al., *Raman and SERS microscopy for molecular imaging of live cells.* Nature Protocols 2013, **8**(4): p. 677-92.

30. Lee, A.F. et al., *A Fast XPS study of the surface chemistry of ethanol over Pt{111}.* Surface Science 2004, **548**(1): p. 200-208.

31. Takayanagi, K. et al., *Structure analysis of Si(111)-7 × 7 reconstructed surface by transmission electron diffraction.* Surface Science 1985, **164**(2): p. 367-392.

32. Miller, D.J. et al., *Oxidation of Pt(111) under near-ambient conditions.* Physical Review Letters 2011, **107**(19): p. 195502.

33. Leadley, S.R. et al., *Analysis of the surface chemical structure of copolymers of poly(sebacic anhydride) with ricinoleic acid maleate using XPS and ToF–SIMS.* Macromolecules 1998, **31**(25): p. 8957-8965.

34. Kusakari, M. et al., *Development of ambient SIMS using mega-electron-volt-energy ion probe.* Journal of Vacuum Science Technology B 2016, **34**(3): p. 03H111.

35. Monte, M. et al., *Near-ambient XPS characterization of interfacial copper species in ceria-supported copper catalysts.* Physical Chemistry Chemical Physics 2015, **17**(44): p. 29995-30004.

36. Newberg, J.T. et al., *Formation of hydroxyl and water layers on MgO films studied with ambient pressure XPS.* Surface Science 2011, **605**(1-2): p. 89-94.

37. Salmeron, M. and R. Schlögl, *Ambient pressure photoelectron spectroscopy: A new tool for surface science and nanotechnology.* Surface Science Reports 2008, **63**(4): p. 169-199.

38. Ali-Löytty, H. et al., *Ambient-pressure XPS study of a Ni–Fe electrocatalyst for the oxygen evolution reaction.* The Journal of Physical Chemistry C 2016, **120**(4): p. 2247-2253.

39. Shen, Y.R., *Surface properties probed by second-harmonic and sum-frequency generation.* Nature 1989, **337**(6207): p. 519-525.

40.   Gan, W. et al., *Polarization and experimental configuration analyses of sum frequency generation vibrational spectra, structure, and orientational motion of the air/water interface.* The Journal of Chemical Physics 2006, **124**(11): p. 114705.

41.   Shen, Y.R., *Surfaces probed by nonlinear optics.* Surface Science, 1994. **299-300**: p. 551-562.

42.   Wang, H.-F., *Sum frequency generation vibrational spectroscopy (SFG-VS) for complex molecular surfaces and interfaces: Spectral lineshape measurement and analysis plus some controversial issues.* Progress in Surface Science 2016, **91**(4): p. 155-182.

43.   Wang, H.-F. et al., *Quantitative sum-frequency generation vibrational spectroscopy of molecular surfaces and interfaces: lineshape, polarization, and orientation.* Annual Review of Physical Chemistry 2015, **66**(1): p. 189-216.

44.   Cimatu, K. and S. Baldelli, *Sum frequency generation microscopy of microcontact-printed mixed self-assembled monolayers.* Journal of Physical Chemistry B 2006, **110**(4): p. 1807-13.

45.   Pikalov, A.A. et al., *Sum frequency generation imaging microscopy of self-assembled monolayers on metal surfaces: factor analysis of mixed monolayers.* Analytical Chemistry 2019, **91**(2): p. 1269-1276.

46.   Zheng, D. et al., *Chemical Imaging of Self-Assembled Monolayers on Copper Using Compressive Hyperspectral Sum Frequency Generation Microscopy.* Journal of Physical Chemistry B 2018, **122**(2): p. 464-471.

47.   Aliaga, C. and S. Baldelli, *Sum frequency generation spectroscopy of dicyanamide based room-temperature ionic liquids. Orientation of the cation and the anion at the gas-liquid interface.* Journal of Physical Chemistry B 2007, **111**(33): p. 9733-40.

48.   Baldelli, S., *Interfacial structure of room-temperature ionic liquids at the solid-liquid interface as probed by sum frequency generation spectroscopy.* Journal of Physical Chemistry Letters 2013, **4**(2): p. 244-52.

49.   Iimori, T. et al., *Local structure at the air/liquid interface of room-temperature ionic liquids probed by infrared-visible sum frequency generation vibrational spectroscopy: 1-alkyl-3-methylimidazolium tetrafluoroborates.* Journal of Physicsl Chemistry B 2007, **111**(18): p. 4860-6.

50.   Iwahashi, T. et al., *Anion configuration at the air/liquid interface of ionic liquid [bmim]OTf studied by sum-frequency generation spectroscopy.* Journal of Physical Chemistry B 2008, **112**(38): p. 11936-41.

51.   Iwahashi, T. et al., *Alkyl-chain dividing layer at an alcohol/ionic liquid buried interface studied by sum-frequency generation vibrational spectroscopy.* Journal of Physical Chemistry Chemical Physics 2010, **12**(40): p. 12943-6.

52.   Penalber, C.Y., G.A. Baker, and S. Baldelli, *Sum frequency generation spectroscopy of imidazolium-based ionic liquids with cyano-functionalized anions at the solid salt-liquid interface.* Journal of Physical Chemistry B 2013, **117**(19): p. 5939-49.

53.   Penalber, C.Y. and S. Baldelli, *Observation of charge inversion of an ionic liquid at the solid salt-liquid interface by sum frequency generation spectroscopy.* Journal of Physical Chemistry Letters 2012, **3**(7): p. 844-7.

54.   Penalber, C.Y. et al., *Surface characterization of imidazolium-based ionic liquids with cyano-functionalized anions at the gas-liquid interface using sum frequency generation spectroscopy.* Physical Chemistry Chemical Physics 2012, **14**(15): p. 5122-31.

55.   Penalber-Johnstone, C. et al., *Sum frequency generation spectroscopy of tetraalkylphosphonium ionic liquids at the air-liquid interface.* Journal of Chemical Physics 2018, **148**(19): p. 193841.

56.   Rivera-Rubero, S. and S. Baldelli, *Influence of water on the surface of the water-miscible ionic liquid 1-butyl-3-methylimidazolium tetrafluoroborate: a sum frequency generation analysis.* Journal of Physical Chemistry B 2006, **110**(31): p. 15499-505.

57. Rollins, J.B., B.D. Fitchett, and J.C. Conboy, *Structure and orientation of the imidazolium cation at the room-temperature ionic liquid/SiO2 interface measured by sum-frequency vibrational spectroscopy.* Journal of Physical Chemistry B 2007, **111**(18): p. 4990-9.

58. Xu, S. et al., *Sum frequency generation spectroscopy study of an ionic liquid at a graphene-BaF2 (111) interface.* Journal of Physical Chemistry B 2014, **118**(19): p. 5203-10.

59. Morita, A., *Theory of Sum Frequency Generation Spectroscopy*, in *Lecture Notes in Chemistry,*. SpringerLink.

60. Bloembergen, N., *Nonlinear optics; a lecture note and reprint volume*. Frontiers in physics. 1965: W. A. Benjamin. xiii, 222 p.

61. Boyd, R.W., *Nonlinear optics*. 1992: Academic Press. xiii, 439 p.

62. Morita, A., *Theory of Sum Frequency Generation Spectroscopy*. Lecture Notes in Chemistry. Vol. 97. 2018: Springer.

63. Arnolds, H. and M. Bonn, *Ultrafast surface vibrational dynamics.* Surface Science Reports 2010, **65**(2): p. 45-66.

64. Zhu, X.D., H. Suhr, and Y.R. Shen, *Surface vibrational spectroscopy by infrared-visible sum frequency generation.* Physical Review B 1987, **35**(6): p. 3047-3050.

65. Guyot-Sionnest, P. et al., *Lifetime of an adsorbate-substrate vibration: H on Si(111).* Physical Review Letters 1990, **64**(18): p. 2156-2159.

66. Guyot-Sionnest, P., P. Dumas, and Y.J. Chabal, *Lifetime of an adsorbate-substrate vibration measured by sum frequency generation : H on Si(111).* Journal of Electron Spectroscopy and Related Phenomena 1990, **54-55**: p. 27-38.

67. Lüpke, G., N.H. Tolk, and L.C. Feldman, *Vibrational lifetimes of hydrogen in silicon.* Journal of Applied Physics 2003 **93**(5): p. 2317-2336.

68. Flörsheimer, M., C. Brillert, and H. Fuchs, *Chemical Imaging of Interfaces by Sum Frequency Microscopy.* Langmuir 1999, **15**(17): p. 5437-5439.

69. Hoffmann, D.M.P., K. Kuhnke, and K. Kern, *Sum-frequency generation microscope for opaque and reflecting samples.* Review of Scientific Instruments 2002, **73**(9): p. 3221-3226.

70. Chastang, J.C. in *Proceedings SPIE*, 1983.

71. Lee, C.M. et al., *Probing crystal structure and mesoscale assembly of cellulose microfibrils in plant cell walls, tunicate tests, and bacterial films using vibrational Sum Frequency Generation (SFG) spectroscopy.* Physical Chemistry Chemical Physics 2014, **16**(22): p. 10844-10853.

72. Lee, C.M. et al., *Multimodal Broadband Vibrational Sum Frequency Generation (MM-BB-V-SFG) Spectrometer and Microscope.* The Journal of Physical Chemistry B 2016, **120**(1): p. 102-116.

73. Li, D. et al., *Multimodal Nonlinear Optical Imaging of MoS2 and MoS2-Based van der Waals Heterostructures.* ACS Nano 2016, **10**(3): p. 3766-3775.

74. Fang, M. and S. Baldelli, *Grain Structures and Boundaries on Microcrystalline Copper Covered with an Octadecanethiol Monolayer Revealed by Sum Frequency Generation Microscopy.* The Journal of Physical Chemistry Letters 2015, **6**: p. 1454-1460.

75. Cai, X. et al., *Sum frequency generation-compressive sensing microscope.* The Journal of Chemical Physics 2011, **135**(19): p. 194202.

76. Fu, Y. et al., *Second harmonic and sum frequency generation imaging of fibrous astroglial filaments in ex vivo spinal tissues.* Biophysical Journal 2007, **92**(9): p. 3251-3259.

77. Raghunathan, V. et al., *Rapid vibrational imaging with sum frequency generation microscopy.* Optics letters 2011, **36**(19): p. 3891-3893.

78. ChungBoik, C.-Y. and E.O. Potma, *Biomolecular imaging with coherent nonlinear vibrational microscopy.* Annual Review of Physical Chemistry 2013, **64**(1): p. 77-99.

79.   Zheng, D. et al., *Compressive Broad-Band Hyperspectral Sum Frequency Generation Microscopy to Study Functionalized Surfaces.* The Journal of Physical Chemistry Letters 2016, **7**(10): p. 1781-1787.

80.   Zheng, D. et al., *Chemical imaging of self-assembled monolayers on copper using compressive hyperspectral sum frequency generation microscopy.* The Journal of Physical Chemistry B 2018, **122**(2): p. 464-471.

81.   Sun, Z., D. Zheng, and S. Baldelli, *Study of the Wetting of Paraffin Films on the Metal Surface in the Dynamic Dip-Coating Process Using Compressive-Sensing Sum-Frequency Generation Microscopy.* The Journal of Physical Chemistry C 2018, **122**(46): p. 26543-26553.

82.   EKSPLA, *Laser PL2143A/20 Technical Description & User's Manual.* 2001.

83.   Cimatu, K.L.A., *Sum frequency generation imaging microscopy*, in *Chemistry*. 2008., University of Houston.

84.   Zhang, J.-Y., *Optical parametric generation and amplification*. 2019: Routledge.

85.   Cimatu, K. et al., *Sum frequency generation imaging microscopy of patterned self-assembled monolayers with terminal −CH3, −OCH3, −CF2CF3, −C≡C, −Phenyl, and −Cyclopropyl groups.* The Journal of Physical Chemistry C 2008, **112**(37): p. 14529-14537.

86.   Koechner, W., *Solid-state laser engineering*. Vol. 1. 2013: Springer.

87.   Pikalov, A.A., *Sum frequency generation imaging microscopy: Factor analysis of mixed monolayers*. 2019, University of Houston.

88.   Cimatu, K. and S. Baldelli, *Sum Frequency Generation Microscopy of Microcontact-Printed Mixed Self-Assembled Monolayers.* The Journal of Physical Chemistry B 2006, **110**(4): p. 1807-1813.

89.   Tinnefeld, P., C. Eggeling, and S.W. Hell, *Far-Field Optical Nanoscopy*, in *Springer Series on Fluorescence, Methods and Applications,*. Springer. p. XII, 335 p. 104 illus., 74 illus. in color.

90.   Hell, S.W. and M. Kroug, *Ground-state-depletion fluorscence microscopy: A concept for breaking the diffraction resolution limit.* Applied Physics B 1995, **60**(5): p. 495-497.

91.   Leutenegger, M. et al., *Fluorescence correlation spectroscopy with a total internal reflection fluorescence STED microscope (TIRF-STED-FCS).* Optics express, 2012. **20**(5): p. 5243-5263.

92.   Silva, W.R., C.T. Graefe, and R.R. Frontiera, *Toward label-free super-resolution microscopy.* ACS Photonics 2016, **3**(1): p. 79-86.

93.   Tormo, A.D. et al., *Superresolution 4π raman microscopy.* Optics Letters 2017, **42**(21): p. 4410-4413.

94.   Schleeger, M., M. Grechko, and M. Bonn, *Background-free fourth-order sum frequency generation spectroscopy.* Journal of Physical Chemistry Letters 2015, **6**(11): p. 2114-20.

95.   Hecht, E., *Optics*. Vol. 4. 2002: Addison Wesley San Francisco.

96.   Hilborn, R.C., *Einstein coefficients, cross sections, f values, dipole moments, and all that.* American Journal of Physics 1982. **50**(11): p. 982-986.

97.   ThorLabs, *ThorLabs Motorized Actuator Z825-B Manual*.

98.   Kehlet, L.M. et al., *Infrared upconversion hyperspectral imaging.* Optics letters 2015, **40**(6): p. 938-941.

99.   Høgstedt, L. et al., *Low-noise mid-IR upconversion detector for improved IR-degenerate four-wave mixing gas sensing.* Optics letters 2014, **39**(18): p. 5321-5324.

100.   Baldelli, S., *Sensing: Infrared image upconversion.* Nature Photonics 2011, **5**(2): p. 75.

101.   II-VI Incorporated, *Vortex Lens*. 2019

102.   Nakamura, M., M.-B. Song, and M. Ito, *Etching processing of Si (111) and Si (100) surfaces in an ammonium fluoride solution investigated by in situ ATR-IR.* Electrochimica Acta 1996, **41**(5): p. 681-686.

103. Dumas, P., Y. Chabal, and P. Jakob, *Morphology of hydrogen-terminated Si (111) and Si (100) surfaces upon etching in HF and buffered-HF solutions.* Surface Science 1992, **269**: p. 867-878.
104. Allongue, P., V. Kieling, and H. Gerischer, *Etching mechanism and atomic structure of H-Si (111) surfaces prepared in NH4F.* Electrochimica Acta 1995, **40**(10): p. 1353-1360.
105. Chabal, Y., *Etching of silicon (111) and (100) surfaces in HF solutions: H-termination, atomic structure and overall morphology.* MRS Proceedings 1992, **259**.
106. Lenox Laser, *Optical Apertures*
107. Edmund Optics, *Hybrid Aspheric Lenses*.
108. Krummacher, B.C. et. al., *Highly efficient white organic light-emitting diode.* Applied Physics Letters 2006, **88**(11): p. 113506.
109. Geffroy, B., P. Le Roy, and C. Prat, *Organic light-emitting diode (OLED) technology: materials, devices and display technologies.* Polymer International 2006 **55**(6): p. 572-582.
110. Kijima, Y., N. Asai, and S.-i. Tamura, *A blue organic light emitting diode.* Japanese Journal of Applied Physics 1999, **38**(9R): p. 5274.
111. Chen, H.-W. et. al., *Liquid crystal display and organic light-emitting diode display: present status and future perspectives.* Light Science Applications 2018, **7**(3): p. 17168-17168.

112. Sekitani, T. et. al., *Stretchable active-matrix organic light-emitting diode display using printable elastic conductors.* Nature Materials 2009 **8**(6): p. 494-499.
113. Cheng, P. and X. Zhan, *Stability of organic solar cells: challenges and strategies.* Chemical Society Reviews 2016, **45**(9): p. 2544-2582.
114. Hoppe, H. and N.S. Sariciftci, *Organic solar cells: An overview.* Journal of Materials Research 2004, **19**(7): p. 1924-1945.
115. Wöhrle, D. and D. Meissner, *Organic solar cells.* Advanced Materials 1991, **3**(3): p. 129-138.
116. Wu, J. et. al., *Organic solar cells with solution-processed graphene transparent electrodes.* Applied Physics Letters 2008, **92**(26): p. 237.
117. Kaltenbrunner, M. et. al., *Ultrathin and lightweight organic solar cells with high flexibility.* Nature Communications 2012, **3**(1): p. 1-7.
118. Aziz, H. and Z.D. Popovic, *Study of organic light emitting devices with a 5, 6, 11, 12-tetraphenylnaphthacene (rubrene)-doped hole transport layer.* Applied Physics Letters 2002, **80**(12): p. 2180-2182.
119. Pandey, A.K. and J.-M. Nunzi, *Upconversion injection in rubrene/perylene-diimide-heterostructure electroluminescent diodes.* Applied Physics Letters 2007, **90**(26): p. 263508.
120. Pandey, A.K. and J.-M. Nunzi, *Rubrene/Fullerene heterostructures with a half-gap electroluminescence threshold and large photovoltage.* Advanced Materials 2007, **19**(21): p. 3613-3617.
121. Xie, W. et. al., *High-efficiency simple structure white organic light-emitting devices based on rubrene ultrathin layer.* Optical and Quantum Electronics 2005, **37**(10): p. 943-948.
122. Murata, H., C.D. Merritt, and Z.H. Kafafi, *Emission mechanism in rubrene-doped molecular organic light-emitting diodes: direct carrier recombination at luminescent centers.* IEEE Journal of Selected Topics in Quantum Electronics 1998, **4**(1): p. 119-124.
123. de Boer, R.W.I. et. al., *Organic single-crystal field-effect transistors.* Physica Status Solidi (a) 2004, **201**(6): p. 1302-1331.
124. Podzorov, V., V. Pudalov, and M. Gershenson, *Field-effect transistors on rubrene single crystals with parylene gate insulator.* Applied Physics Letters 2003, **82**(11): p. 1739-1741.
125. Takeya, J. et. al., *Very high-mobility organic single-crystal transistors with in-crystal conduction channels.* Applied Physics Letters 2007, **90**(10): p. 102-120.

126. Xie, W. et. al., *High-mobility transistors based on single crystals of isotopically substituted rubrene-d 28.* The Journal of Physical Chemistry C 2013, **117**(22): p. 11522-11529.

127. Nitta, J. et. al., *The actual electronic band structure of a rubrene single crystal.* Scientific Reports 2019 **9**(1): p. 9645.

128. Iimori, T., R. Ito, and N. Ohta, *Stark spectroscopy of rubrene. II. stark fluorescence spectroscopy and fluorescence quenching induced by an external electric field.* Journal of Physical Chemistry A 2016, **120**(28): p. 5497-503.

129. Iimori, T. et. al., *Stark spectroscopy of rubrene. I. electroabsorption spectroscopy and molecular parameters.* Journal of Physical Chemistry A 2016, **120**(25): p. 4307-13.

130. Kim, J.J. et. al., *Correlating crystal thickness, surface morphology, and charge transport in pristine and doped rubrene single crystals.* ACS Applied Materials & Interfaces 2018, **10**(31): p. 26745-26751.

131. Li, W. et. al., *Aging of rubrene layers in Ni/rubrene heterostructures studied by magneto-optical Kerr effect spectroscopy.* American Chemical Society 2010, **132**(16): p. 5687-92.

132. Park, S.W. et. al., *Amorphous-to-crystalline phase transformation of thin film rubrene.* Journal of Physical Chemistry B 2010, **114**(17): p. 5661-5.

133. Ren, X., C.D. Frisbie, and C. Leighton, *Anomalous cooling-rate-dependent charge transport in electrolyte-gated rubrene crystals.* Journal of Physical Chemistry Letters 2018, **9**(17): p. 4828-4833.

134. Sun, K., M. Lan, and J.Z. Wang, *Absolute configuration and chiral self-assembly of rubrene on Bi(111).* Journal of Physical Chemistry Chemical Physics 2015, **17**(39): p. 26220-4.

135. Tao, S. et. al., *Relaxation dynamics of photoexcited excitons in rubrene single crystals using femtosecond absorption spectroscopy.* Physical Review Letters 2012, **109**(9): p. 097403.

136. Ueba, T., T. Yamada, and T. Munakata, *Electronic excitation and relaxation dynamics of the LUMO-derived level in rubrene thin films on graphite.* Journal of Chemical Physics 2016, **145**(21): p. 214703.

137. Wang, J.-Z. et. al., *STM study of a rubrene monolayer on Bi (001): Structural modulations.* Physical Review B 2011, **83**(23): p. 235433.

138. BLüM, M.-C., *Supramolecular assembly, chirality, and electronic properties of rubrene studied by STM and STS*. EPFL 2006.

139. Miwa, J. et. al., *Self-assembly of rubrene on Cu (111).* Nanotechnology 2008, **19**(42): p. 424021.

140. Minato, T. et. al., *High-resolution molecular images of rubrene single crystals obtained by frequency modulation atomic force microscopy.* Applied Physics Letters 2009, **95**(9): p. 221.

141. Yokota, Y. et. al., *Structural investigation of ionic liquid/rubrene single crystal interfaces by using frequency-modulation atomic force microscopy.* Chemical Communications 2013, **49**(90): p. 10596-10598.

142. Sinha, S. et. al., *Oxidation of rubrene thin films: an electronic structure study.* Langmuir 2014, **30**(51): p. 15433-15441.

143. LENG, C.-q. et. al., *Surface and interface analysis of Rubrene/TPD using AFM and XPS.* Journal of Functional Materials 2010: p. S2.

144. Ji, G. et. al., *Interfacial electronic structures revealed at the rubrene/CH3NH3PbI3 interface.* Journal of Physical Chemistry Chemical Physics 2017, **19**(9): p. 6546-6553.

145. Choi, H.H. et. al., *A large anisotropic enhancement of the charge carrier mobility of flexible organic transistors with strain: a hall effect and raman study.* Advanced Science 2020, **7**(1): p. 1901824.
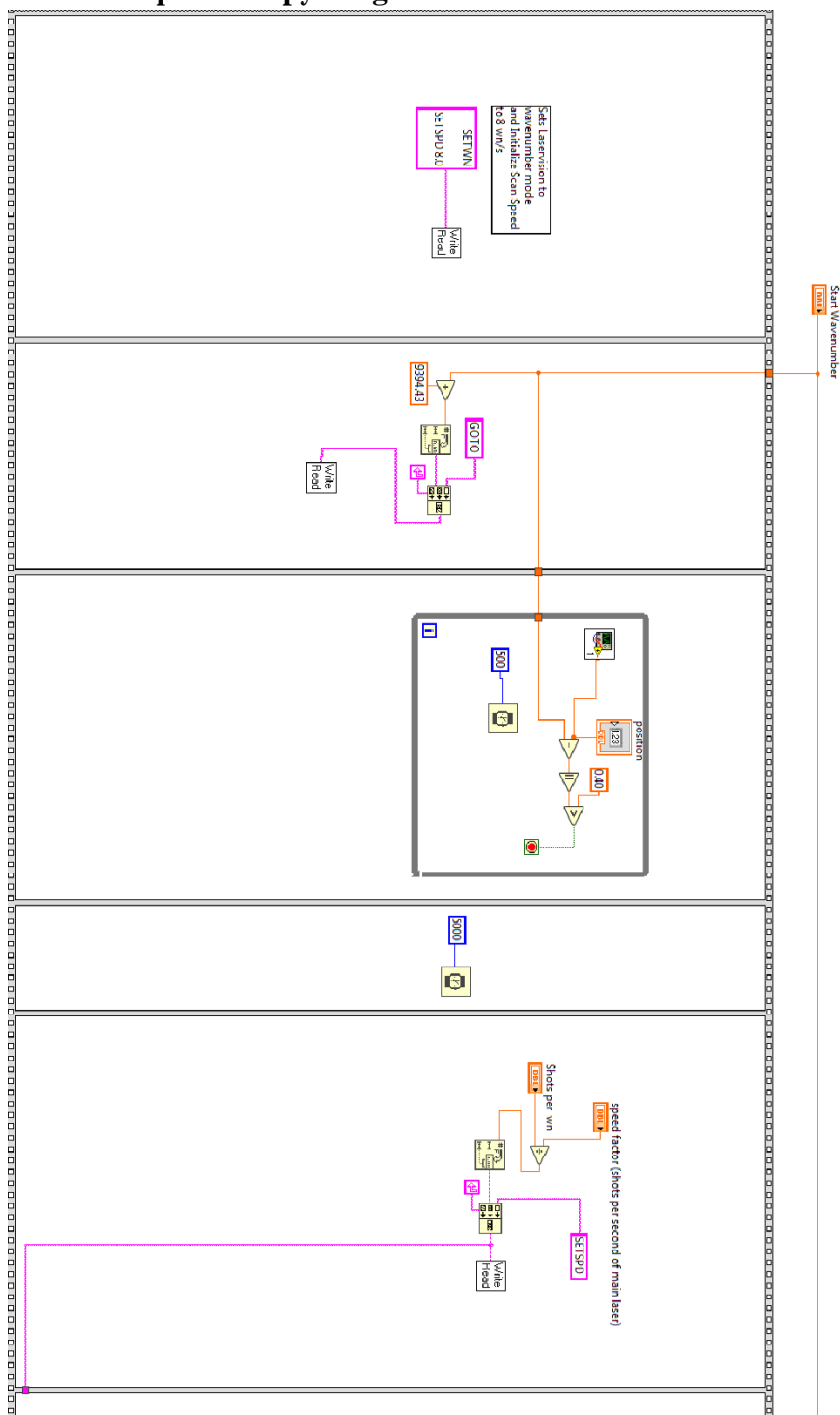
146.   Bera, K., C.J. Douglas, and R.R. Frontiera, *Femtosecond raman microscopy reveals structural dynamics leading to triplet separation in rubrene singlet fission.* Journal of Physical Chemistry Letters 2017, **8**(23): p. 5929-5934.

147.   Tavazzi, S. et. al., *Generalized ellipsometry and dielectric tensor of rubrene single crystals.* Journal of Applied Physics 2007, **102**(2): p. 023107.

148.   Tavazzi, S. et. al., *Optical response and emission waveguiding in rubrene crystals.* Physical Review B 2007, **75**(24): p. 245416.

149.   Jiang, H. and C. Kloc, *Single-crystal growth of organic semiconductors.* MRS Bulletin 2013, **38**(1): p. 28-33.

150.   Jurchescu, O.D., A. Meetsma, and T.T. Palstra, *Low-temperature structure of rubrene single crystals grown by vapor transport.* Acta Crystallographica Section B: Structural Science 2006, **62**(2): p. 330-334.

151.   Käfer, D. et. al., *Role of Molecular Conformations in Rubrene Thin Film Growth.* Physical Review Letters 2005, **95**(16): p. 166602.

152.   Irkhin, P. and I. Biaggio, *Two-photon absorption spectroscopy of rubrene single crystals.* Physical Review B 2014, **89**(20): p. 201202.

153.   Sai, N. et. al., *Optical spectra and exchange-correlation effects in molecular crystals.* Physical Review B 2008, **77**(16): p. 161306.

154.   Raimondo, L. et. al., *Oxidation of crystalline rubrene films: evidence of an epitaxial native oxide layer.* Advanced Materials Interfaces 2017, **4**(23): p. 1700670.

155.   Ly, J.T. et. al., *Oxidation of rubrene, and implications for device stability.* Journal of Materials Chemistry C 2018. **6**(14): p. 3757-3761.

156.   Oh-e, M., S.-C. Hong, and Y.R. Shen, *Orientations of phenyl sidegroups and liquid crystal molecules on a rubbed polystyrene surface.* Applied Physics Letters 2002, **80**(5): p. 784-786.

157.   Duffy, D.C., P.B. Davies, and C.D. Bain, *Surface vibrational spectroscopy of organic counterions bound to a surfactant monolayer.* The Journal of Physical Chemistry 1995, **99**(41): p. 15241-15246.

158.   Bell, G.R., *Orientation of benzoate ions bound to a monolayer of a cationic surfactant at the surface of water.* Molecular Physics 1996, **88**(1): p. 269-280.

159.   Zhuang, X. et. al., *Mapping molecular orientation and conformation at interfaces by surface nonlinear optics.* Physical Review B 1999, **59**(19): p. 12632.

160.   Hirose, C., N. Akamatsu, and K. Domen, *Formulas for the analysis of the surface SFG spectrum and transformation coefficients of cartesian SFG tensor components.* Applied Spectroscopy 1992, **46**(6): p. 1051-1072.

161.   Lee, E.S. et. al., *Vibrationally resonant sum-frequency generation microscopy with a solid immersion lens.* Biomedical Optics Express 2014, **5**(7): p. 2125-34.

162.   Fu, Y. et. al., *Second harmonic and sum frequency generation imaging of fibrous astroglial filaments in ex vivo spinal tissues.* Biophysical Journal 2007, **92**(9): p. 3251-9.

163.   Cimatu, K. and S. Baldelli, *Chemical imaging of corrosion: sum frequency generation imaging microscopy of cyanide on gold at the solid-liquid interface.* American Chemical Society 2008, **130**(25): p. 8030-7.

164.   Cimatu, K. and S. Baldelli, *Sum frequency generation imaging microscopy of CO on platinum.* American Chemical Society 2006, **128**(50): p. 16016-7.

165.   Goodfellow, I., Y. Bengio, and A. Courville, *Deep learning.* Vol. 1. 2016: MIT Press.

166.   McCulloch, W.S. and W. Pitts, *A logical calculus of the ideas immanent in nervous activity.* The Bulletin of Mathematical Biophysics 1943, **5**(4): p. 115-133.
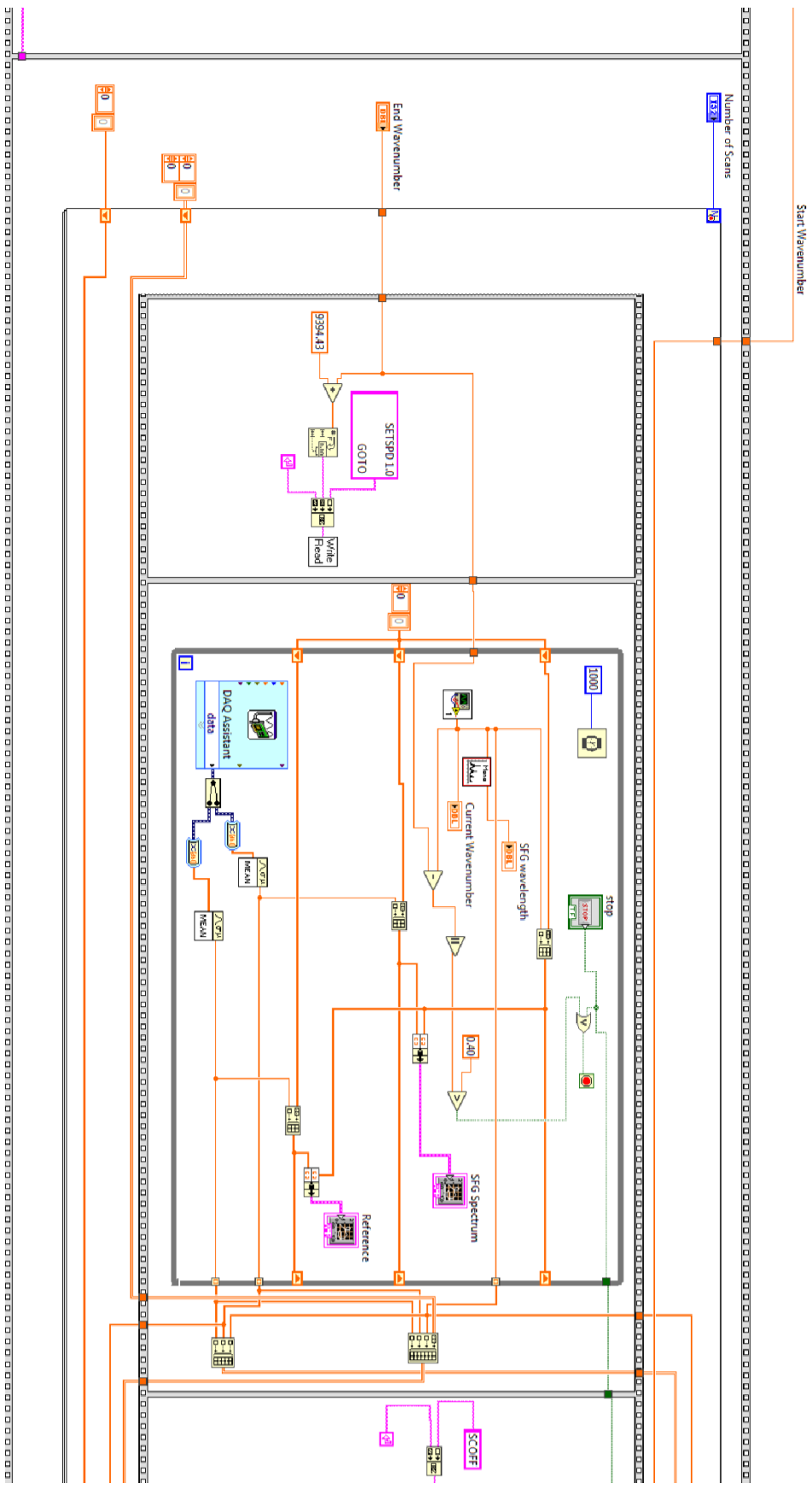
167. Rosenblatt, F., *The perceptron: a probabilistic model for information storage and organization in the brain.* Psychological Review 1958, **65**(6): p. 386.

168. Egmont-Petersen, M., D. de Ridder, and H. Handels, *Image processing with neural networks—a review.* Pattern Recognition 2002, **35**(10): p. 2279-2301.

169. Paliwal, M. and U.A. Kumar, *Neural networks and statistical techniques: A review of applications.* Expert Systems with Applications 2009, **36**(1): p. 2-17.

170. Lipton, Z.C., J. Berkowitz, and C.J.a.p.a. Elkan, *A critical review of recurrent neural networks for sequence learning.* arXiv:1506.00019, 2015.

171. Kalogirou, S.A., *Artificial neural networks in renewable energy systems applications: a review.* Renewable Sustainable Energy Reviews 2001, **5**(4): p. 373-401.

172. Rawat, W. and Z. Wang, *Deep convolutional neural networks for image classification: A comprehensive review.* Neural Computation 2017, **29**(9): p. 2352-2449.

173. Netflix, Machine Learning, 2020.

174. O'Connor, N. and M.G. Madden. *A neural network approach to predicting stock exchange movements using external factors*. in *International Conference on Innovative Techniques and Applications of Artificial Intelligence*. 2005. Springer.

175. Guresen, E., G. Kayakutlu, and T.U. Daim, *Using artificial neural network models in stock market index prediction.* Expert Systems with Applications 2011, **38**(8): p. 10389-10397.

176. Ulman, A. et. al., *Self-assembled monolayers of rigid thiols.* Journal of Biotechnology 2000, **74**(3): p. 175-88.

177. Vericat, C. et. al., *Self-assembled monolayers of thiols and dithiols on gold: new challenges for a well-known system.* Chemical Society Reviews 2010, **39**(5): p. 1805-34.

178. Whitesides, G.M., J.K. Kriebel, and J.C. Love, *Molecular engineering of surfaces using self-assembled monolayers.* Science Progress 2005, **88**(Pt 1): p. 17-48.

179. Gooding, J.J. et. al., *Self-assembled monolayers into the 21st century: recent advances and applications.* Electroanalysis 2003, **15**(2): p. 81-96.

180. Prashar, D., *Self assembled monolayers-a review.* International Journal of ChemTech Research 2012, **4**(1): p. 258-265.

181. Laibinis, P.E. et. al., *Comparison of the structures and wetting properties of self-assembled monolayers of n-alkanethiols on the coinage metal surfaces, copper, silver, and gold.* Journal of the American Chemical Society 1991, **113**(19): p. 7152-7167.

182. Abbott, N.L., C.B. Gorman, and G.M. Whitesides, *Active control of wetting using applied electrical potentials and self-assembled monolayers.* Langmuir 1995, **11**(1): p. 16-18.

183. Schoenbaum, C.A., D.K. Schwartz, and J.W. Medlin, *Controlling the surface environment of heterogeneous catalysts using self-assembled monolayers.* Accounts of Chemical Research 2014, **47**(4): p. 1438-1445.

184. Marshall, S.T. et. al., *Controlled selectivity for palladium catalysts using self-assembled monolayers.* Nature materials 2010, **9**(10): p. 853-858.

185. Balmer, T.E. et. al., *Diffusion of alkanethiols in PDMS and its implications on microcontact printing (µCP).* Langmuir 2005, **21**(2): p. 622-632.

186. Cimatu, K.A. and S. Baldelli, *Sum Frequency Generation Imaging of CO on Platinum Surfaces.* American Chemical Society 2006, **128**(50): p. 16016.

187. Cimatu, K.A. and S. Baldelli, *Sum Frequency Generation Microscopy of Microcontact-Printed Mixed Self-Assembled Monolayers.* Journal of Physical Chemistry B 2006, **110**: p. 1807.

188. Fang, M. and S. Baldelli, *Grain Structures and Boundaries on Microcrystalline Copper Covered with an Octadecanethiol Monolayer Revealed by Sum Frequency Generation Microscopy.* Phyiscal Chemistry Letters 2015, **6**(8): p. 1454-1460.
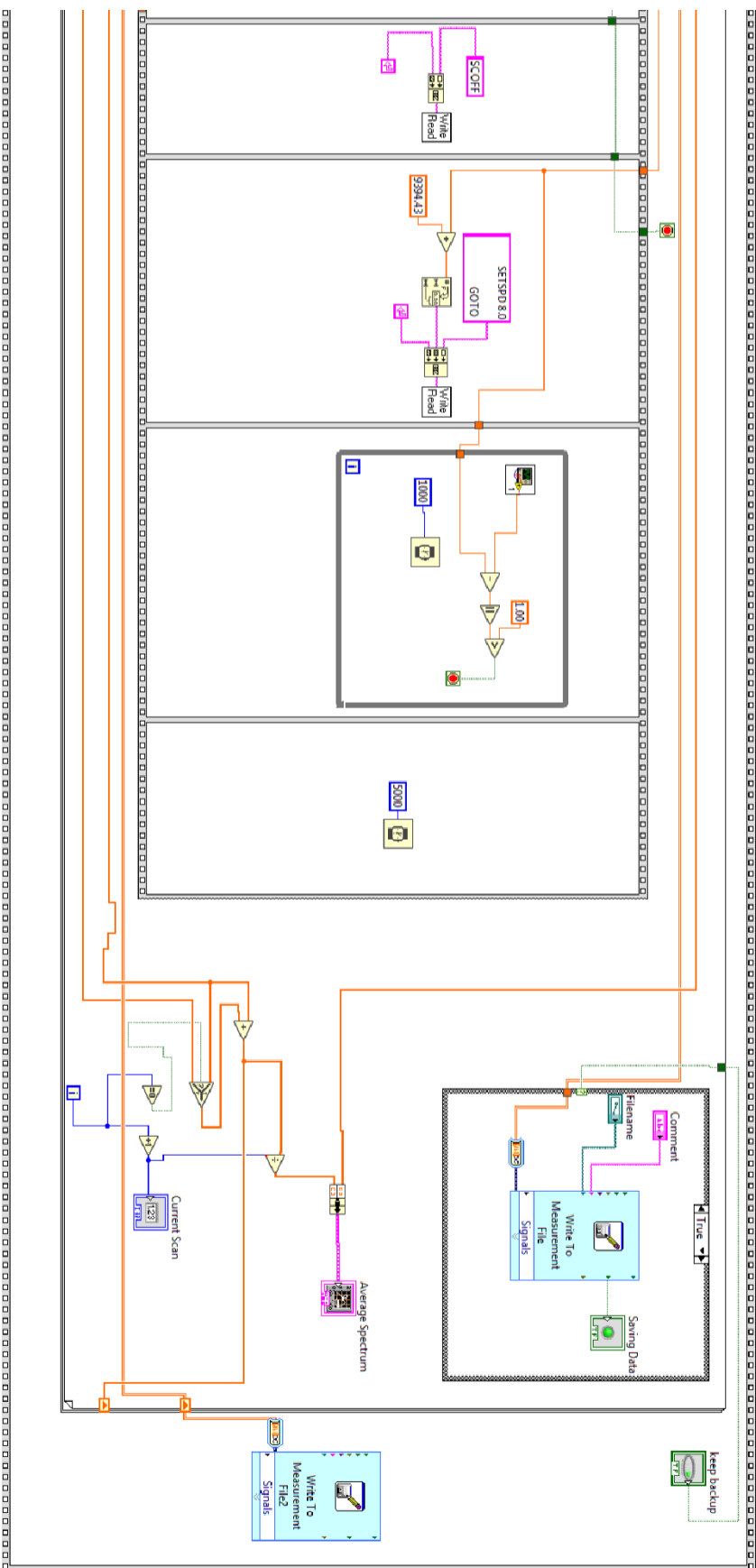
189.   Pikalov, A.A. et. al., *Sum Frequency Generation Imaging Microscopy of Self-Assembled Monolayers on Metal Surfaces: Factor Analysis of Mixed Monolayers.* Anals of Chemistry 2019, **91**: p. 1269–1276.

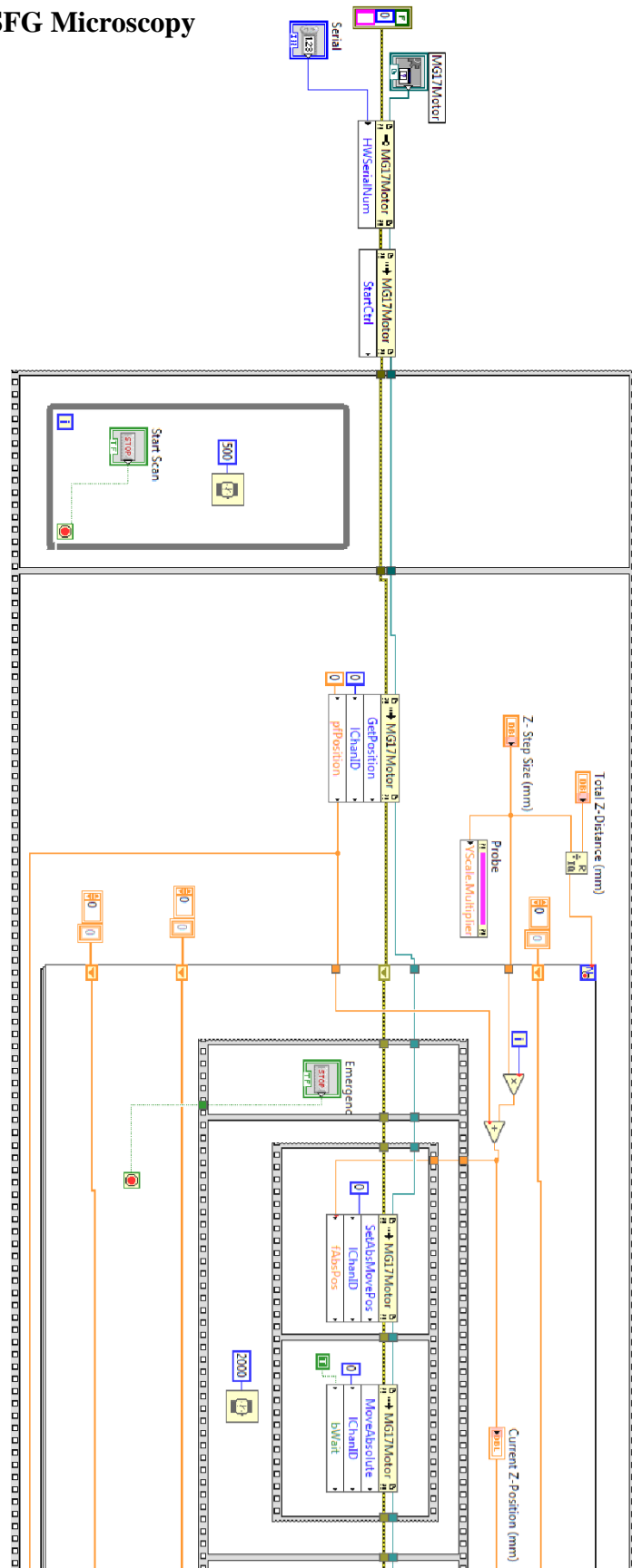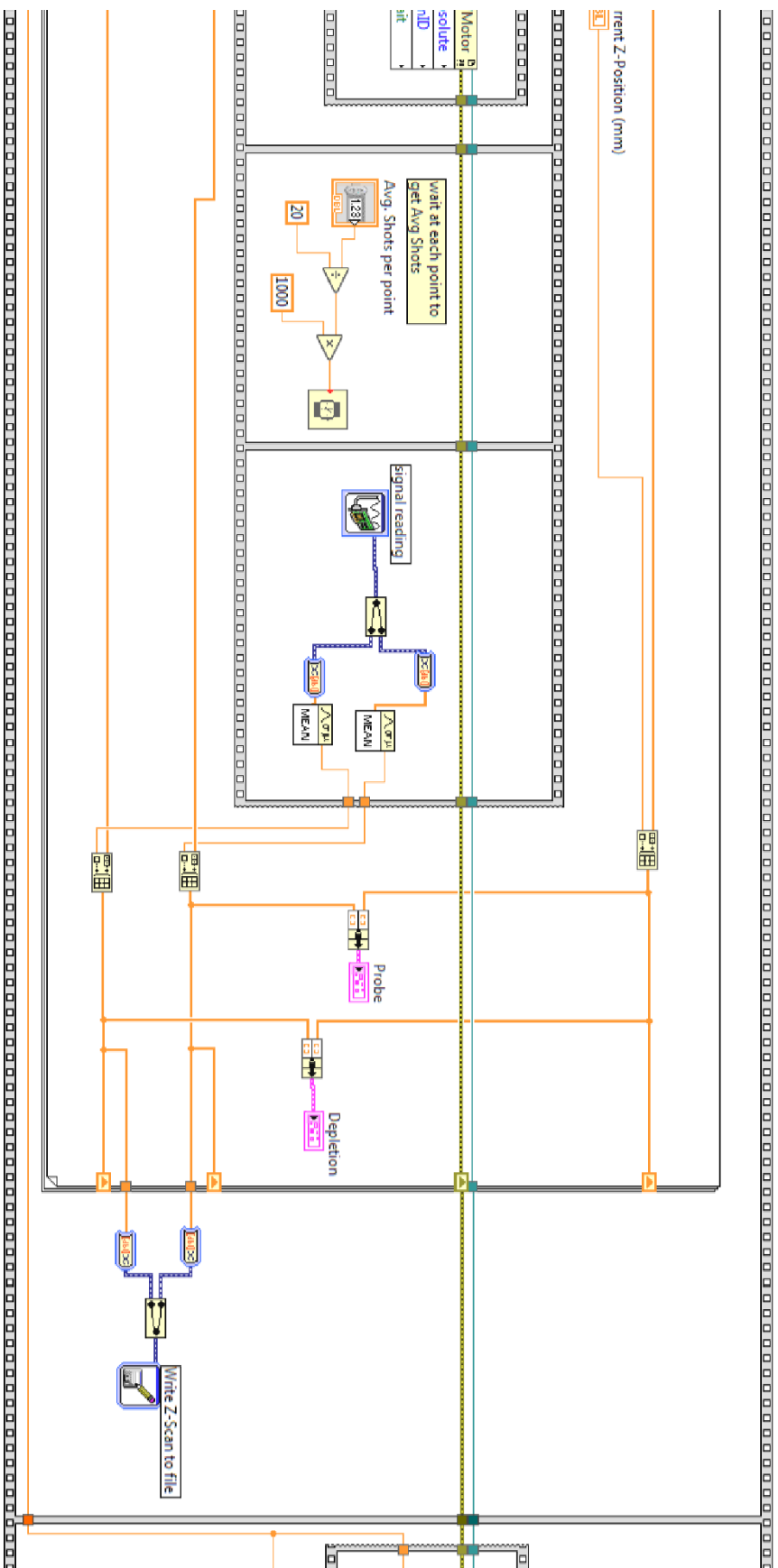# Appendix

LabView Code for SFG Spectroscopy Program:

LabView code for SFG Microscopy

Motor

wait at each point to
get Avg Shots

Avg. Shots per point

signal reading

Probe

Depletion

Write Z-Scan to file

rrent Z-Position (mm)

Rubrene Analysis: Mathematical Expressions for Transformations

In these expression, r is the ratio $\frac{\beta_{\Lambda\Lambda\Lambda}}{\beta_{\eta\eta\Lambda}}$. (Note: in this code, Ω_i is renamed as β_i)

$In[\circ]:=$
```
n1 = 1;
na = 1.8;
nb = 1.6;
n2[ℰ_] := Sqrt[(Cos[ℰ] na)² + (Sin[ℰ] nb)²]
n[ℰ_] := (n2[ℰ] + 1)/2
γ[ℰ_, β_] := ArcSin[n1 Sin[β] / n2[ℰ]]
Lxx[ℰ_, β_] := (2 n1 Cos[γ[ℰ, β]])/(n1 Cos[γ[ℰ, β]] + n2[ℰ] Cos[β])
Lyy[ℰ_, β_] := (2 n1 Cos[β])/(n1 Cos[β] + n2[ℰ] Cos[γ[ℰ, β]])
Lzz[ℰ_, β_] := (2 n2[ℰ] Cos[β])/(n1 Cos[γ[ℰ, β]] + n2[ℰ] Cos[β]) (n1/n[ℰ])²
```

$In[\circ]:=$
```
Xzxx[θ_, ψ_, φ_] := ((Cos[θ] - Cos[3 θ]) / 8) (1 + Cos[2 ψ]) +
    (- ((Cos[θ] - Cos[3 θ]) / 16) (1 + Cos[2 ψ]) (1 + Cos[2 φ]) +
        ((1 - Cos[2 θ]) / 8) Sin[2 ψ] Sin[2 φ]) r
```

$In[\circ]:=$
```
Xzzz[θ_, ψ_, φ_] :=
    ((3 Cos[θ] + Cos[3 θ]) / 4) + ((Cos[θ] - Cos[3 θ]) / 8) (1 + Cos[2 φ]) r
```

$In[\circ]:=$
```
Xyyz[θ_, ψ_, φ_] := ((Cos[θ] - Cos[3 θ]) / 8) (1 - Cos[2 ψ]) +
    (Cos[θ / 2] (1 - Cos[2 ψ] Cos[2 φ]) -
        ((Cos[θ] - Cos[3 θ]) / 16) (1 - Cos[2 ψ]) (1 + Cos[2 φ]) +
        ((1 + Cos[2 θ]) / 4) Sin[2 ψ] Sin[2 φ]) r
```

$In[\circ]:=$
```
Xxzx[θ_, ψ_, φ_] := ((Cos[θ] - Cos[3 θ]) / 8) (1 + Cos[2 ψ]) +
    (- ((Cos[θ] - Cos[3 θ]) / 16) (1 + Cos[2 ψ]) (1 + Cos[2 φ]) +
        ((1 - Cos[2 θ]) / 8) Sin[2 ψ] Sin[2 φ]) r
```

$In[\circ]:=$
```
Xxxz[θ_, ψ_, φ_] := ((Cos[θ] - Cos[3 θ]) / 8) (1 + Cos[2 ψ]) +
    (Cos[θ / 2] (1 + Cos[2 ψ] Cos[2 φ]) -
        ((Cos[θ] - Cos[3 θ]) / 16) (1 + Cos[2 ψ]) (1 + Cos[2 φ]) -
        ((1 + Cos[2 θ]) / 4) Sin[2 ψ] Sin[2 φ]) r
```

Python Implementation for Neural Networks:

There are two main codes for the python implementation i.e.,

1. Data Wrangling
2. Multi-Class Model

The Data Wrangling code utilizes the pixel spectra extracted from the SAMs data to create training and testing datasets. Typically, the training and testing sets contain 70 % and 30 % of the total data. The process is as follows:

a. The SAMs data is contained in 5 sets. Each set is created by using the SFG images acquired from pure sample of a single SAM; therefore, each set contains pixel spectra for one particular SAM. For each SAM, a unique number is assigned as label (typically, 0 to 4).
b. A new dataset is created by joining all 5 sets along with their labels. In this new set, each data point contains a spectrum and its label that identifies its' SAM.
c. This dataset is shuffled and then separated into the training and testing sets.

Multi-Class Model code is responsible for creating, training, and testing the NNs. It performs these tasks as follows:

a. It creates a fully connected NN with 4 layers. The first layer has 71 perceptrons, the second contains 1000 perceptrons, the third has 100, and the fourth layer is made of only 5 perceptrons.
b. The spectra are fed into the NN through the Input layer (1st layer) and the Output layer (4th layer) makes the prediction for its chemical label. The prediction is made by selecting the chemical label for the perception that shows maximum numerical valued output.
c. In total, this fully connected NN contains 171500 weights. These weights are initially assigned random values. During training, the weights are calibrated to match the NN predictions with the true labels of the training spectra.
d. During testing phase, the predicted labels for the testing set are matched with the true chemical labels and the accuracy is calculated as misclassification error.

The code for Data Wrangling:

```python
import numpy as np


def generate_five_sams_data(training_fraction):
    odt = np.load('processed data\multi sams data-solution\odt.npy')
    methoxy = np.load('processed data\multi sams data-solution\meoht.npy')
    phhdt = np.load('processed data\multi sams data-solution\phhdt.npy')
    h2f = np.load('processed data\multi sams data-solution\h2f.npy')
    carborane = np.load('processed data\multi sams data-
```

```python
solution\carborane.npy')
    #gold = np.load('processed data\multi sams data\processed_gold.npy')
    np.random.shuffle(odt)
    np.random.shuffle(methoxy)
    np.random.shuffle(phhdt)
    np.random.shuffle(h2f)
    np.random.shuffle(carborane)
    #np.random.shuffle(gold)

    odt_labels = [int(0)] * np.shape(odt)[0]
    methoxy_labels = [int(1)] * np.shape(methoxy)[0]
    phhdt_labels = [int(2)] * np.shape(phhdt)[0]
    h2f_labels = [int(3)] * np.shape(h2f)[0]
    carborane_labels = [int(4)] * np.shape(carborane)[0]

    print("Label assignments: odt 0, methoxy 1, phhdt 2, h2f 3 and carborane
4.")
    total_data = np.concatenate((odt, methoxy, phhdt, h2f, carborane), 0)
    labels = np.concatenate((odt_labels, methoxy_labels, phhdt_labels,
h2f_labels, carborane_labels), 0)
    print('shape of total data ', np.shape(total_data), 'shape of labels ',
np.shape(labels))


    print('randomly permuting data')
    p = np.random.permutation(len(total_data))
    total_data = total_data[p]
    labels = labels[p]

    print('element of lables', labels[0:10])
    print('elements of data', total_data[0:10])

    # splitting data according to split fraction
    split_index = int(np.shape(total_data)[0] * training_fraction)

    training_spectra = total_data[:split_index]
    test_spectra = total_data[split_index:]
    training_labels = labels[:split_index]
    test_labels = labels[split_index:]

    return [training_spectra, training_labels, test_spectra, test_labels]
```

The code for Multi-Class:

```python
import numpy as np
import tensorflow as tf
```

```python
import matplotlib.pyplot as plt
import data_wrangling


def create_model():
  model = tf.keras.models.Sequential([
#    tf.keras.layers.Flatten(),
    tf.keras.layers.Dense(71, activation=tf.nn.relu),
#    tf.keras.layers.Dropout(0.25),
#    tf.keras.layers.Flatten(),
#    tf.keras.layers.Conv1D(filters=71, kernel_size=10),
    tf.keras.layers.Dense(1000, activation=tf.nn.relu),
    tf.keras.layers.Dense(100, activation=tf.nn.relu),
    tf.keras.layers.Dense(5, activation=tf.nn.softmax),
#    tf.keras.layers.Dropout(0.25)
  ])
  model.compile(optimizer='adam', loss='sparse_categorical_crossentropy',
metrics=['accuracy'])
  return model


class myCallback(tf.keras.callbacks.Callback):
  def on_epoch_end(self, epoch, logs=[87]):
    if (logs.get('acc') > 0.98):
      print("\nReached 98% accuracy so cancelling training!")
      self.model.stop_training = True


def train(training_fraction):
  model = create_model()
  [training_spectra, training_labels, test_spectra, test_labels] = \
    data_wrangling.generate_five_sams_binned_data(training_fraction)
  callbacks = myCallback()

  model.fit(training_spectra, training_labels, epochs=5,
callbacks=[callbacks])

  validation_loss = model.evaluate(test_spectra, test_labels)
# model.save_weights('trained models\my5component_checkpoint')
  print(model.predict(test_spectra))


  # testing out new image
  #fiveSams1k = np.load('processed data\multi sams data-
stamped\\fiveSams1k.npy')
  fiveSams5k = np.load('processed data\multi sams data-
stamped\\fiveSams5k.npy')
  new_labels = model.predict(fiveSams5k)
  print(np.shape(new_labels))
  np.save('Results\\5sams5k-new_labels', new_labels)
  final_labels = []
  for a in range(1024):
    final_labels.append(new_labels[a * 1024:a * 1024 + 1024, :])

  image = np.array(final_labels)
```

```python
    np.save('Results\\5sams5k-image', image)
    print('shape of image is ', np.shape(image))




def load_and_test_model():
    #odt methoxy = np.load('processed
data\gold_odt_methoxy\processed_odt_methoxy.npy')
    model = create_model()
    model.load_weights('trained models\my5component_checkpoint')
```